EXTENSION OF NEOCLASSICAL ROTATION THEORY FOR TOKAMAKS TO ACCOUNT FOR GEOMETRIC EXPANSION/COMPRESSION OF MAGNETIC FLUX SURFACES

A Dissertation
Presented to
The Academic Faculty
of the Nuclear and Radiological
Engineering Program

by

Cheonho Bae

In Partial Fulfillment
of the Requirements for the Degree
Doctorate in the
Nuclear and Radiological Engineering Program

Georgia Institute of Technology
December 2012

EXTENSION OF NEOCLASSICAL ROTATION THEORY FOR TOKAMAKS TO ACCOUNT FOR GEOMETRIC EXPANSION/COMPRESSION OF MAGNETIC FLUX SURFACES

Approved by:

Dr. Weston M. Stacey, Advisor
Nuclear and Radiological Engineering Program
Georgia Institute of Technology

Dr. Farzad Rahnema
Nuclear and Radiological Engineering Program
Georgia Institute of Technology

Dr. Wayne M. Solomon
Princeton Plasma Physics Laboratory

Dr. Jeff I. Jagoda
School of Aerospace Engineering
Georgia Institute of Technology

Dr. Bojan Petrovic
Nuclear and Radiological Engineering Program
Georgia Institute of Technology

Date Approved: August 31, 2012

ACKNOWLEDGEMENTS

I would like to extend my deepest gratitude for all those who have guided and supported for the completion of my study at Georgia Tech. I thank Dr. Jagoda for accepting me to Georgia Tech and providing guidance and advises during my Aerospace study. I thank Dr. Rahnema for assistance and guidance as I was making the transition to NRE program. I also thank Dr. Petrovic for the excellent courses that help me understand my new study field to comfortably settle in the NRE program. I thank Dr. Solomon not only for the experimental data he provided but also for an excellent experimental perspective on my research and the hands-on experience on TRANSP, which will be a great tool as I continue my research in nuclear fusion. I also thank Dr. Morley, school of mathematics at Georgia Tech, for the guidance and advises on the numerical solution of my theory and the code development. Lastly, my special thanks goes to my advisor, Dr. Stacey, for introducing me into the nuclear fusion world where I do find the meaning of my life and for the excellent guidance and patience all throughout the difficult times with the research. I've had many life-changing moments in my short life but meeting Dr. Stacey and being introduced into the nuclear fusion field surely stand on the top of the list and I sincerely thank Dr. Stacey for having me as one of his students.

I also would not forget those support from my family, Yunuk and Youngsoo, and friends for making my study at Georgia Tech a pure joy. I also thank John-Patrick and other lab-mates for the good times we shared together at Georgia Tech and wish to continue cooperating to realize the dream energy available for the future generations.

TABLE OF CONTENTS

LIST OF TABLES

LIST OF FIGURES

SUMMARY

An extended neoclassical rotation theory (poloidal and toroidal) is developed from the fluid moment equations, using the Braginskii decomposition of the viscosity tensor extended to generalized curvilinear geometry and a neoclassical calculation of the parallel viscosity coefficient interpolated over collision regimes. Important poloidal dependences of density and velocity are calculated using the Miller equilibrium flux surface geometry representation, which takes into account elongation, triangularity, flux surface compression/expansion and the Shafranov shift. The resulting set of eight (for a two-ion-species plasma model) coupled nonlinear equations for the flux surface averaged poloidal and toroidal rotation velocities and for the up-down and in-out density asymmetries for both ion species are solved numerically. The numerical solution methodology, a combination of nonlinear Successive Over-Relaxation(SOR) and Simulated Annealing(SA), is also discussed. Comparison of prediction with measured carbon poloidal and toroidal rotation velocities in a co-injected and a counter-injected H-mode discharges in DIII-D [J. Luxon, Nucl. Fusion 42, 614 (2002)] indicates agreement to within <10% except in the very edge ($\rho > .90$) in the co-injected discharge.

CHAPTER 1

INTRODUCTION

Rotation of tokamak plasmas is known to be important for the stabilization of Magnetohydrodynamics (MHD) instabilities and for achieving good confinement in tokamaks, as well as providing insight about transport. Earlier studies indicated that toroidal rotation affects neoclassical particle transport to suppress the MHD instabilities [1-4] and is postulated to play a role in the shear suppression of microinstabilities that enhance transport [5]. Because of the importance of characterizing and understanding toroidal rotation and the related angular momentum transport in neutral beam driven tokamaks, there has been a longstanding effort both experimentally [6-11] and theoretically [12-28] to understand and predict toroidal rotation, but this task has been challenging. Poloidal rotation is also of interest because of its role in the shear suppression of turbulent energy transport [29].

In understanding toroidal rotation and the angular torque mechanisms, representation of the viscosity stress is very important. From the earlier classical studies in cylindrical geometry [9, 14, 15], the familiar perpendicular viscosity was calculated to be too small to account for the observed momentum damping. Taking neoclassical effects into account [14, 15, 18, 19] did not change this result, leading to the belief that the momentum transport in tokamak plasmas must be due to an "anomalous" effect. For clarification, in this research "neoclassical" refers to the classical transport plus the transport due to toroidal geometry (i.e., Pfirsch-Schluter (PS) transport) and trapped particle effects.

What generally has not been accounted for in these early neoclassical studies [14, 15, 18, 19] is the GYROVISCOUS contribution to the radial angular momentum transport, which is larger than the PERPENDICULAR viscosity component by several

orders of magnitude when significant up-down asymmetries are present [12, 13]. This gyroviscous contribution vanishes in classical cylindrical geometry and appears only at a higher gyroradius order in neoclassical theories. Even more advanced neoclassical theories [18, 19, 25] which do not treat poloidal dependencies (geometric expansion and compression) of density and velocity in the formalism failed to properly calculate the gyroviscous transport contribution, but recovered only the much smaller perpendicular viscosity. However, there exist several theoretical studies [12, 13, 16, 17, 20-24, 26-28] that have provided a firm theoretical basis for the importance of gyroviscosity relative to perpendicular viscosity.

Motivated by the indicated importance of neoclassical gyroviscosity, studies with a simple circular flux surface geometry (the "circular model") [29-33] were previously carried out to calculate toroidal velocity and the related gyroviscous momentum transport, taking into account density and velocity asymmetries in the formalism. These studies established that gyroviscosity predicts the right order of magnitude of the toroidal velocity, thus demonstrating the greater importance of the gyroviscous contribution relative to the much smaller perpendicular transport. The calculated carbon toroidal velocities, however, were about a factor of two larger (e.g. Ref. [30]) than the experimental measurement, indicating either that the approximations in the representation of important poloidal asymmetries made in the “circular gyroviscous model” were too crude or that other equally significant momentum transport mechanisms must be present, or both.

One gross approximation in the circular model studies [29-33] is believed to be the representation of the actual D-shaped equilibrium flux surfaces with a circular geometry, which limits the accuracy in the calculation of poloidal dependences of density and velocity. In these previous studies, it was shown that the angular momentum transport rates are strong functions of these poloidal asymmetries. Thus, without a more accurate representation of the poloidal dependences along the flux surfaces, it was not

possible to determine how well the extended neoclassical rotation theory could predict rotation. This observation has motivated the development of a new extended neoclassical plasma rotation theory based on the more accurate flux surface geometry given by the Miller equilibrium flux surface geometry (the "Miller model" hereafter) [34] that became available in 1998 [35, 36].

Therefore, the main objectives of this research are i) to present the theoretical development of a new extended neoclassical rotation and transport theory based on the Miller model representation of poloidal asymmetries, and ii) to compare the calculated poloidal and toroidal rotation velocities with measurements made in two recent DIII-D discharges [37] to verify the new theory. The implication of the results to the general question of the adequacy of neoclassical rotation calculations in accounting for rotation in tokamaks is discussed. To fulfill the second objective, an effective and robust nonlinear algorithm was designed to solve the resultant coupled system of nonlinear equations. The challenges in the numerical analysis of the extended neoclassical rotation theory based on the Miller model and the chosen numerical methods are also discussed in detail in Chapter 5.

CHAPTER 2

PLASMA FLUID EQUATIONS

2.1 Plasma Fluid Equations in Curvilinear Geometry

The motions of charged particles in plasmas are governed by the continuity, momentum balance, and energy balance equations shown below with " j " being species (ions or electrons).

Continuity equation: $$\frac{\partial n_j}{\partial t} + \nabla \cdot (n_j \vec{V}_j) = S_j^{\,o} \tag{1}$$

Momentum balance equation:

$$m_j \frac{\partial}{\partial t}(n_j \vec{V}_j) + n_j m_j \nabla \cdot \left(\vec{V}_j \vec{V}_j\right) + \nabla P_j + \nabla \cdot \vec{\vec{\Pi}}_j = n_j e_j (\vec{E} + \vec{V}_j \times \vec{B}) + \vec{F}_j^{\,1} + \vec{S}_j^{\,1} \tag{2}$$

Energy balance equation:

$$\frac{\partial}{\partial t}\left(\frac{1}{2} TrM_j\right) + \nabla \cdot \left(\frac{1}{2} n_j m_j V_j^{\,2} \vec{V}_j + \frac{5}{2} n_j T_j \vec{V}_j + \vec{\vec{\Pi}}_j \cdot \vec{V}_j + \vec{q}_j\right) = n_j e_j \vec{V}_j \cdot \vec{E} + F_j^{\,2} + S_j^{\,2} \tag{3}$$

where TrM_j is the scalar trace of the momentum stress tensor

$$\vec{\vec{\mathbf{M}}}_j \equiv n_j m_j \left\langle \vec{V}_j \vec{V}_j \right\rangle_j = n_j m_j \vec{V}_j \vec{V}_j + \frac{1}{3}\left(TrP_j\right)\vec{\vec{\mathbf{I}}} + \vec{\vec{\Pi}}_j, \tag{4}$$

$\vec{F}_j$ is the friction, and $\vec{q}_j = -n_j \chi_j \nabla T_j$ is the heat conduction relation. The first and second term in the momentum balance equation, Eq. (2), can be expanded as

$$m_j \frac{\partial}{\partial t}(n_j \vec{V}_j) = m_j \vec{V}_j \frac{\partial n_j}{\partial t} + n_j m_j \frac{\partial \vec{V}_j}{\partial t}, \tag{5}$$

$$n_j m_j \nabla \bullet (\vec{V}_j \vec{V}_j) = n_j m_j \left(\vec{V}_j \bullet \nabla\right)\vec{V}_j + m_j \vec{V}_j \nabla \bullet \left(n_j \vec{V}_j\right). \tag{6}$$

When multiplying the Continuity equation by $m_j \vec{V}_j$, we obtain

$$m_j \vec{V}_j \frac{\partial n_j}{\partial t} = m_j \vec{V}_j S_j^{\,o} - m_j \vec{V}_j \nabla \cdot (n_j \vec{V}_j) \tag{7}$$

which when replacing the first term in Eq. (5) its second term cancels out the second term in Eq. (6), thus yielding the basic form of the momentum balance equation used in this research.

$$n_j m_j \frac{\partial \vec{V}_j}{\partial t} + n_j m_j \left(\vec{V}_j \bullet \nabla\right)\vec{V}_j + \nabla P_j + \nabla \cdot \vec{\vec{\Pi}}_j = n_j e_j (\vec{E} + \vec{V}_j \times \vec{B}) + \vec{F}_j^{\,1} + \vec{S}_j^{\,1} - m_j \vec{V}_j S_j^{\,o} \tag{8}$$

The viscosity tensor($\vec{\vec{\Pi}}_j$) can be represented in (at least) two different ways by different ordering arguments. The short mean free path (i.e., highly collisional or Pfirsch-Schluter) description of viscosity, originally formulated by Braginskii [13], assumes a "strong rotation" ordering in which ion mean flow is on the order of ion thermal speed, $|V_\perp| \ll |V_\parallel| \sim V_{th}$ where V_{th} is the ion thermal velocity. Mikhailovskii and Tsypin [16] realized that this ordering is not one of the most interest in many practical situations, as in the plasma edge region or in discharges with slow rotation, and assumed ion mean flow to be on the order of the diamagnetic drift velocity, thus $|V_\parallel| \ll V_{th}$ in this "weak rotation" ordering. In reducing the plasma fluid equations to derive a neoclassical plasma rotation theory, either Braginskii's or Mikhailovskii's viscosity formalism may be employed if the corresponding ordering conditions are satisfied. For this research, we limit the scope of the research to Braginskii's ordering since it is valid for strongly rotating tokamak plasmas heated with directed neutral beam injection, except in the edge region. Using this ordering will enable us to check the validity of the new extended neoclassical rotation theory against measurements with significant rotation, presumably involving less experimental uncertainty. The extension of the present theory to Mikhailovskii's ordering is a useful topic for future research.

Applying Braginskii viscosity formalism to axisymmetric ($\partial/\partial\phi = 0$) toroidal flux surface geometry [17], which is eventually the "Pfirsch-Schluter" extension of classical gyroviscosity, the steady-state plasma fluid equations are reduced to Eqs. (9)-(12). Note

that the momentum balance equation is composed of three scalar components (r,θ,ϕ) and that the energy balance equation is not needed in this study with Braginskii's ordering (but would be included in future weak rotation studies).

Continuity equation:

$$\frac{1}{h_r}\frac{\partial}{\partial r}\left(n_j V_{rj}\right)+\frac{n_j V_{rj}}{h_r}\left(\frac{1}{h_\phi}\frac{\partial h_\phi}{\partial r}+\frac{1}{h_\theta}\frac{\partial h_\theta}{\partial r}\right)+\frac{1}{h_\theta}\frac{\partial}{\partial \theta}\left(n_j V_{\theta j}\right)+\frac{n_j V_{\theta j}}{h_\theta}\left(\frac{1}{h_\phi}\frac{\partial h_\phi}{\partial \theta}+\frac{1}{h_r}\frac{\partial h_r}{\partial \theta}\right) \quad (9)$$
$$=n_e\left(n_{oj}\left\langle\sigma V\right\rangle_{ionj}\right)\equiv n_e \nu_{ionj}$$

Radial momentum balance equation:

$$n_j m_j\left[\left(\vec{V}_j\bullet\nabla\right)\vec{V}_j\right]_r+\frac{1}{h_r}\frac{\partial p_j}{\partial r}+\left(\nabla\bullet\vec{\vec{\Pi}}_j\right)_r \quad (10)$$
$$=n_j e_j\left(E_r+V_{\theta j}B_\phi-V_{\phi j}B_\theta\right)+F_{rj}+\left(S_{rj}^1-m_j V_{rj}S_j^{\,0}\right)$$

Poloidal momentum balance equation:

$$n_j m_j\left[\left(\vec{V}_j\bullet\nabla\right)\vec{V}_j\right]_\theta+\frac{1}{h_\theta}\frac{\partial p_j}{\partial \theta}+\left(\nabla\bullet\vec{\vec{\Pi}}_j\right)_\theta \quad (11)$$
$$=n_j e_j\left(E_\theta-V_{rj}B_\phi\right)+F_{\theta j}+\left(S_{\theta j}^1-m_j V_{\theta j}S_j^{\,0}\right)$$

Toroidal momentum balance equation:

$$n_j m_j\left[\left(\vec{V}_j\bullet\nabla\right)\vec{V}_j\right]_\phi+\left(\nabla\bullet\vec{\vec{\Pi}}_j\right)_\phi=n_j e_j\left(\mathrm{E}_\phi^A+V_{rj}B_\theta\right)+F_{\phi j}+\left(S_{\phi j}^1-m_j V_{\phi j}S_j^{\,0}\right) \quad (12)$$

where h_r, h_θ and h_ϕ are differential metric coefficients (or scale factors) for a given flux surface geometry, which relate differential coordinates and their length elements by $dl_r=h_r dr$, $dl_\theta=h_\theta d\theta$, and $dl_\phi=h_\phi d\phi$. E_ϕ^A is the toroidal component of the inductive electric field $\vec{E}^A=-\partial\vec{A}/\partial t$. Details of representing the plasma fluid equations in general curvilinear geometry has been worked out earlier [36]. All coordinate components of the inertial term, $\left[\left(\vec{V}\bullet\nabla\right)\vec{V}\right]$, and the viscous term, $\left(\nabla\bullet\vec{\vec{\Pi}}\right)$, can be found in Appendix A.

To acquire relations required to solve for rotation velocities and poloidal asymmetries, further approximations are made to Eqs. (9)-(12) by introducing the strong

rotation ordering to eliminate negligible terms. We start by neglecting radial velocities because $V_r \ll V_\theta < V_\phi$ holds in tokamak plasmas. The continuity equation then becomes

$$\frac{1}{h_r}\frac{\partial}{\partial r}\left(n_j V_{rj}\right)+\frac{1}{h_\theta}\frac{\partial}{\partial \theta}\left(n_j V_{\theta j}\right)+\frac{n_j V_{\theta j}}{h_\theta}\left(\frac{1}{h_\phi}\frac{\partial h_\phi}{\partial \theta}+\frac{1}{h_r}\frac{\partial h_r}{\partial \theta}\right)=n_e \nu_{ionj} \tag{13}$$

Assuming that all other terms except the pressure gradient and electromagnetic force terms are negligible, the radial momentum balance equation reduces to

$$\frac{1}{h_r}\frac{\partial P_j}{\partial r}=n_j e_j\left(E_r+V_{\theta j}B_\phi-V_{\phi j}B_\theta\right)=n_j e_j\left(-\frac{1}{h_r}\frac{\partial \Phi}{\partial r}+V_{\theta j}B_\phi-V_{\phi j}B_\theta\right) \tag{14}$$

where Φ is the electrostatic potential. In the poloidal momentum balance equation, Eq. (11), the inertial and viscous terms from Appendix A reduce to

$$\left[\left(\vec{V}\bullet\nabla\right)\vec{V}\right]_\theta=\frac{V_{\theta j}}{h_\theta}\frac{\partial V_{\theta j}}{\partial \theta}-\frac{V_{\theta j}V_{\phi j}}{h_\theta h_\phi}\frac{\partial h_\phi}{\partial \theta}, \tag{15}$$

$$\begin{aligned}\left(\nabla\bullet\Pi\right)_\theta=&\frac{1}{H}\frac{\partial}{\partial r}\left(Rh_\theta\Pi_{r\theta}\right)+\frac{1}{H}\frac{\partial}{\partial \theta}\left(h_r h_\phi\Pi_{\theta\theta}\right)\\&-\frac{1}{h_\theta h_r}\frac{\partial h_r}{\partial \theta}\Pi_{rr}+\frac{1}{h_\theta h_r}\frac{\partial h_\theta}{\partial r}\Pi_{\theta r}-\frac{1}{Rh_\theta}\frac{\partial R}{\partial \theta}\Pi_{\phi\phi}\end{aligned} \tag{16}$$

where $H=h_r h_\theta h_\phi$. In the toroidal momentum balance equation, Eq. (12), the inertial and viscous terms in Appendix A are reduce to

$$\left[\left(\vec{V}\bullet\nabla\right)\vec{V}\right]_\phi=\left(\frac{V_{rj}}{h_r}\frac{\partial V_{\phi j}}{\partial r}+\frac{V_{\phi j}V_{rj}}{h_\phi h_r}\frac{\partial h_\phi}{\partial r}\right)+\left(\frac{V_{\theta j}}{h_\theta}\frac{\partial V_{\phi j}}{\partial \theta}+\frac{V_{\phi j}V_{\theta j}}{h_\phi h_\theta}\frac{\partial h_\phi}{\partial \theta}\right), \tag{17}$$

$$\left(\nabla\bullet\Pi\right)_\phi=\left[\frac{1}{Rh_\theta h_r}\frac{\partial}{\partial r}\left(Rh_\theta\Pi_{r\phi}\right)+\frac{1}{Rh_r}\frac{\partial R}{\partial r}\Pi_{r\phi}\right]+\left[\frac{B_\theta}{h_\theta}\frac{\partial}{\partial \theta}\left(\frac{\Pi_{\theta\phi}}{B_\theta}\right)+\frac{1}{Rh_\theta}\frac{\partial R}{\partial \theta}\Pi_{\theta\phi}\right]. \tag{18}$$

These reduced forms of the continuity and momentum balance equations constitute the basic set of relations required to develop any plasma rotation theory in strongly rotating plasmas. In this study, an extended neoclassical rotation theory based on the Miller geometry is developed for a two-species "deuterium-carbon" plasma for simplicity but can also be extended to multiple ion species by summing over all ion species to calculate the friction term and the electron density from charge neutrality.

2.2 Extended Stacey-Sigmar Poloidal Rotation Model

Quite different plasma poloidal rotation theories can be developed from the same basic set of equations in the previous section, based on which terms are retained in the momentum balance equations and how the viscosity and poloidal dependences of density and velocity are represented in Eqs. (9)-(12). One of the biggest differences among existing theories is the number of terms retained in the poloidal momentum balance, Eq. (11). Such differences in poloidal rotation calculation models ultimately affect the toroidal velocity calculations. One of the early poloidal rotation models is based on the Hirshman-Sigmar poloidal rotation theory (the H-S model) [38], which neglects all terms except the viscosity and friction terms, which are treated with a sophisticated friction and viscosity representation. This model is used in the NCLASS code [39]. The model by Kim, Diamond, and Groebner (the KDG model) [40], is a trace-impurity approximation to the H-S model. The Shaing-Sigmar-Stacey (the S-S-S model) [1] retain more terms in the poloidal momentum balance equation and calculates poloidal density asymmetries to represent poloidal dependences. The most recent form of neoclassical poloidal rotation theory evolved from the S-S-S model is the Stacey-Sigmar poloidal rotation model (the "S-S model" hereafter) [20, 30, 41], which uses the generalized curvilinear form of Braginskii flow rate-of-strain tensor (see Appendix A) [36, 42] and retains all terms to obtain

$$\begin{aligned} & n_j m_j \left[\left(\vec{V}_j \bullet \nabla \right) \vec{V}_j \right]_\theta + \left(\nabla \bullet \vec{\vec{\Pi}}_j \right)_\theta + \frac{1}{h_\theta} \frac{\partial p_j}{\partial \theta} - M_{\theta j} + n_j m_j \nu_{jk} \left(V_{\theta j} - V_{\theta k} \right) \\ & + n_j e_j \left(V_{rj} B_\phi - E_\theta \right) + n_j m_j \nu_{ionj} V_{\theta j} + n_j m_j \nu_{elcxj} V_{\theta j} = 0 \end{aligned} \tag{19}$$

which is basically Eq. (11) rewritten with the source and friction terms replaced with actual calculation models. The third term in Eq. (19) is the pressure gradient. The fourth term $\left(M_{\theta j} \right)$ represents any external poloidal momentum input or torque and comes from representing the momentum source term as the momentum input minus momentum

damping due to charge exchange and elastic scattering of rotating ions with non-rotating neutrals, as in

$$\vec{\mathbf{S}}_j^{\,1} = \overrightarrow{M}_j - n_j m_j \nu_{elcxj} \vec{V}_j . \tag{20}$$

The fifth term is the interspecies collisional friction and a simple Lorentz form, $\overrightarrow{F}_j^1 = -n_j m_j \sum_k \nu_{jk} \left(\vec{V}_j - \vec{V}_k \right)$, is used in this study. The sixth term is a combination of $\vec{V} \times \vec{B}$ force and electric field force, the seventh term comes from the right-hand side of Eq. (13), and the last term comes from the 2nd term in Eq. (20). This S-S model also replaces the parallel viscosity coefficient in the H-S model with the Shaing banana-plateau-PS viscosity interpolation formula

$$\eta_{0j} = \frac{n_j m_j V_{thj} q R_0 \varepsilon^{-3/2} \nu_{jj}^*}{\left(1+\varepsilon^{-3/2}\nu_{jj}^*\right)\left(1+\nu_{jj}^*\right)} \equiv n_j m_j V_{thj} q R f_j\left(\nu_{jj}^*\right) \tag{21}$$

where the normalized collision frequency is $\nu_{jj}^* \equiv \nu_{jj}\, qR_0 / V_{thj}$ with ν_{jj} being the self-collision frequency of species " j ", q is the safety factor, and $\varepsilon \equiv r/R_0$ [17, 42].

In the S-S poloidal rotation model, the poloidal dependences of density and velocity over flux surfaces are represented by the following low-order Fourier expansion,

$$n_j(r,\theta) \approx \overline{n}_j(r)\left[1 + n_j^c(r)\cos\theta + n_j^s(r)\sin\theta\right], \tag{22a}$$

$$V_j(r,\theta) \approx \overline{V}_j(r)\left[1 + V_j^c(r)\cos\theta + V_j^s(r)\sin\theta\right] \tag{22b}$$

where the overbar indicates the average values over flux surfaces, the cosine asymmetries with superscript "c" represent "in-out" variations, and the sine asymmetries with superscript "s" represents "up-down" asymmetries. More details on the S-S poloidal rotation model can be found in Refs. [17] and [42].

Earlier studies with the S-S model [29-33] have developed an extended neoclassical rotation theory based on the circular flux surface geometry and the calculations were compared to actual velocity measurements [30]. Although the

calculated toroidal velocities were off by about a factor of two, these studies proved the possibility of using simple analytic flux surface geometry models in this type of neoclassical rotation and the related momentum transport calculations but concluded that higher accuracy could be achieved with a more accurate flux surface geometry since poloidal asymmetries are closely related to the geometric expansion, compression, and elongation of flux surfaces [30]. These findings have motivated the use of the Miller flux surface geometry to rederive an extended neoclassical rotation theory [35] based on the S-S poloidal rotation model.

2.3 Miller Equilibrium Flux Surface Model

The circular model was rather simpler in terms of the derivation and numerical coding but lacks the accuracy in the representation of poloidal dependences along the flux surfaces. Miller et al. [34] presented an analytical geometry to better describe actual D-shaped equilibrium flux surfaces of tokamak plasmas with elongation κ and triangularity δ as shown in Fig. 1, thus one of the most advanced analytic representations of the flux surfaces in tokamak plasmas. $R_0(r)$ is a function of r, the half-diameter from the center of plasma along the plasma mid-plane, representing the

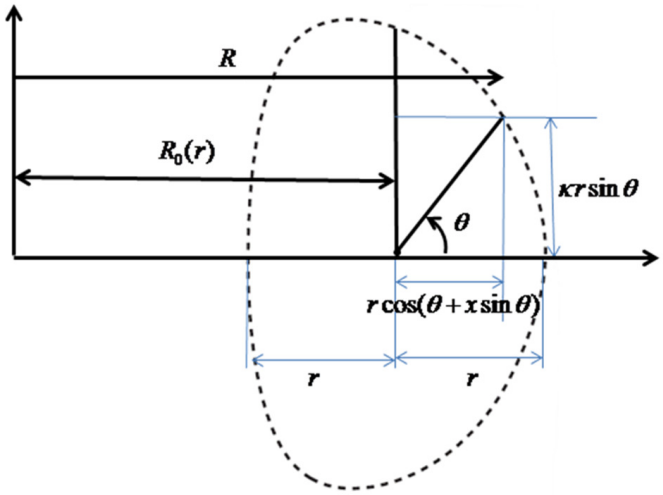

Figure 1. Miller equilibrium flux surface geometry.

shifts of the center of each flux surface. The R and Z coordinates of the Miller model are described by

$$R(r) = R_0(r) + r\cos(\theta + x\sin\theta) \equiv R_0(r) + r\cos\xi, \tag{23a}$$

$$Z(r) = \kappa r\sin\theta \tag{23b}$$

where $x \equiv \sin^{-1}\delta$ and $\xi \equiv \theta + x\sin\theta$.

Analysis of the curvilinear differential geometry in all coordinates(r, θ, ϕ) yields the following metric coefficients for the Miller model [34, 35, 43],

$$h_r = \frac{\kappa\left[\cos(x\sin\theta) + \frac{\partial R_0(r)}{\partial r}\cos\theta + \left[s_\kappa - s_\delta\cos\theta + (1+s_\kappa)x\cos\theta\right]\sin\theta\sin\xi\right]}{\sqrt{\sin^2\xi(1+x\cos\theta)^2 + \kappa^2\cos^2\theta}}, \tag{24}$$

$$h_\theta = \frac{r\kappa\left[\cos(x\sin\theta) + \frac{\partial R_0(r)}{\partial r}\cos\theta + \left[s_\kappa - s_\delta\cos\theta + (1+s_\kappa)x\cos\theta\right]\sin\theta\sin\xi\right]}{\sqrt{\left(\frac{\partial R_0}{\partial r} + \cos\xi - s_\delta\sin\xi\sin\theta\right)^2 + \kappa^2\sin^2\theta(s_\kappa+1)^2}}, \tag{25}$$

$$h_\phi = R(r) = R_0(1+\varepsilon\cos\xi) \tag{26}$$

where $s_\kappa(r) = r/\kappa(\partial\kappa/\partial r)$ and $s_\delta(r) = r(\partial\delta/\partial r)/\sqrt{(1-\delta^2)}$ account for the changes in elongation and triangularity respectively along the radial direction. Ampere's law provides the following magnetic field representations for the Miller model.

$$B_\theta(r,\theta) = \left(1 + \frac{\partial R_0(r)}{\partial r}\right)\frac{\overline{B}_\theta}{h_r(1+\varepsilon\cos\xi)} \tag{27}$$

$$B_\phi = \frac{\overline{B}_\phi}{1+\varepsilon\cos\xi} \tag{28}$$

With this analytical Miller model, we can use the S-S poloidal rotation model to calculate the poloidal dependences of density and velocity represented in Eqs. (22a) and (22b) more accurately, ultimately increasing the accuracy in the toroidal velocity and momentum transport calculations.

Different flux surface geometries provide different formulas for the flux surface average (FSA) calculations. For the Miller model, we have

$$\left\langle A(r,\theta)\right\rangle \equiv \frac{\oint \frac{A(r,\theta)d\ell_\theta}{B_\theta}}{\oint \frac{d\ell_\theta}{B_\theta}} = \frac{\oint A(r,\theta)Y(r,\theta)d\theta}{\oint Y(r,\theta)d\theta} \tag{29}$$

where

$$Y(r,\theta) = \frac{(1+\varepsilon\cos\xi)\left[\cos(x\sin\theta)+\frac{\partial R_0(r)}{\partial r}\cos\theta+\left[s_\kappa - s_\delta\cos\theta+(1+s_\kappa)x\cos\theta\right]\sin\theta\sin\xi\right]^2}{\sqrt{\left[\left(\frac{\partial R_0}{\partial r}+\cos\xi-s_\delta\sin\xi\sin\theta\right)^2+\kappa^2\sin^2\theta(s_\kappa+1)^2\right]\left[\sin^2\xi(1+x\cos\theta)^2+\kappa^2\cos^2\theta\right]}}.$$

Unlike those of the circular model used in earlier studies [29-33], FSAs in the Miller model do not reduce to simple analytic forms, thus must be numerically computed separately and imported into the final computation code. Note here that the circular model is simply a special case of the Miller model with elongation $\kappa = 1$, triangularity $\delta = 0$ and no Shafranov shift. This simple fact served as one of the tools to check the accuracy and validity of the new plasma rotation theory against the earlier circular model study [29, 30] (see Appendix B for revised circular model formalism) and for the numerical coding in this work.

CHAPTER 3

EXTENDED NEOCLASSICAL ROTATION THEORY IN THE MILLER MODEL REPRESENTATION

3.1 Angular Toroidal Torques and Transport with the Miller Geometry

Now with all theoretical backgrounds required to develop a new extended neoclassical rotation theory with the Miller geometry presented, we are ready to derive the formalism for calculating toroidal velocity and neoclassical gyroviscous contribution to angular momentum damping. Earlier studies with the circular model [29-33] now become special cases of this new theory. Thus, the new theory with the Miller model was developed in a similar fashion to the circular model study [30] so that direct comparison would be possible to enable evaluation of the accuracy improvement. In this chapter, derivation of the toroidal angular torque formalism is presented first to stress the importance of the gyroviscous contribution to the total viscous torque.

From the first term of the toroidal momentum balance equation, Eq. (12), the FSA of toroidal angular "inertial" torque using the Miller model is given by

$$\left\langle n_j m_j R^2 \nabla\phi \bullet \left(\vec{V}_j \bullet \nabla\right)\vec{V}_j \right\rangle = R_0 \overline{n}_j m_j \nu_{nj} \overline{V}_{\phi j} \tag{30}$$

with the "inertial" transport frequency (ν_{nj}),

$$\begin{aligned} \nu_{nj} = {} & \frac{\overline{V}_{rj}}{R_0}\left[\frac{\partial R_0}{\partial r}\left\langle\frac{1}{h_r}\right\rangle + \left\langle\frac{\cos\xi}{h_r}\right\rangle + \varepsilon\left(\tilde{n}_j^c + \tilde{V}_{\phi j}^c\right)\left\langle\cos\theta\frac{\cos\xi}{h_r}\right\rangle - R_0 L_{\overline{V}_\phi}^{-1}\right] \\ & + \overline{V}_{\theta j}\varepsilon\tilde{V}_{\phi j}^s\left(\left\langle\cos\theta\frac{1}{h_\theta}\right\rangle + \frac{\left\langle\frac{1}{R}\frac{\partial R}{\partial\theta}\sin\theta\frac{1}{h_\theta}\right\rangle}{\left\langle\sin^2\theta\frac{1}{h_\theta}\right\rangle}\left\langle\cos^2\theta\frac{1}{h_\theta}\right\rangle + \varepsilon\left\langle\cos\theta\frac{\cos\xi}{h_\theta}\right\rangle + \frac{1}{R_0}\left\langle\frac{\partial R}{\partial\theta}\sin\theta\frac{1}{h_\theta}\right\rangle\right) \end{aligned} \tag{31}$$

where $L_X^{-1} = -1/X\left(\partial X/\partial r\right)$ is the gradient length scales for a given quantity X,

$\tilde{n}_j^{s,c} = n_j^{s,c}/\varepsilon$, and $\widetilde{V}_{\phi j}^{c,s} \equiv V_{\phi j}^{c,s}/\varepsilon$.

Also from the 2nd term of the toroidal momentum balance equation, Eq. (12), the FSA of toroidal angular "viscous" torque is given by

$$\begin{aligned}\left\langle R^2\nabla\phi\bullet\nabla\bullet\overleftrightarrow{\mathbf{\Pi}}\right\rangle &= \left\langle\left(R^2\nabla\phi\bullet\nabla\bullet\overleftrightarrow{\mathbf{\Pi}}\right)_{\perp}\right\rangle + \left\langle\left(R^2\nabla\phi\bullet\nabla\bullet\overleftrightarrow{\mathbf{\Pi}}\right)_{gv}\right\rangle \approx \left\langle\left(R^2\nabla\phi\bullet\nabla\bullet\overleftrightarrow{\mathbf{\Pi}}\right)_{gv}\right\rangle \\ &= -\left\langle\frac{1}{Rh_\theta h_r}\frac{\partial}{\partial r}\left[R^3\eta_4\frac{\partial\left(V_\phi R^{-1}\right)}{\partial\theta}\right]\right\rangle = R_0\bar{n}_j m_j \nu_{dj}\overline{V}_{\phi j}\end{aligned} \tag{32}$$

where $\eta_{4j} = n_j m_j T_j/\left(e_j B\right)$ and the gyroviscous transport (or "drag") frequency is

$$\nu_{dj} \approx \nu_{dj}^1 + \nu_{dj}^2 \tag{33}$$

with

$$\nu_{dj}^1 = -\frac{T_j}{R_0 e_j \overline{B}_\phi}\varepsilon\left[\begin{array}{l}\widetilde{V}_{\phi j}^s\left(\begin{array}{l}2\left\langle\cos\theta\dfrac{\cos\xi}{h_\theta h_r}\right\rangle + \dfrac{1}{R_0}\left\langle R\cos\theta\dfrac{\cos\xi}{h_\theta h_r}\right\rangle \\ +\dfrac{1}{R_0}\left\langle R\sin\theta\dfrac{\sin\xi}{h_\theta h_r}\right\rangle + \dfrac{1}{R_0}x\left\langle R\sin\theta\cos\theta\dfrac{\sin\xi}{h_\theta h_r}\right\rangle\end{array}\right) \\ +\tilde{n}_j^s\dfrac{1}{R_0}\left(\left\langle R\sin\theta\dfrac{\sin\xi}{h_\theta h_r}\right\rangle + x\left\langle R\sin\theta\cos\theta\dfrac{\sin\xi}{h_\theta h_r}\right\rangle\right)\end{array}\right], \tag{34}$$

$$\nu_{dj}^2 \equiv \frac{1}{2}\frac{\tilde{\theta}_j G_j T_j}{R_0^{\,2} e_j B_\phi} \tag{35}$$

where

$$G_j \equiv r\left(L_{\bar{n}_j}^{-1} + L_{T_j}^{-1} + L_{\overline{V}_{\phi j}}^{-1}\right), \tag{36}$$

$$\tilde{\theta}_j = 2\varepsilon\left[\begin{array}{l}\widetilde{V}_{\phi j}^s\left(\begin{array}{l}\tilde{n}_j^c\left\langle R\dfrac{\cos^2\theta}{h_\theta h_r}\right\rangle + \dfrac{1}{\varepsilon}\left\langle R\dfrac{\cos\theta}{h_\theta h_r}\right\rangle + \left\langle R\cos\theta\dfrac{\cos\xi}{h_\theta h_r}\right\rangle \\ +\left\langle R\sin\theta\dfrac{\sin\xi}{h_\theta h_r}\right\rangle + x\left\langle R\sin\theta\cos\theta\dfrac{\sin\xi}{h_\theta h_r}\right\rangle\end{array}\right) \\ +\tilde{n}_j^s\left(-\widetilde{V}_{\phi j}^c\left\langle R\dfrac{\sin^2\theta}{h_\theta h_r}\right\rangle + \left\langle R\sin\theta\dfrac{\sin\xi}{h_\theta h_r}\right\rangle + x\left\langle R\sin\theta\cos\theta\dfrac{\sin\xi}{h_\theta h_r}\right\rangle\right)\end{array}\right]. \tag{37}$$

Earlier circular model studies [29-33] were done with ν_{dj}^{2} only, but ν_{dj}^{1} was identified to have non-negligible contribution during the numerical calculation in this work, thus included for both the Miller model and the revised circular model theories (see Appendix B for the revised circular model formalism). ν_{dj}^{2} contains the same G_j and $\tilde{\theta}_j$ representing the radial gradients and poloidal asymmetries respectively, thus allowing direct comparison with the earlier circular model formalism [29-33]. Note here in Eq. (32) that the gyroviscous contribution accounts for the most of the viscous torque since it is much larger than the perpendicular component by the following argument. Braginskii's parallel (η_0), gyroviscous $(\eta_{3,4})$, and perpendicular $(\eta_{1,2})$ viscosity coefficients in a collisional plasma are given as follows, expressed with their relative orderings,

$$\eta_0 = 0.96nT\tau, \quad \eta_1 = \frac{3}{10}\frac{nT}{\Omega^2\tau}, \quad \eta_2 = 4\eta_1, \quad \eta_3 = \frac{1}{2}\frac{nT}{\Omega}, \quad \eta_4 = 2\eta_3 \tag{38}$$

where in tokamak plasmas $\tau \sim 10^{-5}\ s$ is the typical self-collision time and $\Omega \sim 10^{8}\ s^{-1}$ is the typical ion gyrofrequency. Thus, Braginskii's parallel, gyroviscous, and perpendicular viscosity coefficients are in the ratio of $1/(\Omega\tau)^{-1}/(\Omega\tau)^{-2} \approx 1/10^{-3}/10^{-6}$. Therefore, the ordering among these components are given by $\eta_0 \gg \eta_4 \gg \eta_2$. With the parallel contribution identically vanishing in the FSA and $\eta_4 \approx (\Omega\tau)\eta_2 \approx (10^{-3} \sim 10^{-4})\eta_2$, the gyroviscous contribution is the dominant one, larger than the perpendicular component generally by a couple of orders of magnitude.

Note here that the gyroviscous momentum transport frequency given by Eqs. (33)-(37) is a strong function of density and toroidal velocity asymmetries, thus vanishes in any formalism that neglects poloidal dependences. Also, although Braginskii's viscosity was derived assuming large collisionality, this Pfirsch-Schluter type "neoclassical" gyroviscosity is independent of any explicit collisionality since no direct evidence on the trapped particle effect on gyroviscosity has been reported. When the

poloidal asymmetries are not considered, as in the NCLASS code [39], only the perpendicular contribution survives and the calculated neoclassical momentum damping is negligible [18, 19, 25], leading to the incorrect conclusion that neoclassical transport is too small.

3.2 Stacey-Sigmar Poloidal Rotation Theory with the Miller Geometry

Calculation of the toroidal angular torques and transport rates in the previous section requires a calculation of the poloidal asymmetries ($n_j^{c,s}$ and $V_j^{c,s}$) appearing in Eqs. (22a) and (22b). This can be accomplished by taking Fourier moments (i.e., 1, cosine, and sine moments) of the poloidal momentum balance, Eq. (19), with Eqs. (22a) and (22b) assumed. Using the same Fourier moments of the continuity equation, Eq. (13), the velocity asymmetries ($V_j^{c,s}$) can be related to the density asymmetries ($n_j^{c,s}$) by

$$\widetilde{V}_{\theta j}^{s} \equiv V_{\theta j}^{s} \Big/ \varepsilon \approx -\tilde{n}_j^{s}, \tag{39}$$

$$\widetilde{V}_{\theta j}^{c} \equiv V_{\theta j}^{c} \Big/ \varepsilon = -\tilde{n}_j^{c} + \frac{1}{\varepsilon} \frac{\left\langle \frac{1}{R} \frac{\partial R}{\partial \theta} \sin\theta \frac{1}{h_\theta} \right\rangle}{\left\langle \sin^2\theta \frac{1}{h_\theta} \right\rangle} \tag{40}$$

to reduce the number of unknowns in the final computation model. We may consider adding an additional atomic physics term on the right-hand side of the continuity equation, Eq. (9), to increase the accuracy in the plasma edge region as in one of the early circular model studies [44] but this is left as a future research.

We also assume the same type of Fourier series expansion for the electrostatic potential,

$$\Phi(r,\theta) \approx \overline{\Phi}(r)\left[1 + \Phi^c(r)\cos\theta + \Phi^s(r)\sin\theta\right], \tag{41}$$

and use it in the moments of the poloidal momentum balance equation for " j = electrons" to relate the potential asymmetries ($\Phi^{c/s}$) to the electron density asymmetries ($n_e^{c/s}$). In

doing so, we neglect all other terms except the pressure and electric field terms in the poloidal momentum balance, Eq. (19), to yield

$$\overline{\Phi}\Phi^{c,s} = T_e n_e^{c,s} \big/ e \tag{42}$$

where $n_e^{c,s}$ are coupled with $n_j^{c,s}$ (j = ions) by the charge neutrality. The same Fourier moments of the radial momentum balance, Eq. (14), can be used to calculate the radial electric field, $\overline{E}_r$, and the toroidal velocity asymmetries ($V_{\phi j}^{c/s}$) as a function of $n_j^{c,s}$ as in Eqs. (43)-(45), again allowing the reduction in the number of unknowns in the numerical computation model. The 1, cosine, and sine moments of the reduced radial momentum balance, Eq. (14), are

$$\hat{\Phi}_j^{'} \equiv \frac{\overline{\Phi}^{'}}{V_{thj}} \equiv \frac{1}{V_{thj}\overline{B}_\theta}\frac{\partial \overline{\Phi}}{\partial r} = -\frac{\overline{E}_r}{V_{thj}\overline{B}_\theta} = \hat{V}_{\theta j}\frac{\left\langle \dfrac{1}{1+\varepsilon\cos\xi} \right\rangle}{\left\langle \dfrac{1}{h_r} \right\rangle} - \hat{V}_{\phi j}\left(1+\frac{\partial R_0(r)}{\partial r}\right)\frac{\left\langle \dfrac{1}{(1+\varepsilon\cos\xi)}\dfrac{1}{h_r} \right\rangle}{\left\langle \dfrac{1}{h_r} \right\rangle} - \hat{P}_j^{'} \tag{43}$$

where $\hat{P}_j^{'} \equiv \dfrac{\overline{P}_j^{'}}{V_{thj}} \equiv \dfrac{1}{V_{thj}}\dfrac{1}{\overline{n}_j e_j \overline{B}_\theta}\dfrac{\partial \overline{P}_j}{\partial r}$, $f_p \equiv B_\theta / B_\phi$, $\hat{V}_{\theta j} \equiv \overline{V}_{\theta j} \big/ \left(f_p V_{thj} \right)$, and $\hat{V}_{\phi j} \equiv \overline{V}_{\phi j} / V_{thj}$,

$$\tilde{V}_{\phi j}^{s} = \tilde{n}_j^{s}\alpha_j^{1S} + \alpha_j^{2S} \tag{44}$$

where α_j^{1S} and α_j^{2S} can be found in Appendix C, and

$$\begin{aligned} \tilde{V}_{\phi j}^{c} = \frac{\hat{V}_{\theta j}}{\hat{V}_{\phi j}} & \left(\alpha_j^{3C} + \alpha_j^{2C}\frac{\left\langle \dfrac{1}{1+\varepsilon\cos\xi} \right\rangle}{\left\langle \dfrac{1}{h_r} \right\rangle} \right) \\ & + \alpha_j^{1C} - \alpha_j^{2C}\left(1+\frac{\partial R_0(r)}{\partial r}\right)\frac{\left\langle \dfrac{1}{(1+\varepsilon\cos\xi)}\dfrac{1}{h_r} \right\rangle}{\left\langle \dfrac{1}{h_r} \right\rangle} - \frac{\hat{P}_j^{'}}{\hat{V}_{\phi j}}\left(\alpha_j^{2C} - \alpha_j^{4C}\right) \end{aligned} \tag{45}$$

where α_j^{1C}, α_j^{2C}, α_j^{3C}, and α_j^{4C} are all functions of $\tilde{n}_j^{c}$ and can be found in Appendix C.

Using all the coupling relations found so far, the first moment of the poloidal momentum balance reduces to Eq. (46a), written in a generic form for simplicity, that allows us to calculate the poloidal velocity for two ion species " j " and " k ",

$$A_{11}\hat{V}_{\theta j}{}^{2} + A_{12}\hat{V}_{\theta j} + A_{13}\hat{V}_{\theta k} = B_1 \tag{46a}$$

where A_{11}, A_{12}, A_{13}, and B_1 are given in Appendix C. In the numerical calculation model, the quadratic term in Eq. (46a) is treated iteratively

$$A_{11}\hat{V}_{\theta j}{}^{n}\hat{V}_{\theta j}{}^{n-1} + A_{12}\hat{V}_{\theta j}{}^{n} + A_{13}\hat{V}_{\theta k}{}^{n} = B_1{}^{n} \tag{46b}$$

as a linear term with n being the current iteration step and $n-1$ being the previous step. With the quadratic equation possibly having two solutions, this iteration helps steer the algorithm towards the solution that is near the initial guesses of poloidal velocities. In Eqs. (46), the friction term appears in $\nu^*_{jk} = \nu_{jk} qR / V_{thj}$ and the viscous term in $f_j = \varepsilon^{-3/2}\nu^*_{jj} \Big/ \left[\left(1+\varepsilon^{-3/2}\nu^*_{jj}\right)\left(1+\nu^*_{jj}\right)\right]$ from the use of neoclassical parallel viscosity expression, $\eta_{0j} = n_j m_j V_{thj} qR f_j\left(\nu^*_{jj}\right)$.

The cosine and sine moments of the poloidal momentum balance, Eq. (19), reduce to Eqs. (47) and (48) respectively (again in generic forms for the two species), to solve for $\tilde{n}_j^{c,s}$,

$$A_{C1}\tilde{n}_j^{c} + A_{C2}\tilde{n}_j^{s} + A_{C3}\tilde{n}_k^{c} = B_C, \tag{47}$$

$$A_{S1}\tilde{n}_j^{c} + A_{S2}\tilde{n}_j^{s} + A_{S3}\tilde{n}_k^{s} = B_S \tag{48}$$

where $A_{C,S}$ and $B_{C,S}$ coefficients are given in Appendix C. When we assume "two-species" plasma with the main ion (deuterium) and a majority impurity(carbon), Eqs. (46)-(48) provide six equations, with j being either deuterium or carbon and k being the other, leaving two more relations to be identified from the toroidal angular momentum balance for the calculation of toroidal velocities.

3.3 Toroidal Rotation Calculation Model with the Miller Geometry

The calculation model for the toroidal velocity can be derived from the toroidal component of the angular momentum balance,

$$\begin{aligned} & n_j m_j \left[R\left(\vec{V}_j \bullet \nabla\right)\vec{V}_j \right]_\phi + \left[R\left(\nabla \bullet \vec{\vec{\Pi}}_j\right) \right]_\phi \\ & = Rn_j e_j \mathrm{E}_\phi^A + Rn_j e_j V_{rj} B_\theta + RF_{\phi j} + RM_{\phi j} - Rn_j m_j \nu_{atomj} V_{\phi j}, \end{aligned} \tag{49}$$

from which we can get two additional relations to complete the eight equations to solve for the eight unknowns (4 velocities and 4 density asymmetries). Using the FSAs of first (inertial) and second (viscous) torque terms presented in Eqs. (30) and (32), we can take FSAs of all other terms in Eq. (49) to find relations for the toroidal velocity calculation. The first moment of Eq. (49) yields

$$\begin{aligned} & \overline{n}_j m_j \sum_k \overline{\nu}_{jk} \left[\left(1+\beta_j\right)\overline{V}_{\phi j} - \overline{V}_{\phi k} \right] \equiv \overline{n}_j m_j \sum_k \overline{\nu}_{jk} y_j \\ & = \overline{n}_j e_j E_\phi^A + \left(1 + \frac{\partial R_0(r)}{\partial r} \right) \left\langle \frac{1}{h_r} \right\rangle e_j \overline{B}_\theta \Gamma_{rj} + \overline{M}_{\phi j} \end{aligned} \tag{50}$$

where $\beta_j \equiv \left(\nu_{dj} + \nu_{nj} + S_{nbj} / \overline{n}_j\right) \Big/ \left(\overline{\nu}_{jk} + \overline{\nu}_{je}\right)$, $y_j \equiv \left(1+\beta_j\right)\overline{V}_{\phi j} - \overline{V}_{\phi k}$, and $\overline{M}_\phi$ is the toroidal momentum input. β_j represents the radial transport of angular momentum with S_{nbj} being the local neutral beam source rate and ν_{nj} and ν_{dj} are the inertial and gyroviscous transport frequencies respectively calculated with Eq. (31) and (33). Thus, a relation between the toroidal velocities of deuterium and impurity can be derived by adding y_j of the two species, $j = i$ (deuterium) and $j = I$ (carbon) with $V_{thi} = \sqrt{m_I / m_i}\, V_{thI}$ when assuming equilibrium temperature($T_i = T_I$). This yields

$$\widehat{V}_{\phi i} \sqrt{m_I / m_i}\, \beta_i + \widehat{V}_{\phi I} \beta_I = \left(y_i + y_I \right) \Big/ V_{thI} , \tag{51}$$

which becomes the 7th equation in the numerical computation model.

The last equation comes from manipulating the first moments of radial momentum balance, Eq. (43), for the two species. Since $\overline{\Phi}' \equiv 1 \Big/ \overline{B}_\theta \left(\partial \overline{\Phi} / \partial r \right)$ is

independent of species, it must be identical when calculated with either $j = i$ or $j = I$, thus providing

$$\widehat{V}_{\phi i} - \sqrt{\frac{m_i}{m_I}}\widehat{V}_{\phi I} = \left(\widehat{V}_{\theta i} - \sqrt{\frac{m_i}{m_I}}\widehat{V}_{\theta I}\right)\frac{\left\langle \frac{1}{1+\varepsilon\cos\xi}\right\rangle}{\left(1+\frac{\partial R_0(r)}{\partial r}\right)\left\langle \frac{1}{(1+\varepsilon\cos\xi)}\frac{1}{h_r}\right\rangle} + \left(-\widehat{P}^{'}_{i} + \sqrt{\frac{m_i}{m_I}}\widehat{P}^{'}_{I}\right)\frac{\left\langle \frac{1}{h_r}\right\rangle}{\left(1+\frac{\partial R_0(r)}{\partial r}\right)\left\langle \frac{1}{(1+\varepsilon\cos\xi)}\frac{1}{h_r}\right\rangle} \tag{52}$$

which is the last, 8th, relation that the toroidal velocities of both species must satisfy.

CHAPTER 4

EXPERIMENT RESULTS

Improvement of the extended neoclassical rotation theory in this research can be verified through the comparison of the calculated results with actual DIII-D [37] experimental measurements. In this chapter, a brief discussion on the rotation measurements in DIII-D is presented, followed by the detailed information on two DIII-D shots (discharges), shot #138639 and shot #142020, used for comparison with the theoretical calculations.

4.1 Rotation Experiment and Velocity Measurement in DIII-D Tokamak

In DIII-D tokamak, toroidal rotations are provided mainly by the neutral beam injections (NBI) except for other special purpose discharges. Figures 2 show the schematic alignment of the NBI ports in DIII-D with 30°, 150°, and 330° beamlines providing CCW-injections and 210° beamlines providing CW-injections when viewed from the top (notice that each has two beamlines). In this research, co- and counter-injection directions are determined relative to I_p direction with parallel direction being co- and anti-parallel being counter-injection. For two shots used in this research, neutral beams (dashed black lines) are injected from 30°, 150°, and 330° ports only, thus provides strong CCW-rotation for both discharges. 210° beamlines can also be used for either slow or intrinsic rotation discharges but not used for two shots selected for this research because the new extended rotation theory [42] needs to be verified with strong rotation shots. Figures 2 also show theoretical sign conventions for two shots in red (the directions of experimental parameters are shown in blue) that the users of the developed code, GTROTA (Georgia Tech ROTAtion), must ensure its correct directions (see Appendix E for the user's manual). Theoretical sign conventions in this research are

determined by the orthogonal coordinate system by a right-hand rule with the thumb pointing parallel to I_p direction. Therefore, for an accurate and reliable verification of the theory, the accurate input values with correct signs into GTROTA code become very important.

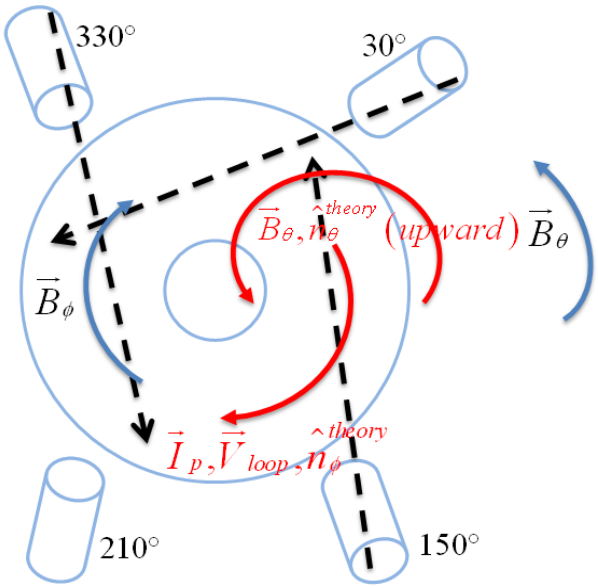

(a) Shot 138639 (ctr-injection)

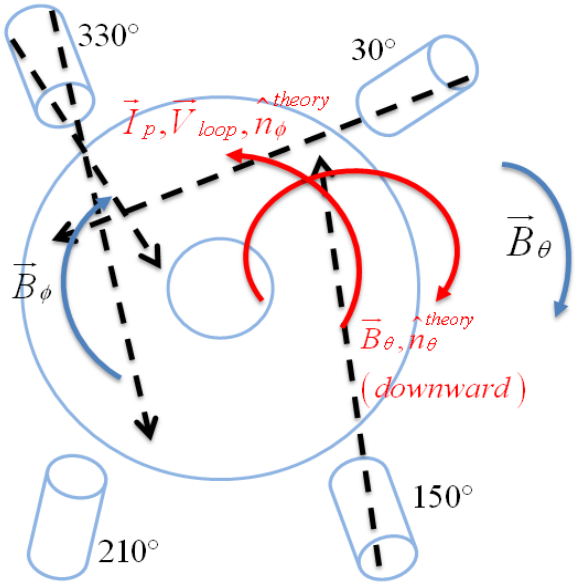

(b) Shot 142020 (co-injection)

Figure 2. Neutral beam injection configuration in DIII-D and sign conventions.

Measurement of rotation velocities in tokamaks are done with CER (Charge Exchange Recombination) diagnostic system [45-47] that measures the Doppler shift of the spectrum of light from an excited ions that have undergone charge exchange with beam neutrals [48]. There has been recent improvement in rotation measurement and analysis [47, 49, 50], motivating the comparison of theoretical calculations with recent shots to verify the new extended theory based on the Miller model. Figure 3(a) shows various diagnostic ports inside DIII-D and 3(b) shows the schematics of the recent CER viewing chords in DIII-D [51] modified to allow the measurement of deuterium velocities, which were not possible with earlier CER configurations. Availability of the measured deuterium velocities yields a great future research opportunity in verifying the theory and increasing the accuracy in prediction of other variables in the numerical model.

4.2 Experimental Data

Since the new extended neoclassical rotation theory was developed based on Braginskii's strong rotation orderings, two strongly rotating ELMing (Edge Localized Mode) H-mode DIII-D shots are analyzed in this research. One shot was counter-injection #138639 (2085 ms) and the other was co-injection #142020 (2310 ms). Summary of the shot parameters are provided in Table I. In this table, the impurity/deuterium density ratio shows the relative amount of impurities with respect to deuterium density. For example, shots 138639 has approximately 10% impurities on average with ~9% at the center and ~10% at the 90% flux surfaces. Throughout the radial ranges except the plasma edge, the ratio only slightly fluctuate about the average but the fluctuation increases at more than 90% flux surfaces where the ratio is not reliable due to lack of atomic physics treatment on the edge. The incident neutral beam power (P_{NB}) is given as the ratio of incident vs. capable neutral beam power, which is identical to the duty cycle, and also indicates which NBI beamlines were on for the given time for each shot. For example, the 30LT beam for shot 142020 (1.3 MW/2.6 MW) has the

(a) DIII-D interior with diagnostic ports [52]

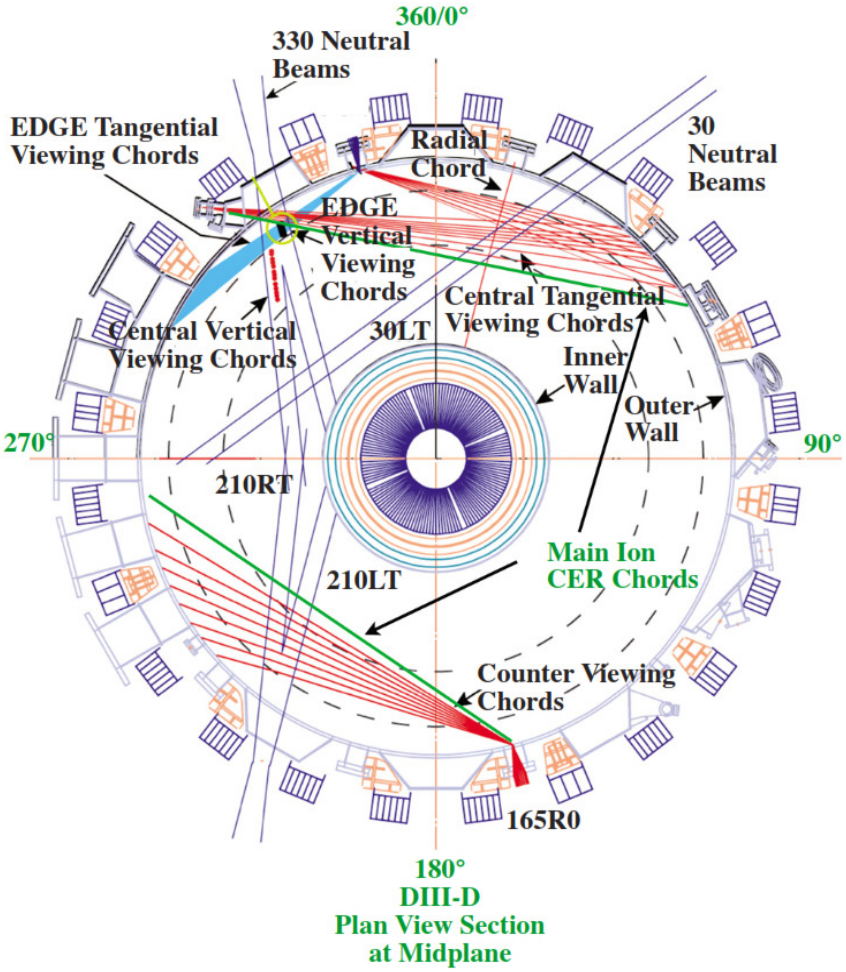

(b) CER viewing chords in DIII-D [51]

Figure 3. DIII-D tokamak and CER diagnostics.

capability of 2.6MW beam injection but used with 50% duty cycle, thus generating 1.3MW of beam injection energy. Figures 4 show the equilibrium flux surfaces for these two shots.

Table 1. Summary of two DIII-D shot parameters

Shot properties	shot 138639 (2085 ms)	shot 142020 (2310 ms)
Beam Injection Direction	Counter-injection	Co-injection
R (major radius)	1.734 m	1.796 m
a (minor radius)	0.586 m	0.592 m
$\kappa(r=0)/\kappa(r=a)$ (elongation)	1.45 / 1.83	1.39 / 1.85
$\delta(z_{\text{bottom}})/\delta(z_{\text{top}})$ (triangularity)	0.22 / 0.6	0.714 / 0.382
I (current)	-1.181 MW (CW from the top view)	1.074MW (CCW from the top view)
B_p (poloidal magnetic strength)	0.275 T	0.249 T
B_ϕ (toroidal magnetic strength)	-1.994 T	-1.897 T
q_{95} (safety factor at 95% flux surface)	4.9	5.63
V_{loop} (Loop Voltage)	-0.26296 V	0.315715 V
Divertor configuration	Upper Single Null(USN)	Lower Single Null(LSN)
Impurity/deuterium density ratio (average/at the center/at 95% flux surfaces)	0.1 / 0.09 / 0.1	0.04 / 0.04 / 0.05
P_{NB} (Incident Power/ Capable Power)	30LT (2.1/2.6 MW), 150LT (2.2/2.2 MW), 330LT (2.6/2.6 MW)	30LT (1.3 MW/2.6 MW), 150LT (1.8 MW/1.8 MW), 330LT (1.1 MW/2.2MW), 330RT (1.3 MW/2.2 MW)

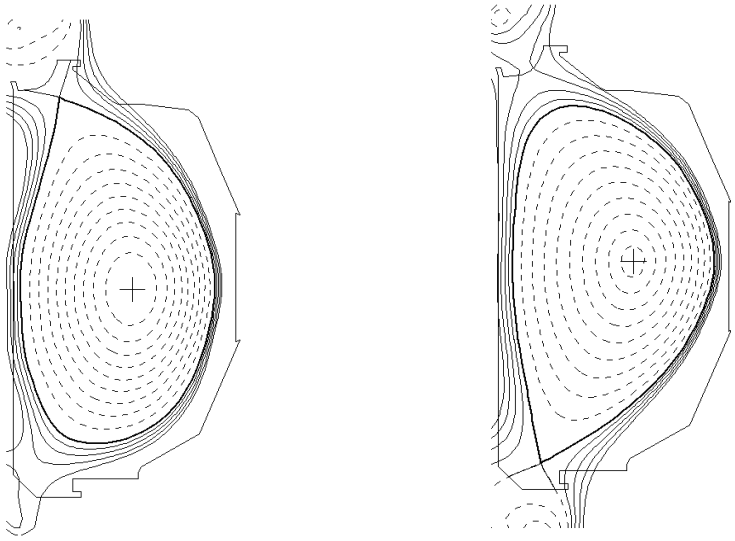

(a) shot 138639-2085ms **(b) shot 142020-2310ms**

Figure 4. Equilibrium flux surfaces of two DIII-D shots.

As mentioned, there have been recent advances in the measurements and analysis of toroidal and poloidal rotation, including proper treatment of the apparent velocity caused by the energy dependent cross-section [47, 49, 50], as well as extensions to the circular model theory since the earlier comparison [30]. Comparison of the calculated velocities from the new rotation theory against these measurements are presented in the following chapter. Although only two shots were analyzed in this research, a good combination of co- and counter-injection, different directions of B_θ and I_p, and the different extent of poloidal dependences of upper and lower divertors (as will be shown in the next chapter) enables a good test of the theory and the numerical algorithm. Efforts to identify more suitable shots are underway, especially shots which take advantage of the recent advances in the measurement of deuterium velocity and analysis [51].

CHAPTER 5

COMPARISON OF PREDICTION AND EXPERIMENT

5.1 Calculated Velocities and Density Asymmetries

The eight equations and eight unknowns provided in Chapter 3 constitute a self-consistent system of nonlinear equations, and its numerical calculation model and solution methodology is discussed in the next chapter. In this chapter we discuss the comparison of the calculated results and the actual measurement for both shots, which are provided in Figs. 5 and 6. For all the figures in this research, "t" represents "toroidal", "p" for "poloidal", "D" or "i" for deuterium, and "C" or "I" for carbon. In these figures $Vt_D^{computed}$ and $Vp_D^{computed}$ (blue diamonds) are the calculated, thus predicted, toroidal and poloidal deuterium velocities respectively for which no measurements are available. $\rho = r/a$ on the x-axis is the normalized distance from the center of plasma to the last closed flux surface (LCFS). Overall, these two sets of the calculated results show that the new extended neoclassical rotation theory based on the Miller equilibrium flux surface geometry predicts carbon toroidal and poloidal rotation velocities which agree quite well with measured values, generally to within approximately $<10\%$.

The notable exception of a significant under-prediction of the poloidal velocity in the edge region of the co-injected shot #142020 is probably attributable to not taking into account charge-exchange damping, the effect of divertor on poloidal asymmetry in the prediction, use of Braginskii's strong rotation ordering in the edge where rotation is much weaker, and ill-conditioning of the numerical calculation model in the edge. We note here that the Miller geometry does not represent the divertor x-point as a simple comparison of Figs. (1) and (4) indicates. It is uncertain at this point how the divertor x-point would affect the poloidal asymmetry calculation and whether it is related to the

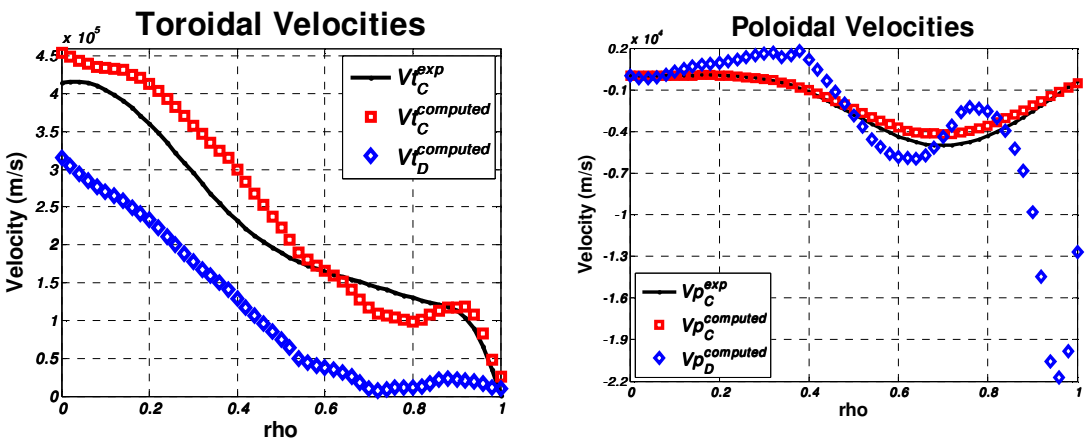

(a) $\overline{V}_\phi$ (CCW positive) **(b) $\overline{V}_\theta$ (positive upward at outer mid-plane)**

Figure 5. Calculated velocities for carbon and deuterium for counter-injected upper SN shot #138639.

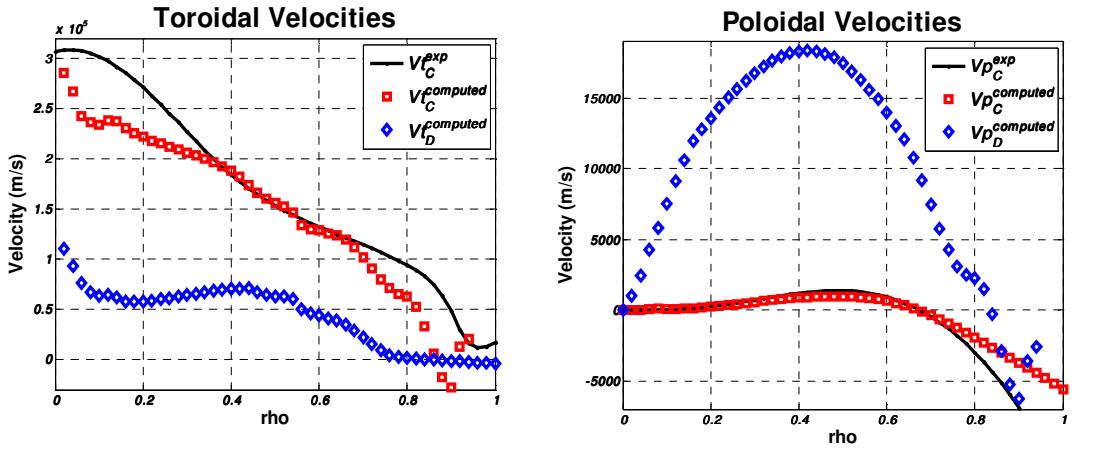

(a) $\overline{V}_\phi$ (CCW positive) **(b) $\overline{V}_\theta$ (positive downward at outer mid-plane)**

Figure 6. Calculated velocities for carbon and deuterium for co-injected lower SN shot #142020.

consistent under-prediction of poloidal velocities for the two shots in this research. Inclusion of the divertor effect and other unrepresented plasma physics in the calculation model are left as future research. The results from the Miller model study, however, is a significant improvement relative to the earlier circular model study [30], in which the

measured carbon toroidal velocities were overpredicted by roughly a factor of 2 and the disagreement in predicted and measured carbon poloidal velocities was even larger.

Figures 7 show the calculated density asymmetries ($n_{i,I}^{c,s}$), which are relatively small (less than 10% everywhere except in the very edge). These asymmetries are larger for carbon than for deuterium. Note that a positive/negative sine component indicates an upward/downward asymmetry in the density distribution, while a positive/negative cosine component indicates an outward/inward asymmetry in the density distribution. The velocity asymmetries ($V_{i,I}^{c,s}$) are coupled with $n_{i,I}^{c,s}$ by Eqs. (39), (40), (44) and (45), thus can be easily computed from these density asymmetries.

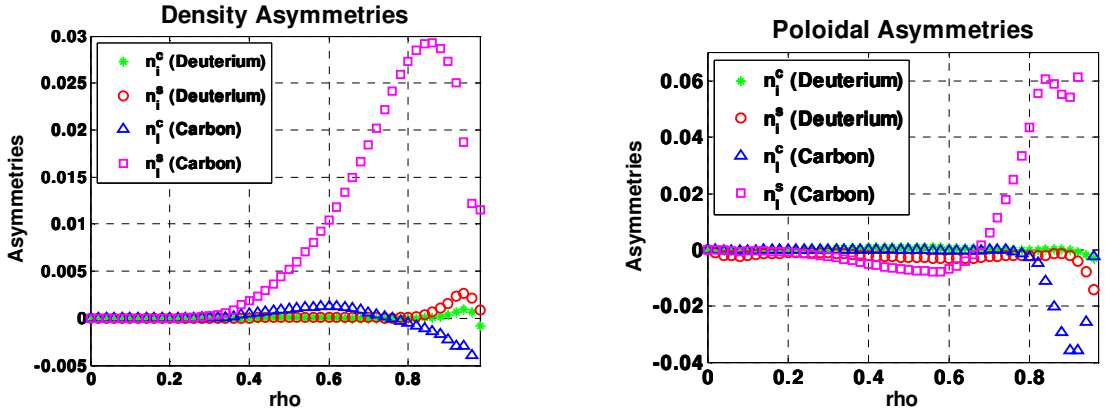

(a) Ctr-injection shot #138639 **(b) Co-injected shot #142020**

Figure 7. Density asymmetries for carbon and deuterium.

5.2 Calculated Momentum Transport Rates

The inertial and gyroviscous toroidal angular momentum transport frequencies are strong functions of poloidal asymmetries as shown in Eq. (31) and (33)-(37). These transport frequencies are calculated with the density asymmetries shown in Figs. 7 and plotted in Figs. 8 and 9 for the range in which neglected edge phenomena are unimportant. Since the gyroviscous transport frequency is generally much larger than the inertial transport frequency and the deuterium density is much larger than the carbon density, the

total toroidal angular momentum transport frequency (neglecting charge-exchange) is essentially the gyroviscous toroidal angular momentum transport frequency of deuterium, i.e., $\nu_j \approx \nu_{dj}$ where ν_j is the total transport rate of species j. Note that this significant neoclassical gyroviscous transport would vanish in a poloidal rotation theory that does not account for density and velocity asymmetries. It is notable that Figs. 8 and 9 imply both inward ($\nu_{nj}, \nu_{dj} < 0$) and outward ($\nu_{nj}, \nu_{dj} > 0$) angular momentum transport for both

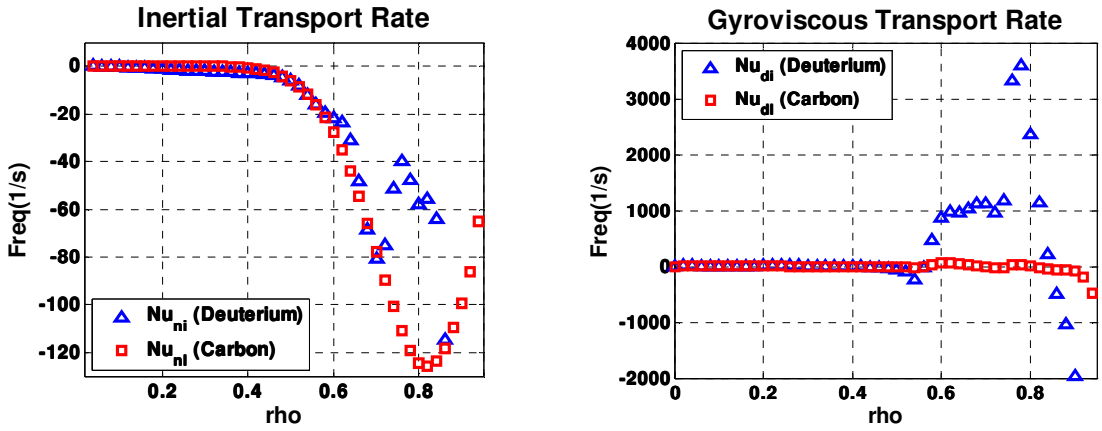

(a) Inertial transport frequency **(b) Gyroviscous transport frequency**

Figure 8. Toroidal angular momentum transport frequencies for counter-injected shot #138639.

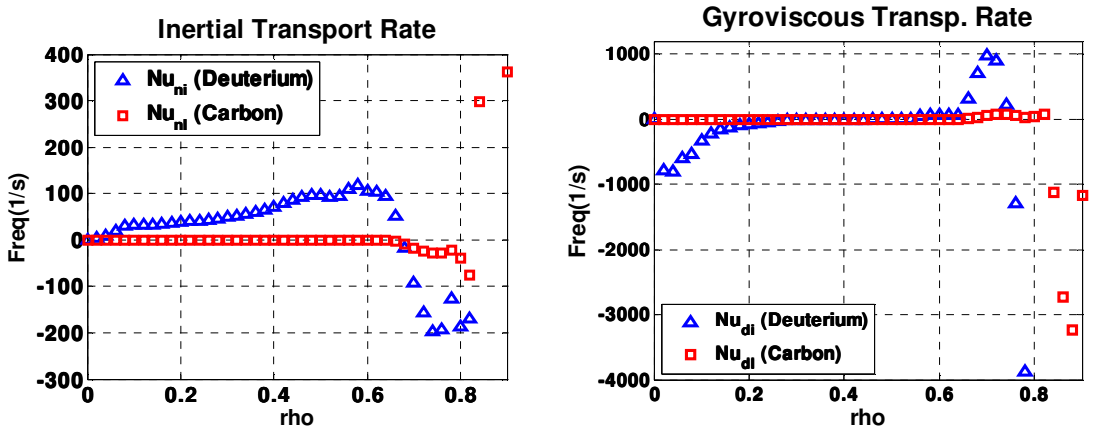

(a) Inertial transport frequency **(b) Gyroviscous transport frequency**

Figure 9. Toroidal angular momentum transport frequencies for co-injected shot #142020.

deuterium and carbon. Although the larger transport frequencies in the plasma edge may be due in part to the $V_{\phi j} \sim V_{thj}$ ordering of the Braginskii formalism and the neglect of charge-exchange, the profiles clearly imply both inward and outward momentum transport.

5.3 Circular vs. Miller Model Results

Since the circular model is just a special case of the Miller geometry (i.e., $\kappa = 1$ and $\delta = 0$ with no Shafranov shift), the same numerical algorithm can be used to calculate the velocities for the circular model extended rotation theory. The predictions of the circular and Miller model theories are compared with the measured carbon velocities in Figs. 10 and 11. The Miller model predictions are in significantly better agreement with experiment than are the circular model predictions, due to the better representation of the poloidal dependences of the flux surfaces, which leads to a more accurate calculation of poloidal asymmetries and poloidal rotation velocities.

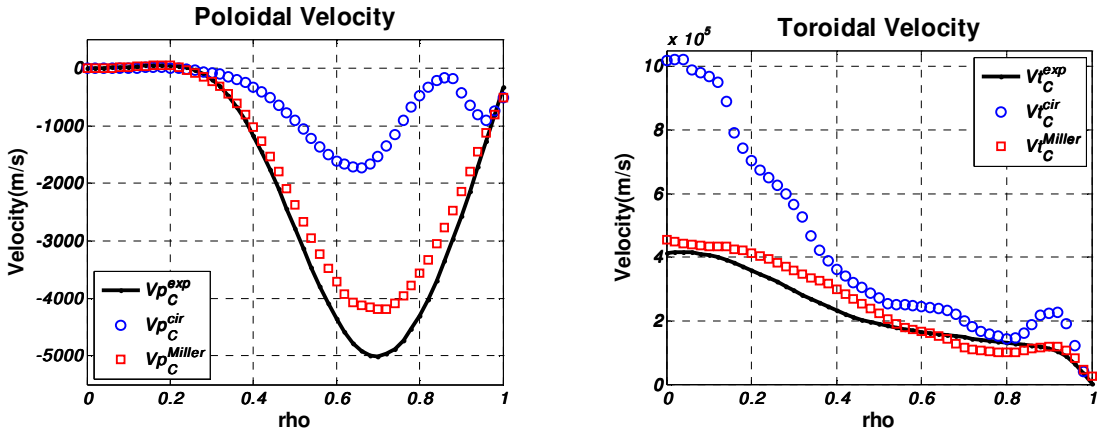

(a) $\overline{V}_\phi$ (CCW positive) **(b) $\overline{V}_\theta$ (positive upward at outer mid-plane)**

Figure 10. Comparison of predicted carbon velocities with the circular and Miller models with measurements for ctr-injected shot #138639.

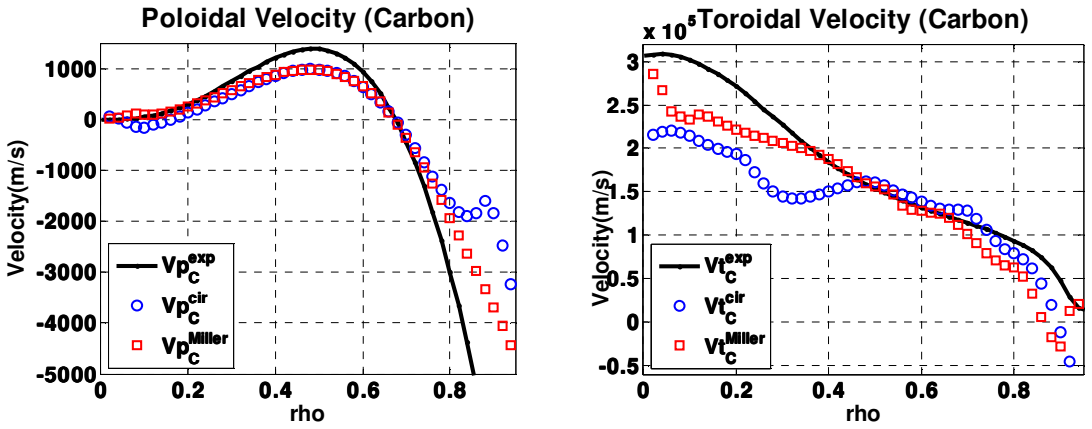

(a) $\overline{V}_{\phi}$ (CCW positive) (b) $\overline{V}_{\theta}$ (positive downward at outer mid-plane)

Figure 11. Comparison of predicted carbon velocities with the circular and Miller models with measurements for co-injected shot #142020.

CHAPTER 6

NUMERICAL ANALYSIS METHODOLOGY

Since the dynamics of nonlinear system of equations involving plasma fluid equation is still an unexplored area of research from chaos theory [53], its numerical solution requires a detailed analysis of the iterative dynamics and apply the minimization (or optimization) approach to identify the true solution from multiple feasible solutions generated by nonlinear iterations. In this research, a combination of nonlinear Successive Over-Relaxation (SOR) [54-56] and Simulated Annealing (SA) [57, 58] provides the most stable and robust algorithm for the given task, which are discussed in detail in this chapter.

6.1 Numerical Calculation Model

The resultant system of eight nonlinear equations from the new extended neoclassical rotation theory can be solved for the toroidal and poloidal velocities and the sin and cos density asymmetries for a two species (deuterium and carbon) plasma, at each radial mesh point from the center of plasma to the edge (we use 51 mesh points). Note that all the unknowns in the calculation model, summarized in Eqs. (53), are normalized so that numerical round-off errors are minimized, and the calculated results presented in Figs. (5)-(7) in the previous chapter are non-normalized values.

$$\begin{aligned}
&\hat{V}_{\phi i} = \hat{V}_{\phi D} = \hat{V}_{tD} : \text{Toroidal Velocity (Deuterium)}, && \hat{V}_{\phi I} = \hat{V}_{\phi C} = \hat{V}_{tC} : \text{Toroidal Velocity (Carbon)} \\
&\hat{V}_{\theta i} = \hat{V}_{\theta D} = \hat{V}_{pD} : \text{Poloidal Velocity (Deuterium)}, && \hat{V}_{\theta I} = \hat{V}_{\theta C} = \hat{V}_{pC} : \text{Poloidal Velocity (Carbon)} \\
&\tilde{n}^{c}_{D} = \tilde{n}^{c}_{i} : \text{Cos Asymmetry (Deuterium)}, && \tilde{n}^{c}_{C} = \tilde{n}^{c}_{I} : \text{Cos Asymmetry (Carbon)} \\
&\tilde{n}^{s}_{D} = \tilde{n}^{s}_{i} : \text{Sin Asymmetry (Deuterium)}, && \tilde{n}^{s}_{C} = \tilde{n}^{s}_{I} : \text{Sin Asymmetry (Carbon)}
\end{aligned} \tag{53}$$

A numerical algorithm is designed to solve the nonlinearly coupled set of eight equations iteratively, using the decomposition of the entire system based on physical grounds into three subsystems given in Eqs. (54a)-(54c), written in generic forms.

Poloidal rotation subsystem: $$\begin{bmatrix} c_{11} & c_{12} \\ c_{21} & c_{22} \end{bmatrix} \begin{bmatrix} \hat{V}_{\theta i} \\ \hat{V}_{\theta I} \end{bmatrix} = \begin{bmatrix} d_1 \\ d_2 \end{bmatrix} \tag{54a}$$

Density asymmetry subsystem: $$\begin{bmatrix} a_{11} & a_{12} & a_{13} & 0 \\ a_{21} & a_{22} & 0 & a_{24} \\ a_{31} & 0 & a_{33} & a_{34} \\ 0 & a_{42} & a_{43} & a_{44} \end{bmatrix} \begin{bmatrix} \tilde{n}_i^c \\ \tilde{n}_i^s \\ \tilde{n}_I^c \\ \tilde{n}_I^s \end{bmatrix} = \begin{bmatrix} b_1 \\ b_2 \\ b_3 \\ b_4 \end{bmatrix} \tag{54b}$$

Toroidal rotation subsystem: $$\begin{bmatrix} e_{11} & e_{12} \\ e_{21} & e_{22} \end{bmatrix} \begin{bmatrix} \hat{V}_{\phi i} \\ \hat{V}_{\phi I} \end{bmatrix} = \begin{bmatrix} f_1 \\ f_2 \end{bmatrix} \tag{54c}$$

where all the coefficients can be found in Appendix D. This decomposition proved to be better-conditioned and iteratively more stable than the entire set of eight-by-eight nonlinear system taken as a single set by allowing isolation of ill-conditioning to (54c) only after reformulating (54a) and (54b) to eliminate singularities in them. The numerical algorithm for this Miller model study is developed independently from the earlier circular model calculation algorithm [30] but shares very similar numerical characteristics. More detailed description of the Miller model numerical algorithm is given in the following sections.

In earlier studies with the circular model [30, 59], Shafranov shift was not considered for simplicity but is represented in this study with the following form of analytic Shafranov shift model [34],

$$\partial R_0 \big/ \partial r \equiv \Delta' = - r \big/ R_0 \left(\beta_\theta + 1 \big/ 2 \, \ell_i \right) \tag{55}$$

where $\beta_\theta = nT \big/ \left(B_\theta^2 \big/ 2\mu_0 \right)$ and ℓ_i is the internal inductance. Studies with more accurate Shafranov shift models can be done when these are considered to be critical for accuracy.

Now with the given decomposed numerical computation model, Eqs. (54a)-(54c), there still remain two major numerical challenges. First is the instability of the nonlinear iteration dynamics and second is the identification of the true solution from the several feasible solutions generated by nonlinear iterations. In short, the former was successfully

controlled with nonlinear SOR [54-56] and the latter accomplished by SA [57, 58]. Before discussing the details of these methods, it is necessary to briefly discuss the differences in linear and nonlinear programming to understand the rationale for the methods used in this extended neoclassical rotation calculation.

6.2 Linear and Nonlinear Programming

Linear programming [54, 60, 61] is the study of maximizing or minimizing linear functions subject to linear equality and inequality constraints. Since linear functions are both convex and concave, any local minimum or maximum must be a global optimum. Thus, excepting numerical issues, there is no issue with convergence to the "wrong" solution. Thus, literatures [54, 55, 61, 62] on linear programming discusses how fast it can converge, and as long as storage is not a concern faster convergence is always preferred.

For simple and standard nonlinear problems [54, 55, 61, 62], it is also possible to converge to a single solution using standard numerical methods such as Newton's method and its variants. In the nonlinear non-convex case [53, 56, 63], which includes many practical physics problems, the situation changes quite significantly. The higher the nonlinearity is, the higher the chance of failing to converge to the physical solution. In this case the iteration will often try to converge towards the true (physical) solution but then be eventually disturbed by numerical noises, then drive towards other solutions [53, 56]. Keeping track of these various approximate solutions as the algorithm progresses, the algorithm generates several feasible solutions [53, 62, 63], corresponding to local minima in nonlinear topological maps, but only one of them corresponds to the true physical solution. Then, a technique becomes necessary to identify the true solution from the nonlinear topological maps [58, 63]. Considering that most minimization techniques [55, 62] tend to converge to the nearest local minimum from initial guesses, application

of the global minimum search concepts from SA [57, 58] greatly reduces the risk of identifying a wrong solution as the true solution and allows search for a global minimum within physically feasible range.

Another issue is the importance of the accuracy of initial guesses for any iterative programming [53-55, 62]. When the initial guesses are too far from the true solution, even simple linear and nonlinear problems can continue diverging the iterations far from the true solution, increasing the risk of identifying a wrong solution as the true solution even if it converges [54, 55, 62]. With nonlinear physics problems, the accuracy of initial guesses become increasingly important because minimization algorithm will eventually search for the solution near the initial guesses [54, 55], but SA gives the algorithm greater flexibility by allowing it to test all the feasible solutions within the feasible range [57, 58]. For the extended rotation calculation in this research [64], the initial guesses for the velocities are believed to be very accurate because the initial $\hat{V}_{\theta I}$ and $\hat{V}_{\phi I}$ for the carbon impurity comes directly from experimental measurement, and the initial deuterium $\hat{V}_{\phi i}$ is inferred from perturbation theory [59] with $\hat{V}_{\phi I}$ as an input, and the initial deuterium $\hat{V}_{\theta i}$ is calculated with other initial guesses based on the momentum balance equation. The initial guesses for $\tilde{n}_j^{c.s}$, however, can be neither measured nor inferred, thus zeros are used.

In terms of the dynamics of the numerical system, nonlinear algorithms are vulnerable to instability (i.e., highly sensitive to numerical errors) [53, 56]. Since all nonlinear problems must be solved iteratively, there are several factors that affect the dynamics of the iterations such as conditioning of the system, degree of nonlinearity, characteristics of the chosen numerical method, accuracy of the initial guesses, etc. Instability of the system dynamics was surely an issue for the extended neoclassical

rotation calculation, especially with the ill-conditioned toroidal rotation subsystem in Eq. (54c). Fortunately, under-relaxation worked very effectively, making nonlinear SOR with optimal relaxation weight the key to the stable iterative dynamics of the given problem [64]. This dependence of the dynamic stability on many factors also means that the final solutions may also slightly vary within a stable range depending on the chosen algorithm, relaxation scheme, etc. [53, 65].

6.3 Nonlinear SOR Method and Instability Control

Figure 12 is a flowsheet for the nonlinear SOR algorithm for the extended neoclassical rotation calculation model. Since the initial guesses for $\tilde{n}_j^{c,s}$ are zeros, these are allowed to be updated whenever new $\hat{V}_{\phi,\theta}$ values are available. Testing the algorithm with final calculated asymmetries as new initial guesses appears to help stabilize iteration dynamics of the system, but is left for future investigation as a longer run-time and

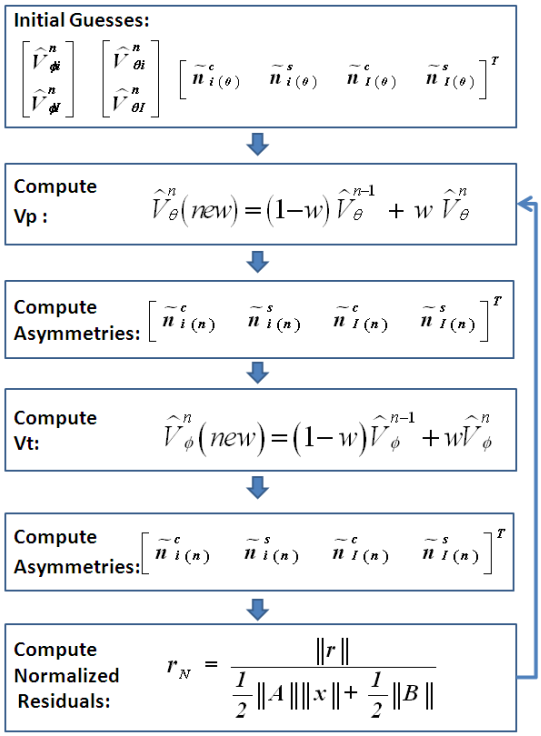

Figure 12. SOR flowsheet.

manual input of new asymmetries are not desirable for a user-friendly code.

Theoretically, there exists an optimal relaxation weight when solving a minimization problem with iterative SOR [54, 55, 62]. The extended rotation calculation model in this research [64] adaptively determines the relaxation weights (w) based on the conditioning of the subsystems at initial iteration ($n=1$) by

$$w = \frac{\alpha}{cond\left(A\right)^{n=1}} \quad . \tag{56}$$

Here α is a constant fixed for all 51 meshes, usually $0.2 \le \alpha \le 2$, and $cond\left(A\right)^{n=1}$ is the condition number of each mesh in Eqs. (54a) and (54c) at the initial step, usually $3 < cond\left(A\right) < 100$ except for the near singularity meshes (i.e., meshes with high condition numbers in Fig. 13). Fig. 13 shows the extreme ill-conditioning of the toroidal rotation subsystem near $\rho = 0.25$, $\rho = 0.67$, $\rho = 0.84$, and in the plasma edge, which are introduced by one of the coefficients (e_{11}) in Eq. (54c) crossing zero axis at the corresponding meshes.

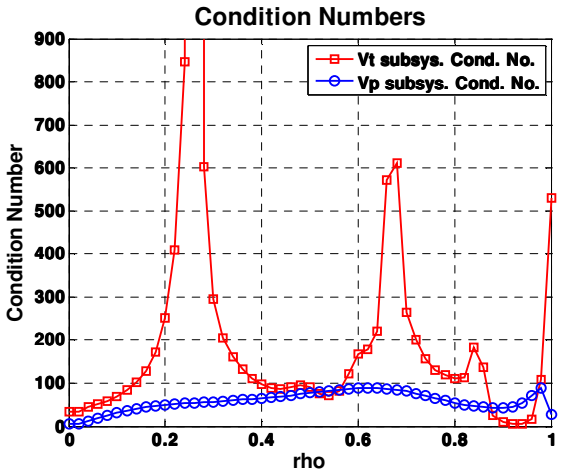

Figure 13. Condition numbers at initial iteration step.

In dealing with the unstable iterative dynamics of this ill-conditioned system, the adaptive weight scheme in Eq. (56) serves two purposes: i) the relaxation weight is

smaller when the conditioning is worse at a near singular mesh, giving all the meshes the same order of deviation magnitude while iterations continue; and ii) it prevents a premature termination of the algorithm when a calculated value at a singular mesh reaches OFL (OverFlow Level) due to high numerical sensitivity. Premature termination needs to be avoided so that the algorithm can generate topological maps with enough feasible solutions (at least three, empirically) for SA to test them for the true solution. Thus, for the rotation subsystems in Eqs. (54a) and (54c), the new output velocities at n^{th} iteration is calculated by

$$\hat{V}^{n}\left(new\right) = \left(1-w\right)\hat{V}^{n-1} \;+\; w\,\hat{V}^{n} \,. \tag{57}$$

6.4 Nonlinear Topological Maps and Simulated Annealing

Nonlinear topological maps can be generated with many iterative parameters but most commonly by "relative" residuals (or errors) computed with either $\|r_n\|/\|r_1\|$ or $\|r_n\|/\|r_{n-1}\|$ where r_n is the residual at n^{th} iteration, r_{n-1} is at the previous step iteration, and r_1 is at the initial iteration [54-56]. Application of these popular relative residuals yields noisy topological maps probably because the coefficients on both sides of each subsystem constantly change its relative magnitudes, especially with the initial guesses of $\tilde{n}_j^{c,s}$ being zeros. To measure the error magnitude relative to the size of constantly-changing subsystems, a new concept called "normalized" residual (r_N) at the n^{th} iteration step given by

$$r_N{}^{n} \equiv \frac{\left\|r^n\right\|}{\frac{1}{2}\left\|A^n\right\|\left\|x^n\right\| + \frac{1}{2}\left\|b^n\right\|} \tag{58}$$

is devised for a general n^{th} iteration system $A^n x^n = b^n$ where $r^n = b^n - A^n x^n$ is its residual. This normalized residual allows a heuristic measure of the residual size relative

to the magnitude of each iteration system. For example, $r_N = 10^{-3}$ indicates that the residual is approximately one thousandth when the entire system magnitude is normalized to one. Since r_N is calculated for both poloidal and toroidal subsystems, topological maps for the entire system dynamics are given by the 2-norms of both normalized residuals of Eqs. (54a) and (54c) as shown in Fig. 14 and 15.

With topological maps provided, a simple local minima searching algorithm can assist SA to identify a global minimum within the feasible range, eliminating the need of applying a complete implementation of SA [57]. From the empirical testing of the nonlinear dynamics of the given problem in this research, there are two important considerations when applying SA. First, it is practically efficient to set a physically feasible range and locate a "locally" global minimum within that range. This is also a good practice when we know that the initial guesses are quite close to the true solution as is the case with the given problem. Second, understanding that nonlinear algorithms with high numerical sensitivity tend to eventually drive the iterations to trivial solutions [56, 65], all feasible solutions need to be tested for trivial solutions because these are usually identified with much smaller normalized residuals than those of the true solution. In the plasma rotation calculation with strong beam injection, any solution(s) with zero velocity (or velocities) can be considered trivial solution(s). Therefore, use of SA within local (not global) feasible range and elimination of trivial solutions based on physics argument is empirically proven to be the best minimization method for the extended neoclassical rotation calculations [64].

6.5 Nonlinear Dynamics of the Extended Neoclassical Rotation Model

Using the numerical methodology discussed in the previous sections, the extended neoclassical rotation calculation algorithm was applied to two DIII-D discharges given in Chapter 4 and the followings summarize the observed characteristics of the nonlinear iterative dynamics of the given problem [64]. First, the iteration has

strong tendency to drive towards trivial solutions especially with larger w values (i.e., larger α). This means that with w too large it is possible for the true solution to turn into a saddle point, thus not be presented as one of the feasible solutions. With w too small, the algorithm generates too many feasible solutions, all of which except one are transient solutions. Thus, examining the solutions with a wide range of α values in Eq. (56) is a simple and robust way to identify the optimal α value explained theoretically [54, 55, 62]. The possibility of theoretically identifying an optimal α value without such a rigorous empirical search will be investigated for future algorithms.

Secondly, certain relaxation weights, supposedly very close to the optimal α, allow the system to stagnate near the true solution. With optimal α value, it appears that the algorithm tries to converge to a stagnant solution, increasing the confidence when it agrees with the true solution selected by SA, which is the case for two shots in this study [64]. Lastly, the true solutions are usually identified with r_N^n below 10^{-3} before getting disturbed again by numerical noises. Analysis on more shots are required to generalize this finding but with the trivial solutions usually yielding r_N^n lower by more than an order of magnitude (below 10^{-4}) it can be used as a criteria to test any local minimum for the true solution in future algorithms.

6.6 Application of Simulated Annealing

Out of two shots analyzed in this research, shot #138639 contains a good mix of the characteristics discussed in the previous section with more stable dynamics, thus we focus our discussion on this shot. Figures 14 and 15 present topological maps for four selected mesh points for this shot with $\alpha = 0.5$. The first three local minima in these maps correspond to the three feasible solutions (non-normalized velocities) in Figs. 16.

There are subtle differences between the topological maps in Figs. 15 and 16 because the iterative dynamics are different from the mesh points on the left and right

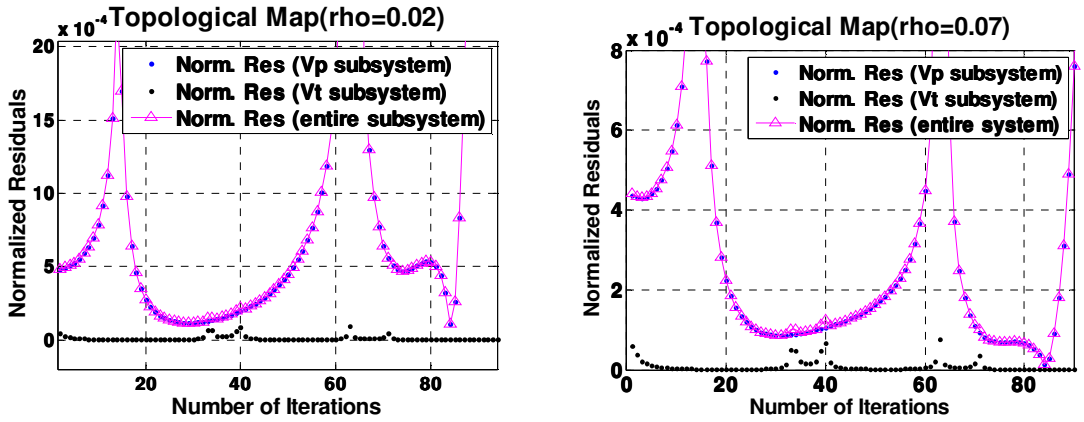

Figure 14. Topological maps for the meshes for $\rho < 0.25$ ($\alpha = 0.5$).

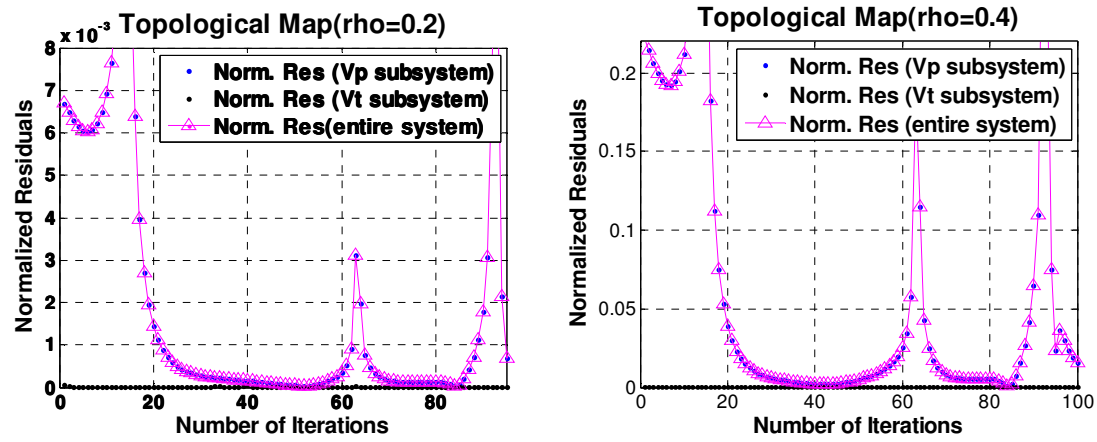

Figure 15. Topological maps for the meshes for $\rho > 0.25$ ($\alpha = 0.5$).

side of $\rho = 0.25$. The iterative dynamics of the mesh points in $0.25 < \rho < 1$ range, with their sample topological maps in Figs. 15, are more stable because the 2nd and 3rd solutions sets in Figs. 16 for the well-conditioned mesh points stay quite closer to each other (i.e., stagnate at these solutions) for about up to 40 iterations except the deuterium polidal velocity in Fig. 16(b), possibly indicating that the algorithm may converge the iterations to these solutions unless disturbed by numerical noises. With all three solutions being possible candidates for the true solution in this range, SA identifies the 2nd solution set with the lowest r_N^n as the true solutions. On the other hand, the mesh points on the left side of $\rho = 0.25$ in Figs. 16, with their sample topoligical maps in Figs. 14, are

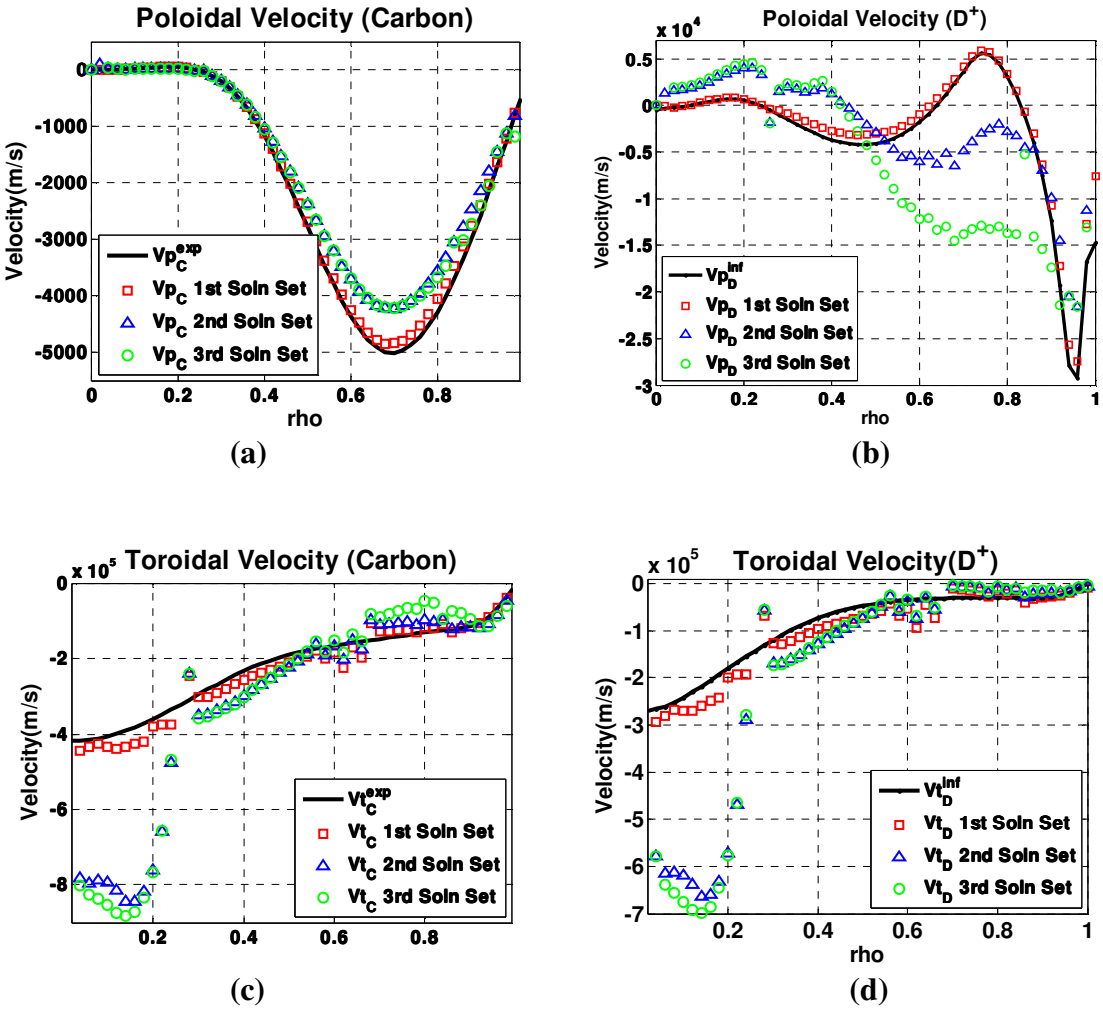

Figure 16. Feasible solution sets for local minima in Figs. 14 and 15 (toroidal velocities: CW positive / poloidal velocities: positive upward at outer mid-plane).

driven towards the trivial solutions much faster because according to Eq. (56) this region has much higher w values. $V_{\theta I}$ values in this range quickly drive to zeros and introduce numerical errors in other velocities causing them to jump to much higher values, which is a typically observed response of the system at trivial solutions. Therefore, in this range the first solution set with r_N^n well below 10^{-3} corresponds to the true physical solution and it can be verified with lower α values to yield the same type of iterative dynamics as in $0.25 < \rho < 1$ range.

In Figures 16(c) and 16(d), it can be observed that the mesh points with near singularity are highly sensitive to numerical round-off errors. The present algorithm simply neglects these near singular meshes from the output and spline-connects the entire radial profile based on the physics argument that such discontinuities cannot physically exist in tokamak plasmas. Thus, the final non-normalized processed velocity profiles for this shot #138639 are presented in Figs. 5 with the direction of the toroidal velocities reversed as positive counter-clockwise (CCW) to indicate in the direction of the neutral beam injection. The final non-normalized density asymmetries ($n_j^{c,s}$), which are the additional variables that made this extended neoclassical rotation model highly nonlinear, is presented in Fig. 7(a). More details on how to run the code and process these final solutions can be found in the user's manual provided in Appendix E.

6.7 Verification of the Algorithm and of the Results

Since the calculation results from the extended neoclassical rotation algorithm [64] cannot be verified against known solutions, checking the existence of true solutions for a wider range of α values seems to be the most robust way of numerically verifying the final solutions. Refer to the user's manual in Appendix E for the details on this numerical verification. Another rigorous verification was done during the code development phase by turning off some variables (i.e., fixed them at initial guesses) selectively with different combinations of variables to check the solutions against known characteristics of simpler plasma rotation models [30, 38-40]. In the simplest case, with the asymmetries and toroidal velocities fixed at their initial guesses, the algorithm was checked to generate the same solutions as in solving a simple linear poloidal rotation subsystem in Eq. (54a). Then, turning on the toroidal velocity subsystem in Eq. (54c) allows nonlinear calculation of the velocities with no asymmetries ($\tilde{n}_j^{c,s} = 0$), which we would predict to be less accurate poloidal velocities that eventually translate into the

over-prediction of toroidal velocities [51]. Finally, turning on the asymmetry iterations of Eq. (54b), we can observe the evolution of the true physical solutions to our final solutions in Fig. 5.

CHAPTER 7

FUTURE RESEARCH

7.1 Future Extensions of Neoclassical Rotation Theory

The Extended Neoclassical Rotation theory in this research is based on Braginskii's strong rotation ordering, $V_{\phi j} \simeq V_{thj}$, does not explicitly represent the divertor, and does not include neutral recycling and the associated atomic physics in the edge. Representation of the divertor x-point may require either a geometric treatment of the Miller flux surfaces or additional terms that account for the complicated atomic physics in the divertor region, thus needs more investigation in the future. It is straightforward to extend the continuity equation to include all the atomic physics effects and to include a neutral recycling calculation, as was done in one of the previous circular model studies [59]. Extension of the Miller flux surface geometry model to explicitly represent the divertor should be possible but such extensions will still be limited to the strong rotation ordering. Developing a new theory based on Mikhailovskii's weak rotation ordering, $V_{\phi j} \ll V_{thj}$, would extend the applicability of the current rotation theory based on the S-S model to a wider range of weaker plasma rotation as might be found in future burning plasmas. Thus, in summary the next theoretical research directions for the extended neoclassical rotation theory [64] are the extension of the current theory to include i) the divertor X-point dependence of the magnetic flux surfaces, ii) Mikhailovskii's weak rotation ordering viscosity tensor [16, 26-28, 66], and iii) the charge-exchange of recycling neutrals, all of which would increase the accuracy in the plasma edge and extend applicability to plasmas with weak rotation.

Mikhailovskii's viscosity formulism [16] has been revised by other researchers and most recently by Catto and Simakov [26, 27] and Ramos [28]. A simple way of presenting Catto and Simakov's viscosity formalism to show its relation to Braginskii's is

$$\overleftrightarrow{\mathbf{\Pi}}_j^{\,Mikhailovskii} = \overleftrightarrow{\mathbf{\Pi}}_j^{\,Braginskii} + \overleftrightarrow{\mathbf{\Pi}}_j^{\,Heat} . \tag{59}$$

This shows that we can extend the current rotation theory by adding $\overleftrightarrow{\mathbf{\Pi}}_j^{\,Heat}$ to the formalism, thus making the current theory a special case of the more general theory based on Mikhailovskii's ordering. In doing so, selectively adding some important terms with significant contribution from the heat equation terms may simplify the modification of the current theory. In this regard, use of Braginskii's formalism in this research can be considered as an intermediate step toward developing a more general extended neoclassical rotation theory for both strong and weak rotation orderings.

7.2 Future Improvement of Numerical Analysis Methodology

Along with theoretical advances, improvement in numerical analysis methodology in future research is as important because the nonlinear dynamics of future computational models would be very similar to the ones presented in this research. To improve the current algorithm in future studies, there are some possible candidate approaches in addition to the minor upgrades suggested in earlier sections. First, realizing that practical physics problems can be formulated into numerical calculation models in a variety of ways, examination of other decompositions of the subsystems in Eqs. (54a)-(54c) to eliminate singularities and improve conditioning should be investigated. Another aggressive restructuring of the problem by identifying new additional relations to set up the entire problem as a least squares problem has gone through some initial investigation, showing improvements with conditioning of the toroidal rotation subsystem, but this approach requires significant further investigation. Another future effort would be in extending the capability of the current algorithm to

handle problems with a diverse combination of inputs because tokamak experiments and diagnostics are focused on different discharge parameters with different accuracy level. To analyze shots with substantially different parameters, the current numerical algorithm presented in this research may need to be modified. Lastly, because of the uncertainties associated with experimental data and the inputs to the algorithm, efforts to identify the sources of such uncertainties and to design an algorithm with minimized sensitivity to these uncertainties will continue during the development of future GTROTA versions. For this purpose, investigation on diagnostic limitations and the sensitivity of the results to these experimental uncertainties will be necessary in future studies to design and apply numerical schemes more resilient to such uncertainties. Therefore, along with a future theoretical research on the extended neoclassical rotation, efforts on the improvement of the corresponding numerical model and methodology should continue as well.

CHAPTER 8

CONCLUSIONS

The extended neoclassical rotation and momentum plasma transport theory based on the Stacey-Sigmar model with the more accurate Miller equilibrium flux surface geometry was presented in this research. It was also shown that the gyroviscous contribution to viscous transport, $\left(R^2\nabla\phi\cdot\nabla\cdot\vec{\mathbf{\Pi}}\right)_{gv}$, accounts for the most of neoclassical toroidal angular momentum damping in this model. Comparisons of the predictions of this new theory with experiment for two DIII-D discharges indicate that the new theory predicts the measured carbon poloidal and toroidal rotation very well (<10%) everywhere except in the very edge for the co-injected shot, where the neglect of recycling neutrals and of the divertor and the assumption of strong rotation ordering may be expected to cause difficulty. It is shown that the more accurate poloidal representation of the flux surfaces provided by the Miller equilibrium model is responsible for a significantly more accurate prediction than is possible with the similar extended neoclassical rotation theory based on the circular model [30].

The good agreement of prediction with experiment found on the two shots examined in this research leads us to tentatively conclude that the extended neoclassical rotation theory, when all important terms are retained and properly evaluated, is capable of accounting for most of the rotation and momentum transport in tokamaks. With the accuracy in the prediction of carbon velocities calculated in this study, we can also conclude that the gyroviscous transport rates calculated with poloidal asymmetries in the formalism are at least in the correct order of magnitude and are actually much greater than the perpendicular viscous transport. This also implies that the amount of anomalous transport may be smaller than we currently try to explain with turbulent transport theory

due to this significant neoclassical transport contribution from gyroviscous effect. These conclusions must, of course, be confirmed by more extensive comparisons of prediction with experiment. Also, improved accuracy in the plasma edge requires extending the model further to represent charge-exchange of recycling neutrals, the effect of the divertor on poloidal asymmetries, and the weak rotation ordering of Mikhailovskii. All these theoretical advances in future research will also be supported with the corresponding improvement in the numerical analysis methodology.

APPENDIX A

INERTIAL AND VISCOSITY TERMS IN CURVILINEAR GEOMETRY

A1. Inertial terms in curvilinear geometry:

$$\left[\left(\vec{V}\bullet\nabla\right)\vec{V}\right]_r = \frac{V_{rj}}{h_r}\frac{\partial V_{rj}}{\partial r} + \left[\frac{V_{\theta j}}{h_\theta}\frac{\partial V_{rj}}{\partial \theta} + \frac{V_{rj}V_{\theta j}}{h_r h_\theta}\left(\frac{\partial h_r}{\partial \theta} - \frac{\partial h_\theta}{\partial r}\right)\right] - \frac{V_{rj}V_{\phi j}}{h_r h_\phi}\frac{\partial h_\phi}{\partial r} \tag{A1}$$

$$\left[\left(\vec{V}\bullet\nabla\right)\vec{V}\right]_\theta = \left[\frac{V_{rj}}{h_r}\frac{\partial V_{\theta j}}{\partial r} + \frac{V_{\theta j}V_{rj}}{h_\theta h_r}\left(\frac{\partial h_\theta}{\partial r} - \frac{\partial h_r}{\partial \theta}\right)\right] + \frac{V_{\theta j}}{h_\theta}\frac{\partial V_{\theta j}}{\partial \theta} - \frac{V_{\theta j}V_{\phi j}}{h_\theta h_\phi}\frac{\partial h_\phi}{\partial \theta} \tag{A2}$$

$$\left[\left(\vec{V}\bullet\nabla\right)\vec{V}\right]_\phi = \left(\frac{V_{rj}}{h_r}\frac{\partial V_{\phi j}}{\partial r} + \frac{V_{\phi j}V_{rj}}{h_\phi h_r}\frac{\partial h_\phi}{\partial r}\right) + \left(\frac{V_{\theta j}}{h_\theta}\frac{\partial V_{\phi j}}{\partial \theta} + \frac{V_{\phi j}V_{\theta j}}{h_\phi h_\theta}\frac{\partial h_\phi}{\partial \theta}\right) \tag{A3}$$

A2. Viscosity terms in curvilinear geometry:

The rate-of-stress tensor elements in the viscous stress tensor is decomposed into

$$\Pi_{\alpha\beta} = \Pi^0_{\alpha\beta} + \Pi^{12}_{\alpha\beta} + \Pi^{34}_{\alpha\beta} \tag{A4}$$

where

$$\Pi^0_{\alpha\beta} = -\eta_0 W^0_{\alpha\beta},\ \Pi^{12}_{\alpha\beta} = -\left(\eta_1 W^1_{\alpha\beta} + \eta_2 W^2_{\alpha\beta}\right), \text{ and } \Pi^{34}_{\alpha\beta} = \eta_3 W^3_{\alpha\beta} + \eta_4 W^4_{\alpha\beta}. \tag{A5}$$

The elements of the traceless rate-of-strain tensor are

$$\begin{aligned}
W^0_{\alpha\beta} &\equiv \frac{3}{2}\left(f_\alpha f_\beta - \frac{1}{3}\delta_{\alpha\beta}\right)\left(f_\mu f_\nu - \frac{1}{3}\delta_{\mu\nu}\right)W_{\mu\nu},\\
W^1_{\alpha\beta} &\equiv \left(\delta^\perp_{\alpha\mu}\delta^\perp_{\beta\nu} + \frac{1}{2}\delta^\perp_{\alpha\beta}f_\mu f_\nu\right)W_{\mu\nu},\\
W^2_{\alpha\beta} &\equiv \left(\delta^\perp_{\alpha\mu}f_\beta f_\nu + \delta^\perp_{\beta\nu}f_\alpha f_\mu\right)W_{\mu\nu},\\
W^3_{\alpha\beta} &\equiv \frac{1}{2}\left(\delta^\perp_{\alpha\mu}\varepsilon_{\beta\gamma\nu} + \delta^\perp_{\beta\nu}\varepsilon_{\alpha\gamma\mu}\right)f_\gamma W_{\mu\nu},\\
W^4_{\alpha\beta} &\equiv \frac{1}{2}\left(f_\alpha f_\mu\varepsilon_{\beta\gamma\nu} + f_\beta f_\nu\varepsilon_{\alpha\gamma\mu}\right)f_\gamma W_{\mu\nu},
\end{aligned} \tag{A6}$$

where $\delta_{\alpha\beta}^{\perp} \equiv \delta_{\alpha\beta} - f_\alpha f_\beta$, $\delta_{\alpha\beta}$ the Kronecker delta function, and $\varepsilon_{\alpha\beta\gamma}$ the antisymmetric unit tensor. The Einstein summation convention is also assumed. For tokamak plasmas, we can assume

$$f_r = |B_r|/|B| \approx 0,\ f_\theta = |B_\theta|/|B| \approx 0,\ f_\phi = |B_\phi|/|B| \approx 1. \tag{A7}$$

Neglecting V_r since $V_r \ll V_\theta < V_\phi$, assuming axisymmetry ($\partial/\partial\phi \approx 0$), and with A_0 defined as

$$\begin{aligned} A_0 &= -\frac{1}{3}\left(W_{rr} + W_{\theta\theta}\right) + \frac{2}{3}W_{\phi\phi} + 2f_\theta W_{\theta\phi} \\ &= 2\left[-\frac{1}{3h_\theta}\frac{\partial V_{\theta j}}{\partial\theta} + \left(\frac{1}{Rh_\theta}\frac{\partial R}{\partial\theta} + \frac{1}{3B_\theta h_\theta}\frac{\partial B_\theta}{\partial\theta} \right) V_{\theta j} + f_p R \frac{1}{h_\theta}\frac{\partial\left(V_{\phi j}R^{-1}\right)}{\partial\theta} \right], \end{aligned} \tag{A8}$$

all the elements of the viscous stress tensors are given by

$$\begin{aligned} \Pi_{rr} = \frac{1}{2}\eta_0 A_0 &+ \eta_1\left[\left(RB_\theta\right)^{-1}\frac{1}{h_\theta}\frac{\partial\left(RB_\theta V_{\theta j}\right)}{\partial\theta} - f_p\frac{R}{h_\theta}\frac{\partial\left(V_{\phi j}R^{-1}\right)}{\partial\theta} \right], \\ &-\eta_3\left[\frac{h_\theta}{h_r}\frac{\partial\left(V_{\theta j}h_\theta^{-1}\right)}{\partial r} - f_p\frac{R}{h_r}\frac{\partial\left(V_{\phi j}R^{-1}\right)}{\partial r} \right] \end{aligned} \tag{A9}$$

$$\begin{aligned} \Pi_{r\theta} = \Pi_{\theta r} = &-\eta_1\frac{h_\theta}{h_r}\frac{\partial\left(V_{\theta j}h_\theta^{-1}\right)}{\partial r} - \left(\eta_2 - \eta_1\right) f_p\frac{R}{h_r}\frac{\partial\left(V_{\phi j}R^{-1}\right)}{\partial r} \\ &-\eta_3\left(RB_\theta\right)^{-1}\frac{1}{h_\theta}\frac{\partial\left(RB_\theta V_{\theta j}\right)}{\partial\theta} - \left(\eta_4 - \eta_3\right) f_p\frac{R}{h_\theta}\frac{\partial\left(V_{\phi j}R^{-1}\right)}{\partial\theta}, \end{aligned} \tag{A10}$$

$$\Pi_{r\phi} = \Pi_{\phi r} = -\eta_2 R\frac{1}{h_r}\frac{\partial\left(V_{\phi j}R^{-1}\right)}{\partial r} - \eta_4 R\frac{1}{h_\theta}\frac{\partial\left(V_{\phi j}R^{-1}\right)}{\partial\theta}, \tag{A11}$$

$$\begin{aligned} \Pi_{\theta\theta} = \frac{1}{2}\eta_0 A_0 &+ \eta_3\frac{h_\theta}{h_r}\frac{\partial\left(V_{\theta j}h_\theta^{-1}\right)}{\partial r} + \left(2\eta_4 - \eta_3\right) f_p\frac{R}{h_r}\frac{\partial\left(V_{\phi j}R^{-1}\right)}{\partial r}, \\ &-\eta_1\left(RB_\theta\right)^{-1}\frac{1}{h_\theta}\frac{\partial\left(RB_\theta V_{\theta j}\right)}{\partial\theta} + \left(\eta_1 - 2\eta_2\right) f_p\frac{R}{h_\theta}\frac{\partial\left(V_{\phi j}R^{-1}\right)}{\partial\theta} \end{aligned} \tag{A12}$$

$$\Pi_{\theta\phi} = \Pi_{\phi\theta} = -\frac{3}{2}\eta_0 f_p A_0 - \eta_2 R\frac{1}{h_\theta}\frac{\partial\left(V_{\phi j}R^{-1}\right)}{\partial\theta} + \eta_4 R\frac{1}{h_r}\frac{\partial\left(V_{\phi j}R^{-1}\right)}{\partial r}, \tag{A13}$$

$$\Pi_{\phi\phi} = -\eta_0 A_0 + 2\eta_2 f_p \frac{R}{h_\theta}\frac{\partial\left(V_{\phi j}R^{-1}\right)}{\partial\theta} - 2\eta_4 f_p \frac{R}{h_r}\frac{\partial\left(V_{\phi j}R^{-1}\right)}{\partial r}. \tag{A14}$$

With these, the viscous force terms in general curvilinear geometry are given by

$$\left(\nabla\bullet\vec{\vec{\Pi}}\right)_\phi = \left[\frac{1}{Rh_\theta h_r}\frac{\partial}{\partial r}\left(Rh_\theta\Pi_{r\phi}\right) + \frac{1}{Rh_r}\frac{\partial R}{\partial r}\Pi_{r\phi}\right] + \left[\frac{B_\theta}{h_\theta}\frac{\partial}{\partial\theta}\left(\frac{\Pi_{\theta\phi}}{B_\theta}\right) + \frac{1}{Rh_\theta}\frac{\partial R}{\partial\theta}\Pi_{\theta\phi}\right], \tag{A15}$$

$$\left(\nabla\bullet\vec{\vec{\Pi}}\right)_\theta = \frac{1}{H}\frac{\partial}{\partial r}\left(Rh_\theta\Pi_{r\theta}\right) + \frac{1}{H}\frac{\partial}{\partial\theta}\left(h_r h_\phi\Pi_{\theta\theta}\right) - \frac{1}{h_\theta h_r}\frac{\partial h_r}{\partial\theta}\Pi_{rr} + \frac{1}{h_\theta h_r}\frac{\partial h_\theta}{\partial r}\Pi_{\theta r} - \frac{1}{Rh_\theta}\frac{\partial R}{\partial\theta}\Pi_{\phi\phi}, \tag{A16}$$

$$\left(\nabla\bullet\vec{\vec{\Pi}}\right)_r = \frac{1}{H}\frac{\partial}{\partial r}\left(Rh_\theta\Pi_{rr}\right) + \frac{1}{H}\frac{\partial}{\partial\theta}\left(h_r h_\phi\Pi_{\theta r}\right) + \frac{1}{h_\theta h_r}\frac{\partial h_r}{\partial\theta}\Pi_{r\theta} - \frac{1}{h_\theta h_r}\frac{\partial h_\theta}{\partial r}\Pi_{\theta\theta} - \frac{1}{Rh_r}\frac{\partial R}{\partial r}\Pi_{\phi\phi}, \tag{A17}$$

where $H \equiv h_r h_\theta h_\phi$.

APPENDIX B

REVISED CIRCULAR MODEL FORMALISM

B1. Continuity Equation (cosine and sine moments):

$$\widetilde{V}_{\theta j}^{s} = -\widetilde{n}_{j}^{s}, \tag{B1}$$

$$\widetilde{V}_{\theta j}^{c} = -\left(1+\widetilde{n}_{j}^{c}\right) \tag{B2}$$

B2. Electron Poloidal Momentum Balance Equation (cosine and sine moments):

$$\widetilde{\Phi}^{c,s} = T_e \widetilde{n}_e^{c,s} \Big/ \overline{\Phi e} \tag{B3}$$

B3. Radial Momentum Balance Equation (1, cosine, and sine moments):

$$\widehat{\Phi}_j^{'} = \frac{\overline{\Phi}^{'}}{V_{thj}} \equiv \frac{1}{V_{thj}\overline{B}_\theta}\frac{\partial \overline{\Phi}}{\partial r} = -\frac{\overline{E}_r}{V_{thj}\overline{B}_\theta} = \widehat{V}_{\theta j} - \widehat{V}_{\phi j} - \widehat{P}_j^{'}, \tag{B4}$$

$$\widetilde{V}_{\phi j}^{c} = 1 - \frac{\widehat{V}_{\theta j}}{\widehat{V}_{\phi j}}\left(\widetilde{\Phi}^{c} + 2 + \widetilde{n}_j^{c}\right) + \widetilde{\Phi}^{c}\left(1+\frac{\widehat{P}_j^{'}}{\widehat{V}_{\phi j}}\right), \tag{B5}$$

$$\widetilde{V}_{\phi j}^{s} = -\frac{\widehat{V}_{\theta j}}{\widehat{V}_{\phi j}}\left(\widetilde{n}_j^{s} + \widetilde{\Phi}^{s}\right) + \left(1+\frac{\widehat{P}_j^{'}}{\widehat{V}_{\phi j}}\right)\widetilde{\Phi}^{s} \tag{B6}$$

B4. Poloidal Momentum Balance Equation (1 moment):

$$\begin{aligned}
&\widehat{V}_{\theta j}^{2}\left[\frac{1}{2}q\varepsilon f_p\left(\widetilde{n}_j^{s} + \widetilde{\Phi}^{s}\right)\right] \\
&-\widehat{V}_{\theta j}\left[\frac{1}{2}q\varepsilon f_p\left(\widehat{V}_{\phi j} + \widehat{P}_j^{'}\right)\widetilde{\Phi}^{s} - q^2 f_j f_p\left(1 + \widetilde{\Phi}^{c} + \frac{2}{3}\widetilde{n}_j^{c}\right) + f_p\sum_{j\neq k}\overline{\nu}_{jk}^{*} + f_p\nu_{atomj}^{*}\right] \\
&+\widehat{V}_{\theta k}\left(f_p\sum_{j\neq k}\overline{\nu}_{jk}^{*}\sqrt{\frac{m_j}{m_k}}\right) \\
&= q^2 f_j f_p\left(\widehat{V}_{\phi j} + \widehat{P}_j^{'}\right)\widetilde{\Phi}^{c} + \frac{1}{4}q\varepsilon\widetilde{n}_j^{s} + \frac{1}{4}q\varepsilon\overline{\overline{\Phi}}_j\widetilde{\Phi}^{s} + \widehat{V}_{rj} - \left\langle M_{\theta j}\right\rangle\frac{qR_0}{\overline{n}_j m_j V_{thj}^2}
\end{aligned} \tag{B7}$$

B5. Poloidal Momentum Balance Equation (cosine moment):

$$\begin{aligned}
&\tilde{n}_j^c\left(\hat{V}_{\theta j}\frac{1}{3\varepsilon}q^2 f_p f_j-\frac{1}{2}f_p\varepsilon\sum_{j\neq k}\bar{\nu}_{jk}^{*}\sqrt{\frac{m_j}{m_k}}\hat{V}_{\theta k}+\frac{1}{2}\varepsilon\hat{V}_{rj}\right)\\
&+\tilde{n}_j^s\left(-\frac{1}{2}qf_p^2\hat{V}_{\theta j}^2+\frac{1}{4}q\right)+\tilde{n}_k^c\left(\frac{1}{2}f_p\varepsilon\sum_{j\neq k}\bar{\nu}_{jk}^{*}\hat{V}_{\theta j}\right)\\
&=-\frac{1}{2\varepsilon}q^2 f_p f_j\hat{V}_{\theta j}-\frac{1}{4}q\bar{\bar{\Phi}}_j\tilde{\Phi}^s\\
&+\frac{1}{2\varepsilon}q^2 f_p f_j\left(\hat{V}_{\phi j}-\hat{V}_{\theta j}+\hat{P}_j^{'}\right)\tilde{\Phi}^c+\left\langle\cos\theta M_{\theta j}\right\rangle\frac{qR_0}{\bar{n}_j m_j V_{thj}^2}
\end{aligned}\tag{B8}$$

B6. Poloidal Momentum Balance Equation (sine moment):

$$\begin{aligned}
&\tilde{n}_j^c\left(\frac{1}{2}qf_p^2\hat{V}_{\theta j}^2-\frac{1}{4}q\right)+\tilde{n}_j^s\left(\hat{V}_{\theta j}\frac{1}{3\varepsilon}q^2 f_p f_j-\frac{1}{2}f_p\varepsilon\sum_{j\neq k}\bar{\nu}_{jk}^{*}\sqrt{\frac{m_j}{m_k}}\hat{V}_{\theta k}+\frac{1}{2}\varepsilon\hat{V}_{rj}\right)\\
&+\tilde{n}_k^s\left(\frac{1}{2}f_p\varepsilon\sum_{j\neq k}\bar{\nu}_{jk}^{*}\hat{V}_{\theta j}\right)\\
&=-\frac{1}{2}qf_p^2\hat{V}_{\theta j}^2-\frac{1}{2}qf_p\hat{V}_{\theta j}\hat{V}_{\phi j}+\frac{1}{2\varepsilon}q^2 f_p f_j\left(\hat{V}_{\phi j}-\hat{V}_{\theta j}+\hat{P}_j^{'}\right)\tilde{\Phi}^s\\
&+\frac{1}{4}q\bar{\bar{\Phi}}_j\tilde{\Phi}^c+\left\langle\sin\theta M_{\theta j}\right\rangle\frac{qR_0}{\bar{n}_j m_j V_{thj}^2}
\end{aligned}\tag{B9}$$

B7. Angular Inertial Torque (1 moment):

$$\left\langle n_j m_j R^2\nabla\phi\bullet\left(\vec{\mathrm{V}}_j\bullet\nabla\right)\vec{\mathrm{V}}_j\right\rangle=R_0\bar{n}_j m_j\nu_{nj}\bar{V}_{\phi j}\tag{B10}$$

where

$$\begin{aligned}
\nu_{nj}&\equiv\frac{1}{2}\frac{\bar{V}_{rj}}{R_0}\left[\varepsilon\left(1+\tilde{n}_j^c+\tilde{V}_{\phi j}^c\right)-2R_0L_{\bar{V}_{\phi j}}^{-1}\right]\\
&=\frac{1}{2}\frac{\bar{V}_{rj}}{R_0}\left\{\varepsilon\left[2+\tilde{n}_j^c-\frac{\hat{V}_{\theta j}}{\hat{V}_{\phi j}}\left(\tilde{\Phi}^c+2+\tilde{n}_j^c\right)+\tilde{\Phi}^c\left(1+\frac{\hat{P}_j^{'}}{\hat{V}_{\phi j}}\right)\right]-2R_0L_{\bar{V}_{\phi j}}^{-1}\right\}
\end{aligned}\tag{B11}$$

B8. Angular Viscous Torque (1 moment):

$$\left\langle R^2\nabla\phi\bullet\nabla\bullet\vec{\vec{\Pi}}\right\rangle\approx\left\langle\left(R^2\nabla\phi\bullet\nabla\bullet\vec{\vec{\Pi}}\right)_{gv}\right\rangle=-\left\langle\frac{1}{Rh_\theta h_r}\frac{\partial}{\partial r}\left(R^3\eta_4\frac{\partial\left(V_{\phi j}R^{-1}\right)}{\partial\theta}\right)\right\rangle\equiv R_0\bar{n}_j m_j\nu_{dj}\bar{V}_{\phi j}\tag{B12}$$

where

$$\nu_{dj} = -\frac{1}{2}\frac{T_j}{R_0^{\,2} e_j \overline{B}_\phi}\left(4\widetilde{V}^s_{\phi j} + \tilde{n}^s_j\right) + \frac{1}{2}\frac{\tilde{\theta}_j G_j T_j}{R_0^{\,2} e_j \overline{B}_\phi}$$
$$= \frac{1}{2}\frac{T_j}{R_0^{\,2} e_j \overline{B}_\phi}\left[4\frac{\widehat{V}_{\theta j}}{\widehat{V}_{\phi j}}\left(\tilde{n}^s_j + \widetilde{\Phi}^s\right) - 4\left(1 + \frac{\widehat{P}'_j}{\widehat{V}_{\phi j}}\right)\widetilde{\Phi}^s - \tilde{n}^s_j\right] + \frac{1}{2}\frac{G_j \tilde{\theta}_j T_j}{R_0^{\,2} e_j \overline{B}_\phi}, \tag{B13}$$

$$G_j \equiv r\left(L^{-1}_{n_j} + L^{-1}_{T_j} + L^{-1}_{\overline{V}_\phi}\right), \tag{B14}$$

$$\tilde{\theta}_j \equiv \widetilde{V}^s_{\phi j}\left(4 + \tilde{n}^c_j\right) + \tilde{n}^s_j\left(1 - \widetilde{V}^c_{\phi j}\right)$$
$$= \left(4 + \tilde{n}^c_j\right)\left[-\frac{\widehat{V}_{\theta j}}{\widehat{V}_{\phi j}}\left(\tilde{n}^s_j + \widetilde{\Phi}^s\right) + \left(1 + \frac{\widehat{P}'_j}{\widehat{V}_{\phi j}}\right)\widetilde{\Phi}^s\right] + \tilde{n}^s_j\left[\frac{\widehat{V}_{\theta j}}{\widehat{V}_{\phi j}}\left(\widetilde{\Phi}^c + 2 + \tilde{n}^c_j\right) - \widetilde{\Phi}^c\left(1 + \frac{\widehat{P}'_j}{\widehat{V}_{\phi j}}\right)\right] \tag{B15}$$

B9. Toroidal Angular Momentum Balance Equation (1 moment):

$$\overline{n}_j m_j \sum_{j\neq k}\overline{\nu}_{jk}\left[\left(1 + \frac{\nu_{nj} + \nu_{dj} + S_{nbj}/\overline{n}_j}{\sum_{j\neq k}\overline{\nu}_{jk}}\right)\overline{V}_{\phi j} - \overline{V}_{\phi k}\right] = \overline{n}_j e_j \mathrm{E}^A_\phi + e_j \Gamma_{nj}\overline{B}_\theta + \overline{M}_{\phi j} \tag{B16}$$

APPENDIX C

COEFFICIENTS IN THE MILLER MODEL FORMALISM

C1. Poloidal momentum balance equation (1 moment):

$$A_{11} = qrf_p^2 \tilde{n}_j^s \left(\left\langle \frac{\cos\theta}{h_\theta} \right\rangle + \frac{\left\langle \frac{1}{R}\frac{\partial R}{\partial \theta}\frac{\sin\theta}{h_\theta} \right\rangle}{\left\langle \frac{\sin^2\theta}{h_\theta} \right\rangle} \left\langle \frac{\cos^2\theta}{h_\theta} \right\rangle \right),$$

$$A_{12} =, \left[\begin{array}{l} -q^2 R_0^{\,2} f_p f_j \left\{ \begin{array}{l} \tilde{n}_j^c \varepsilon \left[-\frac{1}{3} \frac{\left\langle \frac{1}{R}\frac{\partial R}{\partial \theta}\sin\theta\frac{1}{h_\theta} \right\rangle}{\left\langle \frac{\sin^2\theta}{h_\theta} \right\rangle} \left(\left\langle \frac{\sin^2\theta}{(h_\theta)^2} \right\rangle - \left\langle \frac{\cos^2\theta}{(h_\theta)^2} \right\rangle \right) + \frac{1}{3} \left\langle \frac{\partial h_\theta}{\partial \theta}\frac{\sin\theta}{(h_\theta)^3} \right\rangle - \left\langle \frac{1}{R}\frac{\partial R}{\partial \theta}\frac{\sin\theta}{(h_\theta)^2} \right\rangle - \frac{1}{3}\left\langle \frac{\cos\theta}{(h_\theta)^2} \right\rangle \right] \\ +3\langle Q \rangle + \langle M \rangle \\ + \frac{\left\langle \frac{1}{R}\frac{\partial R}{\partial \theta}\sin\theta\frac{1}{h_\theta} \right\rangle}{\left\langle \frac{\sin^2\theta}{h_\theta} \right\rangle} \left(-\frac{1}{3}\left\langle \frac{\partial h_\theta}{\partial \theta}\frac{\sin\theta}{(h_\theta)^3} \right\rangle + \left\langle \frac{1}{R}\frac{\partial R}{\partial \theta}\frac{\sin\theta}{(h_\theta)^2} \right\rangle + \frac{1}{3}\left\langle \frac{\cos\theta}{(h_\theta)^2} \right\rangle + \langle M\cos\theta \rangle - \langle P\sin\theta \rangle \right) \end{array} \right\} \\ +qrf_p \hat{V}_{\phi j} \tilde{V}_\phi^s \left\langle \frac{1}{R}\frac{\partial R}{\partial \theta}\frac{\sin\theta}{h_\theta} \right\rangle - f_p \sum_{j\neq k} \bar{\nu}_{jk}^* - f_p \nu_{atomj}^* \end{array} \right],$$

$$A_{13} = f_p \sum_{j\neq k} \bar{\nu}_{jk}^* \sqrt{\frac{m_j}{m_k}},$$

$$B_1 = \hat{V}_{\phi j} \tilde{V}_{\phi j}^c q^2 R_0^{\,2} f_j f_p \varepsilon \left(\left\langle \frac{\partial h_\theta}{\partial \theta}\frac{\sin\theta}{(h_\theta)^3} \right\rangle - \left\langle \frac{\cos\theta}{(h_\theta)^2} \right\rangle - \langle N\cos\theta \rangle - 2\left\langle \frac{1}{R}\frac{\partial R}{\partial \theta}\frac{\sin\theta}{(h_\theta)^2} \right\rangle \right)$$

$$+\hat{V}_{\phi j} q^2 R_0^{\,2} f_j f_p \left[\varepsilon \tilde{n}_j^c \left(\left\langle \frac{1}{R}\frac{\partial R}{\partial \theta}\sin\theta\frac{1}{(h_\theta)^2} \right\rangle - \langle N\cos\theta \rangle \right) - \langle N \rangle - 3\left\langle \left(\frac{1}{R}\frac{\partial R}{\partial \theta} \right)^2 \frac{1}{(h_\theta)^2} \right\rangle \right] \qquad \text{(C1)}$$

$$+\frac{1}{2} qr\tilde{n}_j^s \left\langle \frac{\cos\theta}{h_\theta} \right\rangle - \langle M_{\theta j} \rangle \frac{qR_0}{n_j m_j V_{thj}^2} + \hat{V}_{rj} \left\langle \frac{1}{(1+\varepsilon\cos\xi)} \right\rangle$$

$$+\frac{1}{2} qr\varepsilon \bar{\bar{\Phi}}_j \left[\tilde{\Phi}^s \left(\frac{1}{\varepsilon} \left\langle \frac{\cos\theta}{h_\theta} \right\rangle + \tilde{n}_j^c \left\langle \frac{\cos^2\theta}{h_\theta} \right\rangle \right) - \tilde{n}_j^s \tilde{\Phi}^c \left\langle \frac{\sin^2\theta}{h_\theta} \right\rangle \right]$$

where q is safety factor, M_θ is poloidal momentum input, $f_p \equiv \overline{B}_\theta \big/ \overline{B}_\phi$, $\nu^*_{atomj} \equiv \dfrac{qR_0}{V_{thj}}\bar{\nu}_{atomj}$,

$\hat{V}_{rj} \equiv \dfrac{qR_0 e_j \overline{B}_\phi}{m_j V_{thj}^2}\bar{V}_{rj}$, $\bar{\bar{\Phi}}_j \equiv \dfrac{e_j\overline{\Phi}}{\frac{1}{2}m_j V_{thj}^2} = \dfrac{e_j\overline{\Phi}}{T_j} = \dfrac{Z_j e\overline{\Phi}}{T_j}$, $\bar{\nu}^*_{jk} \equiv \dfrac{qR_0}{V_{thj}}\bar{\nu}_{jk}$, $f_j \equiv \dfrac{\varepsilon^{-3/2}\nu^*_{jj}}{\left(1+\varepsilon^{-3/2}\nu^*_{jj}\right)\left(1+\nu^*_{jj}\right)}$,

$\hat{\Phi}'_j = \dfrac{\overline{\Phi}'}{V_{thj}} \equiv \dfrac{1}{V_{thj}\overline{B}_\theta}\dfrac{\partial\overline{\Phi}}{\partial r} = -\dfrac{\overline{E}_r}{V_{thj}\overline{B}_\theta}$, $\nu^*_{jj} \equiv \dfrac{\nu_{jj}qR_0}{V_{thj}} = \dfrac{qR_0}{V_{thj}\tau_{jj}}$, $\tilde{\Phi}^{c,c} \approx \dfrac{T_e\tilde{n}_e^{c,s}}{\overline{\Phi}e}$,

$N \equiv -\left(\dfrac{1}{R}\dfrac{\partial R}{\partial\theta}\right)^2\dfrac{1}{\left(h_\theta\right)^2} - \dfrac{\partial h_\theta}{\partial\theta}\dfrac{1}{R}\dfrac{\partial R}{\partial\theta}\dfrac{1}{\left(h_\theta\right)^3} + \dfrac{1}{R}\dfrac{\partial^2 R}{\partial\theta^2}\dfrac{1}{\left(h_\theta\right)^2}$,

$M \equiv N + \dfrac{1}{3}\left[-\left(\dfrac{1}{B_\theta}\dfrac{\partial B_\theta}{\partial\theta}\right)^2\dfrac{1}{\left(h_\theta\right)^2} - \dfrac{\partial h_\theta}{\partial\theta}\dfrac{1}{B_\theta}\dfrac{\partial B_\theta}{\partial\theta}\dfrac{1}{\left(h_\theta\right)^3} + \dfrac{1}{B_\theta}\dfrac{\partial^2 B_\theta}{\partial\theta^2}\dfrac{1}{\left(h_\theta\right)^2}\right]$,

$P \equiv \dfrac{1}{R}\dfrac{\partial R}{\partial\theta}\dfrac{1}{\left(h_\theta\right)^2} + \dfrac{1}{3}\dfrac{1}{B_\theta}\dfrac{\partial B_\theta}{\partial\theta}\dfrac{1}{\left(h_\theta\right)^2}$, $Q \equiv \left(\dfrac{1}{R}\dfrac{\partial R}{\partial\theta}\right)^2\dfrac{1}{\left(h_\theta\right)^2} + \dfrac{1}{3}\left(\dfrac{1}{R}\dfrac{\partial R}{\partial\theta}\right)\left(\dfrac{1}{B_\theta}\dfrac{\partial B_\theta}{\partial\theta}\right)\dfrac{1}{\left(h_\theta\right)^2}$

with $\overline{\Phi}$ being the average electric potential.

C2. Poloidal momentum balance equation (cosine moment):

$$A_{C1} = q^2 R_0 r f_j f_p \begin{bmatrix} -\hat{V}_{\theta j}\dfrac{1}{3}\left(-\left\langle\dfrac{\partial h_\theta}{\partial\theta}\dfrac{\sin\theta\cos\theta}{\left(h_\theta\right)^3}\right\rangle + \left\langle\dfrac{\cos^2\theta}{\left(h_\theta\right)^2}\right\rangle\right) - \hat{V}_{\phi j}\left\langle N\cos^2\theta\right\rangle \\ -\sum_{j\neq k}\bar{\nu}^*_{jk}\varepsilon f_p\sqrt{\dfrac{m_j}{m_k}}\hat{V}_{\theta k}\left\langle\cos^2\theta\right\rangle - \hat{V}_{rj}\varepsilon\left\langle\dfrac{\cos^2\theta}{\left(1+\varepsilon\cos\xi\right)}\right\rangle \end{bmatrix},$$

$$A_{C2} = qr\left(-f_p^2\hat{V}_{\theta j}{}^2\left\langle\cos^2\theta\dfrac{1}{h_\theta}\right\rangle + \dfrac{1}{2}\left\langle\dfrac{\cos^2\theta}{h_\theta}\right\rangle\right), \qquad A_{C3} = \sum_{j\neq k}\bar{\nu}^*_{jk}\varepsilon f_p\hat{V}_{\theta j}\left\langle\cos^2\theta\right\rangle,$$

$$
\begin{aligned}
&B_C = qrf_p \hat{V}_{\theta j}\hat{V}_{\phi j}\widetilde{V}_{\phi}^{s}\left\langle \frac{1}{R}\frac{\partial R}{\partial\theta}\sin\theta\cos\theta\frac{1}{h_\theta}\right\rangle \\
&-\hat{V}_{\theta j}q^2R_0^{\,2}f_jf_p\left[\begin{array}{l}\dfrac{\left\langle \dfrac{1}{R}\dfrac{\partial R}{\partial\theta}\dfrac{\sin\theta}{h_\theta}\right\rangle}{\left\langle \dfrac{\sin^2\theta}{h_\theta}\right\rangle}\left(-\dfrac{1}{3}\left\langle \dfrac{\partial h_\theta}{\partial\theta}\dfrac{\sin\theta\cos\theta}{(h_\theta)^3}\right\rangle+\dfrac{1}{3}\left\langle \dfrac{\cos^2\theta}{(h_\theta)^2}\right\rangle+\langle M\cos^2\theta\rangle-\langle P\sin\theta\cos\theta\rangle\right)\\ +\langle M\cos\theta\rangle+3\langle Q\cos\theta\rangle\end{array}\right] \\
&-\hat{V}_{\phi j}\widetilde{V}_{\phi j}^{c}q^2R_0rf_jf_p\left(\left\langle \frac{\partial h_\theta}{\partial\theta}\frac{\sin\theta\cos\theta}{(h_\theta)^3}\right\rangle-\left\langle \frac{\cos^2\theta}{(h_\theta)^2}\right\rangle-\langle N\cos^2\theta\rangle\right) \\
&-\hat{V}_{\phi j}q^2R_0^{\,2}f_jf_p\langle N\cos\theta\rangle+\langle\cos\theta M_{\theta j}\rangle\frac{qR_0}{\bar{n}_jm_jV_{thj}^2} \\
&-\sum_{j\neq k}\bar{\nu}_{jk}^{*}f_p\left(\hat{V}_{\theta j}-\sqrt{\frac{m_j}{m_k}}\hat{V}_{\theta k}\right)\left(\langle\cos\theta\rangle+\frac{\left\langle \dfrac{1}{R}\dfrac{\partial R}{\partial\theta}\dfrac{\sin\theta}{h_\theta}\right\rangle}{\left\langle \dfrac{\sin^2\theta}{h_\theta}\right\rangle}\langle\cos^2\theta\rangle\right)-\hat{V}_{rj}\left\langle \frac{\cos\theta}{(1+\varepsilon\cos\xi)}\right\rangle \\
&-\frac{1}{2}qr\bar{\bar{\Phi}}_j\widetilde{\Phi}^{s}\left\langle \frac{\cos^2\theta}{h_\theta}\right\rangle-f_p\nu_{atomj}^{*}\hat{V}_{\theta j}\left(\langle\cos\theta\rangle+\frac{\left\langle \dfrac{1}{R}\dfrac{\partial R}{\partial\theta}\dfrac{\sin\theta}{h_\theta}\right\rangle}{\left\langle \dfrac{\sin^2\theta}{h_\theta}\right\rangle}\langle\cos^2\theta\rangle\right)
\end{aligned}
\tag{C2}
$$

where $\widetilde{V}_{\phi}^{c,s}$ given in Eqs. (A4) and (A5).

C3. Poloidal momentum balance equation (sine moment):

$$
\begin{aligned}
&A_{S1} = qrf_p^2\hat{V}_{\theta j}^{\,2}\left\langle \sin^2\theta\frac{1}{h_\theta}\right\rangle-\frac{1}{2}qr\left\langle \frac{\sin^2\theta}{h_\theta}\right\rangle, \\
&A_{S2} = q^2R_0rf_jf_p\left[-\hat{V}_{\theta j}\frac{1}{3}\left(\left\langle \frac{\partial h_\theta}{\partial\theta}\frac{\sin\theta\cos\theta}{(h_\theta)^3}\right\rangle+\left\langle \frac{\sin^2\theta}{(h_\theta)^2}\right\rangle+\langle P\sin\theta\cos\theta\rangle\right)-\hat{V}_{\phi j}3\left\langle\left(\frac{1}{R}\frac{\partial R}{\partial\theta}\right)^2\frac{\sin^2\theta}{(h_\theta)^2}\right\rangle\right] \\
&-\varepsilon\sum_{j\neq k}\bar{\nu}_{jk}^{*}f_p\sqrt{\frac{m_j}{m_k}}\hat{V}_{\theta k}\langle\sin^2\theta\rangle+\hat{V}_{rj}\varepsilon\left\langle \frac{\sin^2\theta}{(1+\varepsilon\cos\xi)}\right\rangle, \\
&A_{S3} = \varepsilon\sum_{j\neq k}\bar{\nu}_{jk}^{*}f_p\hat{V}_{\theta j}\langle\sin^2\theta\rangle, \\
&\\
&B_S = qrf_p^2\hat{V}_{\theta j}^{\,2}\frac{1}{\varepsilon}\left\langle \frac{1}{R}\frac{\partial R}{\partial\theta}\sin\theta\frac{1}{h_\theta}\right\rangle+qrf_p\hat{V}_{\theta j}\hat{V}_{\phi j}\frac{1}{\varepsilon}\left\langle \frac{1}{R}\frac{\partial R}{\partial\theta}\sin\theta\frac{1}{h_\theta}\right\rangle \\
&-\hat{V}_{\phi j}\widetilde{V}_{\phi j}^{s}q^2R_0rf_jf_p\left[-\left\langle \frac{\partial h_\theta}{\partial\theta}\frac{\sin\theta\cos\theta}{(h_\theta)^3}\right\rangle-\left\langle \frac{\sin^2\theta}{(h_\theta)^2}\right\rangle-3\left\langle\left(\frac{1}{R}\frac{\partial R}{\partial\theta}\right)^2\frac{\sin^2\theta}{(h_\theta)^2}\right\rangle\right] \\
&+\langle\sin\theta M_{\theta j}\rangle\frac{qR_0}{\bar{n}_jm_jV_{thj}^2}+\frac{1}{2}qr\bar{\bar{\Phi}}_j\widetilde{\Phi}^{c}\left\langle \frac{\sin^2\theta}{h_\theta}\right\rangle
\end{aligned}
\tag{C3}
$$

where

$$\widetilde{V}^{c}_{\phi j}=\alpha^{1C}_{j}+\frac{\widehat{\Phi}^{'}_{j}}{\widehat{V}_{\phi j}}\alpha^{2C}_{j}+\frac{\widehat{V}_{\theta j}}{\widehat{V}_{\phi j}}\alpha^{3C}_{j}+\frac{\widehat{P}^{'}_{j}}{\widehat{V}_{\phi j}}\alpha^{4C}_{j}\equiv\frac{\widehat{V}_{\theta j}}{\widehat{V}_{\phi j}}\alpha^{3C}_{j}+H^{1C}_{j}=\tilde{n}^{c}_{j}\alpha^{5C}_{j}+H^{2C}_{j}$$
$$=\frac{\widehat{V}_{\theta j}}{\widehat{V}_{\phi j}}\left[\alpha^{3C}_{j}+\alpha^{2C}_{j}\frac{\left\langle\frac{1}{1+\varepsilon\cos\xi}\right\rangle}{\left\langle\frac{1}{h_r}\right\rangle}\right]+\alpha^{1C}_{j}-\alpha^{2C}_{j}\left(1+\frac{\partial R_0(r)}{\partial r}\right)\frac{\left\langle\frac{1}{(1+\varepsilon\cos\xi)}\frac{1}{h_r}\right\rangle}{\left\langle\frac{1}{h_r}\right\rangle}-\frac{\widehat{P}^{'}_{j}}{\widehat{V}_{\phi j}}\left(\alpha^{2C}_{j}-\alpha^{4C}_{j}\right) \tag{C4}$$

$$\widetilde{V}^{s}_{\phi j}=\tilde{n}^{s}_{j}\alpha^{1S}_{j}+\alpha^{2S}_{j}=-\frac{\widehat{V}_{\theta j}}{\widehat{V}_{\phi j}}\frac{\left\langle\frac{1}{1+\varepsilon\cos\xi}\right\rangle}{\left\langle\frac{1}{h_r}\right\rangle}\frac{\left\langle\sin^2\theta\frac{1}{h_r}\right\rangle}{\left(1+\frac{\partial R_0(r)}{\partial r}\right)\left\langle\frac{\sin^2\theta}{(1+\varepsilon\cos\xi)}\frac{1}{h_r}\right\rangle}\left[\tilde{n}^{s}_{j}+\widetilde{\Phi}^{s}\right]$$
$$+\frac{1}{\widehat{V}_{\phi j}}\left(\widehat{V}_{\phi j}\left(1+\frac{\partial R_0(r)}{\partial r}\right)\frac{\left\langle\frac{1}{(1+\varepsilon\cos\xi)}\frac{1}{h_r}\right\rangle}{\left\langle\frac{1}{h_r}\right\rangle}+\widehat{P}^{'}_{j}\right)\frac{\left\langle\sin^2\theta\frac{1}{h_r}\right\rangle}{\left(1+\frac{\partial R_0(r)}{\partial r}\right)\left\langle\frac{\sin^2\theta}{(1+\varepsilon\cos\xi)}\frac{1}{h_r}\right\rangle}\left[\tilde{n}^{s}_{j}+\widetilde{\Phi}^{s}\right] \tag{C5}$$
$$-\frac{1}{\widehat{V}_{\phi j}}\tilde{n}^{s}_{j}\frac{\left\langle\sin^2\theta\frac{1}{h_r}\right\rangle}{\left(1+\frac{\partial R_0(r)}{\partial r}\right)\left\langle\frac{\sin^2\theta}{(1+\varepsilon\cos\xi)}\frac{1}{h_r}\right\rangle}\left(\widehat{P}^{'}_{j}+\widehat{V}_{\phi j}\right)$$

with

$$\alpha^{1C}_{j}\equiv-\frac{1}{\varepsilon}\frac{\left\langle\frac{\cos\theta}{(1+\varepsilon\cos\xi)}\frac{1}{h_r}\right\rangle+\varepsilon\tilde{n}^{c}_{j}\left\langle\frac{\cos^2\theta}{(1+\varepsilon\cos\xi)}\frac{1}{h_r}\right\rangle}{\left\langle\frac{\cos^2\theta}{(1+\varepsilon\cos\xi)}\frac{1}{h_r}\right\rangle},\qquad \alpha^{2C}_{j}\equiv-\frac{1}{\varepsilon}\frac{\left\langle\cos\theta\frac{1}{h_r}\right\rangle+\varepsilon\left(\tilde{n}^{c}_{j}+\widetilde{\Phi}^{c}\right)\left\langle\cos^2\theta\frac{1}{h_r}\right\rangle}{\left(1+\frac{\partial R_0(r)}{\partial r}\right)\left\langle\frac{\cos^2\theta}{(1+\varepsilon\cos\xi)}\frac{1}{h_r}\right\rangle},$$

$$\alpha^{3C}_{j}\equiv\frac{1}{\varepsilon}\frac{\left\langle\frac{\cos\theta}{1+\varepsilon\cos\xi}\right\rangle+\frac{\left\langle\frac{1}{R}\frac{\partial R}{\partial\theta}\sin\theta\frac{1}{h_\theta}\right\rangle}{\left\langle\sin^2\theta\frac{1}{h_\theta}\right\rangle}\left\langle\frac{\cos^2\theta}{1+\varepsilon\cos\xi}\right\rangle}{\left(1+\frac{\partial R_0(r)}{\partial r}\right)\left\langle\frac{\cos^2\theta}{(1+\varepsilon\cos\xi)}\frac{1}{h_r}\right\rangle},\qquad \alpha^{4C}_{j}\equiv-\frac{1}{\varepsilon}\frac{\left\langle\cos\theta\frac{1}{h_r}\right\rangle+\varepsilon\tilde{n}^{c}_{j}\left\langle\cos^2\theta\frac{1}{h_r}\right\rangle}{\left(1+\frac{\partial R_0(r)}{\partial r}\right)\left\langle\frac{\cos^2\theta}{(1+\varepsilon\cos\xi)}\frac{1}{h_r}\right\rangle}$$

$$\alpha_j^{5C} \equiv \frac{1}{\left\langle \frac{\cos^2\theta}{(1+\varepsilon\cos\xi)}\frac{1}{h_r}\right\rangle}\left[-\left\langle \frac{\cos^2\theta}{(1+\varepsilon\cos\xi)}\frac{1}{h_r}\right\rangle - \frac{\hat{\Phi}_j'}{\hat{V}_{\phi j}}\frac{\left\langle \cos^2\theta\frac{1}{h_r}\right\rangle}{\left(1+\frac{\partial R_0(r)}{\partial r}\right)} - \frac{\hat{P}_j'}{\hat{V}_{\phi j}}\frac{\left\langle \cos^2\theta\frac{1}{h_r}\right\rangle}{\left(1+\frac{\partial R_0(r)}{\partial r}\right)}\right]$$

$$H_j^{1C} \equiv \alpha_j^{1C} + \frac{\hat{\Phi}_j'}{\hat{V}_{\phi j}}\alpha_j^{2C} + \frac{\hat{P}_j'}{\hat{V}_{\phi j}}\alpha_j^{4C} = \frac{\hat{V}_{\theta j}}{\hat{V}_{\phi j}}\frac{\left\langle \frac{1}{1+\varepsilon\cos\xi}\right\rangle}{\left\langle \frac{1}{h_r}\right\rangle}\alpha_j^{2C}$$

$$+\alpha_j^{1C} - \left(1+\frac{\partial R_0(r)}{\partial r}\right)\frac{\left\langle \frac{1}{(1+\varepsilon\cos\xi)}\frac{1}{h_r}\right\rangle}{\left\langle \frac{1}{h_r}\right\rangle}\alpha_j^{2C} - \frac{\hat{P}_j'}{\hat{V}_{\phi j}}\left(\alpha_j^{2C} - \alpha_j^{4C}\right)$$

$$H_j^{2C} \equiv -\frac{1}{\varepsilon\left\langle \frac{\cos^2\theta}{(1+\varepsilon\cos\xi)}\frac{1}{h_r}\right\rangle}\left[\begin{array}{l}\left\langle \frac{\cos\theta}{(1+\varepsilon\cos\xi)}\frac{1}{h_r}\right\rangle + \frac{\hat{\Phi}_j'}{\hat{V}_{\phi j}}\frac{1}{\left(1+\frac{\partial R_0(r)}{\partial r}\right)}\left(\left\langle \cos\theta\frac{1}{h_r}\right\rangle + \varepsilon\tilde{\Phi}^c\left\langle \cos^2\theta\frac{1}{h_r}\right\rangle\right) \\ + \frac{\hat{P}_j'}{\hat{V}_{\phi j}}\frac{\left\langle \cos\theta\frac{1}{h_r}\right\rangle}{\left(1+\frac{\partial R_0(r)}{\partial r}\right)}\end{array}\right] + \frac{\hat{V}_\theta}{\hat{V}_\phi}\alpha_j^{3c}$$

$$\alpha_j^{1S} \equiv -\frac{\left\langle \sin^2\theta\frac{1}{h_r}\right\rangle}{\left(1+\frac{\partial R_0(r)}{\partial r}\right)\left\langle \frac{\sin^2\theta}{(1+\varepsilon\cos\xi)}\frac{1}{h_r}\right\rangle}\left(\frac{\hat{\Phi}_j'}{\hat{V}_{\phi j}} + \frac{\hat{P}_j'}{\hat{V}_{\phi j}} + 1\right), \qquad \alpha_j^{2S} \equiv -\frac{\hat{\Phi}_j'}{\hat{V}_{\phi j}}\tilde{\Phi}^s\frac{\left\langle \sin^2\theta\frac{1}{h_r}\right\rangle}{\left(1+\frac{\partial R_0(r)}{\partial r}\right)\left\langle \frac{\sin^2\theta}{(1+\varepsilon\cos\xi)}\frac{1}{h_r}\right\rangle}$$

Here $\frac{\partial R_0(r)}{\partial r}$ is the Shafranov shift [64]. Note that Eqs. (C4) and (AC) are expressed in several forms to make it easy to couple them with different moments in Eqs. (C1)-(C3).

APPENDIX D

COEFFICIENTS IN THE NUMERICAL CALCULATION MODEL

The coefficients of the final numerical code come from the coefficients in Appendix A updated with the coupling relations between $\widetilde{V}_{\phi j}^{c,s}$ and $\widetilde{n}_j^{c,s}$, Eqs. (C4) and (C5).

D1. Coefficients in the density asymmetry subsystem:

$$
\begin{aligned}
a_{11} &= q^2 R_0 r f_i f_p \left[\left[\frac{1}{3}\hat{V}_{\theta i} + \hat{V}_{\phi i}\alpha_i^{5C} \right] \left(\left\langle \frac{\partial h_\theta}{\partial \theta} \frac{\sin\theta\cos\theta}{(h_\theta)^3} \right\rangle - \left\langle \frac{\cos^2\theta}{(h_\theta)^2} \right\rangle \right) \right] \\
&\quad - \left(\bar{\nu}_{iI}^{*} + \bar{\nu}_{ie}^{*} \right) \varepsilon f_p \sqrt{\frac{m_i}{m_I}} \hat{V}_{\theta I} \left\langle \cos^2\theta \right\rangle + \hat{V}_{ri}\varepsilon \left\langle \frac{\cos^2\theta}{(1+\varepsilon\cos\xi)} \right\rangle \\
a_{12} &= qr \left[-f_p \hat{V}_{\theta i} \left[f_p \hat{V}_{\theta i} \left\langle \frac{\cos^2\theta}{h_\theta} \right\rangle + \hat{V}_{\phi i}\alpha_i^{1S} \left\langle \frac{1}{R}\frac{\partial R}{\partial \theta}\frac{\sin\theta\cos\theta}{h_\theta} \right\rangle \right] + \frac{1}{2}\left\langle \frac{\cos^2\theta}{h_\theta} \right\rangle \right] \\
a_{13} &= \left(\bar{\nu}_{iI}^{*} + \bar{\nu}_{ie}^{*} \right) \varepsilon f_p \hat{V}_{\theta i} \left\langle \cos^2\theta \right\rangle, \qquad a_{14} = 0
\end{aligned}
$$

$$
\begin{aligned}
b_1 &= qr f_p \hat{V}_{\theta i}\hat{V}_{\phi i}\alpha_i^{2S} \left\langle \frac{1}{R}\frac{\partial R}{\partial \theta}\frac{\sin\theta\cos\theta}{h_\theta} \right\rangle \\
&\quad - q^2 R_0^{\,2} f_i f_p \hat{V}_{\theta i} \left[\begin{array}{l} \dfrac{\left\langle \dfrac{1}{R}\dfrac{\partial R}{\partial \theta}\dfrac{\sin\theta}{h_\theta} \right\rangle}{\left\langle \dfrac{\sin^2\theta}{h_\theta} \right\rangle} \left(-\dfrac{1}{3}\left\langle \dfrac{\partial h_\theta}{\partial \theta}\dfrac{\sin\theta\cos\theta}{(h_\theta)^3} \right\rangle + \dfrac{1}{3}\left\langle \dfrac{\cos^2\theta}{(h_\theta)^2} \right\rangle + \left\langle M\cos^2\theta \right\rangle - \left\langle P\sin\theta\cos\theta \right\rangle \right) \\ + \left\langle M\cos\theta \right\rangle + 3\left\langle Q\cos\theta \right\rangle \end{array} \right] \\
&\quad - q^2 R_0^{\,2} f_i f_p \hat{V}_{\phi i} \left[\varepsilon H_i^{2C} \left(\left\langle \frac{\partial h_\theta}{\partial \theta}\frac{\sin\theta\cos\theta}{(h_\theta)^3} \right\rangle - \left\langle \frac{\cos^2\theta}{(h_\theta)^2} \right\rangle - \left\langle N\cos^2\theta \right\rangle \right) - \left\langle N\cos\theta \right\rangle \right] \\
&\quad - \left(\bar{\nu}_{iI}^{*} + \bar{\nu}_{ie}^{*} \right) f_p \left[\hat{V}_{\theta i} - \sqrt{\frac{m_i}{m_I}}\hat{V}_{\theta I} \right] \left(\left\langle \cos\theta \right\rangle + \frac{\left\langle \dfrac{1}{R}\dfrac{\partial R}{\partial \theta}\dfrac{\sin\theta}{h_\theta} \right\rangle}{\left\langle \dfrac{\sin^2\theta}{h_\theta} \right\rangle} \left\langle \cos^2\theta \right\rangle \right) \\
&\quad - \hat{V}_{ri} \left\langle \frac{\cos\theta}{(1+\varepsilon\cos\xi)} \right\rangle - \frac{1}{2} qr \bar{\bar{\Phi}}_i \widetilde{\Phi}^s \left\langle \frac{\cos^2\theta}{h_\theta} \right\rangle - f_p \nu_{atomi}^{*} \hat{V}_{\theta i} \left[\left\langle \cos\theta \right\rangle + \frac{\left\langle \dfrac{1}{R}\dfrac{\partial R}{\partial \theta}\dfrac{\sin\theta}{h_\theta} \right\rangle}{\left\langle \dfrac{\sin^2\theta}{h_\theta} \right\rangle} \left\langle \cos^2\theta \right\rangle \right] + \left\langle \cos\theta M_{\theta i} \right\rangle \frac{qR_0}{\bar{\bar{n}}_i m_i V_{thi}^2}
\end{aligned}
\tag{D1}
$$

$$a_{21} = qr\left[f_p^2 \hat{V}_{\theta i}{}^2 - \frac{1}{2} \right] \left\langle \frac{\sin^2\theta}{h_\theta} \right\rangle$$

$$a_{22} = q^2 R_0 r f_i f_p \left\{ \begin{array}{l} -\left(\frac{1}{3}\hat{V}_{\theta i} + \hat{V}_{\phi i}\alpha_i^{1S} \right) \left[\left\langle \frac{\partial h_\theta}{\partial\theta} \frac{\sin\theta\cos\theta}{(h_\theta)^3} \right\rangle + \left\langle \frac{\sin^2\theta}{(h_\theta)^2} \right\rangle \right] \\ -\frac{1}{3}\hat{V}_{\theta i} \left\langle P\sin\theta\cos\theta \right\rangle - 3\left(\hat{V}_{\phi i}\alpha_i^{1S} + \hat{V}_{\phi i} \right) \left\langle \left(\frac{1}{R}\frac{\partial R}{\partial\theta} \right)^2 \frac{\sin^2\theta}{(h_\theta)^2} \right\rangle \end{array} \right\}$$

$$+\hat{V}_{ri}\varepsilon \left\langle \frac{\sin^2\theta}{(1+\varepsilon\cos\xi)} \right\rangle - \varepsilon\left(\bar{\nu}_{iI}^{*} + \bar{\nu}_{ie}^{*} \right) f_p \sqrt{\frac{m_i}{m_I}} \hat{V}_{\theta I} \left\langle \sin^2\theta \right\rangle$$

$$a_{23} = 0, \qquad a_{24} = \varepsilon\left(\bar{\nu}_{iI}^{*} + \bar{\nu}_{ie}^{*} \right) f_p \hat{V}_{\theta i} \left\langle \sin^2\theta \right\rangle \approx \varepsilon\left(\bar{\nu}_{iI}^{*} + \bar{\nu}_{ie}^{*} \right) f_p \hat{V}_{\theta i} \left\langle \cos^2\theta \right\rangle$$

$$b_2 = qR_0 f_p \hat{V}_{\theta i} \left(f_p \hat{V}_{\theta i} + \hat{V}_{\phi i} \right) \left\langle \frac{1}{R}\frac{\partial R}{\partial\theta} \frac{\sin\theta}{h_\theta} \right\rangle + q^2 R_0 r f_i f_p \hat{V}_{\phi i}\alpha_i^{2S} \left[\left\langle \frac{\partial h_\theta}{\partial\theta} \frac{\sin\theta\cos\theta}{(h_\theta)^3} \right\rangle + \left\langle \frac{\sin^2\theta}{(h_\theta)^2} \right\rangle + 3\left\langle \left(\frac{1}{R}\frac{\partial R}{\partial\theta} \right)^2 \frac{\sin^2\theta}{(h_\theta)^2} \right\rangle \right]$$

$$+\frac{1}{2} qr \overline{\overline{\Phi}}_i \widetilde{\Phi}^c \left\langle \frac{\sin^2\theta}{h_\theta} \right\rangle + \left\langle \sin\theta M_{\theta i} \right\rangle \frac{qR_0}{n_i m_i V_{thi}^2} \qquad \text{(D2)}$$

$$a_{31} = \left(\bar{\nu}_{Ii}^{*} + \bar{\nu}_{Ie}^{*} \right) \varepsilon f_p \hat{V}_{\theta I} \left\langle \cos^2\theta \right\rangle, \qquad a_{32} = 0$$

$$a_{33} = q^2 R_0 r f_I f_p \left[\left[\frac{1}{3}\hat{V}_{\theta I} + \hat{V}_{\phi I}\alpha_I^{5C} \right] \left(\left\langle \frac{\partial h_\theta}{\partial\theta} \frac{\sin\theta\cos\theta}{(h_\theta)^3} \right\rangle - \left\langle \frac{\cos^2\theta}{(h_\theta)^2} \right\rangle \right) \right]$$

$$-\left(\bar{\nu}_{Ii}^{*} + \bar{\nu}_{Ie}^{*} \right) \varepsilon f_p \sqrt{\frac{m_I}{m_i}} \hat{V}_{\theta i} \left\langle \cos^2\theta \right\rangle + \hat{V}_{rI}\varepsilon \left\langle \frac{\cos^2\theta}{(1+\varepsilon\cos\xi)} \right\rangle$$

$$a_{34} = qr\left[-f_p \hat{V}_{\theta I} \left[f_p \hat{V}_{\theta I} \left\langle \frac{\cos^2\theta}{h_\theta} \right\rangle + \hat{V}_{\phi I}\alpha_I^{1S} \left\langle \frac{1}{R}\frac{\partial R}{\partial\theta} \frac{\sin\theta\cos\theta}{h_\theta} \right\rangle \right] + \frac{1}{2}\left\langle \frac{\cos^2\theta}{h_\theta} \right\rangle \right]$$

$$b_3 = qr f_p \hat{V}_{\theta I} \hat{V}_{\phi I}\alpha_I^{2S} \left\langle \frac{1}{R}\frac{\partial R}{\partial\theta} \frac{\sin\theta\cos\theta}{h_\theta} \right\rangle$$

$$-q^2 R_0{}^2 f_I f_p \hat{V}_{\theta I} \left[\begin{array}{l} \frac{\left\langle \frac{1}{R}\frac{\partial R}{\partial\theta}\frac{\sin\theta}{h_\theta} \right\rangle}{\left\langle \frac{\sin^2\theta}{h_\theta} \right\rangle} \left(-\frac{1}{3}\left\langle \frac{\partial h_\theta}{\partial\theta} \frac{\sin\theta\cos\theta}{(h_\theta)^3} \right\rangle + \frac{1}{3}\left\langle \frac{\cos^2\theta}{(h_\theta)^2} \right\rangle + \left\langle M\cos^2\theta \right\rangle - \left\langle P\sin\theta\cos\theta \right\rangle \right) \\ +\left\langle M\cos\theta \right\rangle + 3\left\langle Q\cos\theta \right\rangle \end{array} \right]$$

$$-q^2 R_0{}^2 f_I f_p \hat{V}_{\phi I} \left[\varepsilon H_I^{2C} \left(\left\langle \frac{\partial h_\theta}{\partial\theta} \frac{\sin\theta\cos\theta}{(h_\theta)^3} \right\rangle - \left\langle \frac{\cos^2\theta}{(h_\theta)^2} \right\rangle - \left\langle N\cos^2\theta \right\rangle \right) - \left\langle N\cos\theta \right\rangle \right]$$

$$-\left(\bar{\nu}_{Ii}^{*} + \bar{\nu}_{Ie}^{*} \right) f_p \left[\hat{V}_{\theta I} - \sqrt{\frac{m_I}{m_i}} \hat{V}_{\theta i} \right] \left(\left\langle \cos\theta \right\rangle + \frac{\left\langle \frac{1}{R}\frac{\partial R}{\partial\theta}\frac{\sin\theta}{h_\theta} \right\rangle}{\left\langle \frac{\sin^2\theta}{h_\theta} \right\rangle} \left\langle \cos^2\theta \right\rangle \right)$$

$$-\hat{V}_{rI} \left\langle \frac{\cos\theta}{(1+\varepsilon\cos\xi)} \right\rangle - \frac{1}{2} qr \overline{\overline{\Phi}}_I \widetilde{\Phi}^s \left\langle \frac{\cos^2\theta}{h_\theta} \right\rangle - f_p v_{atomI}^{*} \hat{V}_{\theta I} \left[\left\langle \cos\theta \right\rangle + \frac{\left\langle \frac{1}{R}\frac{\partial R}{\partial\theta}\frac{\sin\theta}{h_\theta} \right\rangle}{\left\langle \frac{\sin^2\theta}{h_\theta} \right\rangle} \left\langle \cos^2\theta \right\rangle \right] + \left\langle \cos\theta M_{\theta I} \right\rangle \frac{qR_0}{n_I m_I V_{thI}^2} \qquad \text{(D3)}$$

$$a_{41}=0, \qquad a_{42}=\varepsilon\left(\bar{\nu}^{*}_{Ii}+\bar{\nu}^{*}_{Ie}\right)f_p\hat{V}_{\theta I}\left\langle\sin^2\theta\right\rangle\approx\varepsilon\left(\bar{\nu}^{*}_{Ii}+\bar{\nu}^{*}_{Ie}\right)f_p\hat{V}_{\theta I}\left\langle\cos^2\theta\right\rangle$$

$$a_{43}=qr\left[f_p^2\hat{V}_{\theta I}{}^2-\frac{1}{2}\right]\left\langle\frac{\sin^2\theta}{h_\theta}\right\rangle$$

$$a_{44}=q^2R_0rf_If_p\left\{\begin{array}{l}-\left(\frac{1}{3}\hat{V}_{\theta I}+\hat{V}_{\phi I}\alpha_I^{1S}\right)\left[\left\langle\frac{\partial h_\theta}{\partial\theta}\frac{\sin\theta\cos\theta}{(h_\theta)^3}\right\rangle+\left\langle\frac{\sin^2\theta}{(h_\theta)^2}\right\rangle\right]\\ -\frac{1}{3}\hat{V}_{\theta I}\left\langle P\sin\theta\cos\theta\right\rangle-3\left(\hat{V}_{\phi I}\alpha_I^{1S}+\hat{V}_{\phi I}\right)\left\langle\left(\frac{1}{R}\frac{\partial R}{\partial\theta}\right)^2\frac{\sin^2\theta}{(h_\theta)^2}\right\rangle\end{array}\right\}$$

$$+\hat{V}_{rI}\varepsilon\left\langle\frac{\sin^2\theta}{(1+\varepsilon\cos\xi)}\right\rangle-\varepsilon\left(\bar{\nu}^{*}_{Ii}+\bar{\nu}^{*}_{Ie}\right)f_p\sqrt{\frac{m_I}{m_i}}\hat{V}_{\theta i}\left\langle\sin^2\theta\right\rangle$$

$$b_4=qR_0f_p\hat{V}_{\theta I}\left(f_p\hat{V}_{\theta I}+\hat{V}_{\phi I}\right)\left\langle\frac{1}{R}\frac{\partial R}{\partial\theta}\frac{\sin\theta}{h_\theta}\right\rangle$$

$$+q^2R_0rf_If_p\hat{V}_{\phi I}\alpha_I^{2S}\left[\left\langle\frac{\partial h_\theta}{\partial\theta}\frac{\sin\theta\cos\theta}{(h_\theta)^3}\right\rangle+\left\langle\frac{\sin^2\theta}{(h_\theta)^2}\right\rangle+3\left\langle\left(\frac{1}{R}\frac{\partial R}{\partial\theta}\right)^2\frac{\sin^2\theta}{(h_\theta)^2}\right\rangle\right]$$

$$+\frac{1}{2}qr\overline{\overline{\Phi}}_I\tilde{\Phi}^c\left\langle\frac{\sin^2\theta}{h_\theta}\right\rangle+\left\langle\sin\theta M_{\theta I}\right\rangle\overline{\overline{\frac{qR_0}{n_Im_IV_{thI}^2}}} \qquad \text{(D4)}$$

D2. Coefficients in the poloidal rotation subsystem:

$$c_{11}=\hat{V}_{\theta i}^{n-1}qrf_p^2\tilde{n}_i^s\left(\left\langle\frac{\cos\theta}{h_\theta}\right\rangle+\frac{\left\langle\frac{1}{R}\frac{\partial R}{\partial\theta}\frac{\sin\theta}{h_\theta}\right\rangle}{\left\langle\frac{\sin^2\theta}{h_\theta}\right\rangle}\left\langle\frac{\cos^2\theta}{h_\theta}\right\rangle\right)+qrf_p\hat{V}_{\phi i}\tilde{V}_{\phi i}^s\left\langle\frac{1}{R}\frac{\partial R}{\partial\theta}\frac{\sin\theta}{h_\theta}\right\rangle-f_p\left(\bar{\nu}^{*}_{iI}+\bar{\nu}^{*}_{ie}\right)-f_p\nu^{*}_{atomi}$$

$$-q^2R_0{}^2f_if_p\left[\begin{array}{l}\left[\frac{1}{3}\tilde{n}_i^c+\alpha_i^{3C}\right]\varepsilon\left\langle\frac{\partial h_\theta}{\partial\theta}\frac{\sin\theta}{(h_\theta)^3}\right\rangle-\left[\tilde{n}_i^c+2\alpha_i^{3C}\right]\varepsilon\left\langle\frac{1}{R}\frac{\partial R}{\partial\theta}\frac{\sin\theta}{(h_\theta)^2}\right\rangle-\left[\tilde{n}_i^c+\alpha_i^{3C}\right]\frac{1}{3}\varepsilon\left\langle\frac{\cos\theta}{(h_\theta)^2}\right\rangle\\ +3\langle Q\rangle+\langle M\rangle-\alpha_i^{3C}\varepsilon\langle N\cos\theta\rangle+\frac{\left\langle\frac{1}{R}\frac{\partial R}{\partial\theta}\sin\theta\frac{1}{h_\theta}\right\rangle}{\left\langle\frac{\sin^2\theta}{h_\theta}\right\rangle}\left[\begin{array}{l}-\frac{1}{3}\left\langle\frac{\partial h_\theta}{\partial\theta}\frac{\sin\theta}{(h_\theta)^3}\right\rangle+\left\langle\frac{1}{R}\frac{\partial R}{\partial\theta}\frac{\sin\theta}{(h_\theta)^2}\right\rangle+\frac{1}{3}\left\langle\frac{\cos\theta}{(h_\theta)^2}\right\rangle\\ +\langle M\cos\theta\rangle-\langle P\sin\theta\rangle\end{array}\right]\end{array}\right]$$

$$+q^2R_0{}^2f_if_p\varepsilon\frac{\left\langle\frac{1}{1+\varepsilon\cos\xi}\right\rangle}{\left\langle\frac{1}{h_r}\right\rangle}\alpha_i^{2C}\left[2\left\langle\frac{1}{R}\frac{\partial R}{\partial\theta}\frac{\sin\theta}{(h_\theta)^2}\right\rangle+\langle N\cos\theta\rangle-\left\langle\frac{\partial h_\theta}{\partial\theta}\frac{\sin\theta}{(h_\theta)^3}\right\rangle+\left\langle\frac{\cos\theta}{(h_\theta)^2}\right\rangle\right]$$

$$c_{12}=f_p\left(\bar{\nu}^{*}_{iI}+\bar{\nu}^{*}_{ie}\right)\sqrt{\frac{m_i}{m_I}}$$

$$
\begin{aligned}
d_1 = q^2 R_0{}^2 \hat{V}_{\phi i} f_i f_p \Bigg[& \tilde{n}_i^c \varepsilon \left(\left\langle \frac{1}{R}\frac{\partial R}{\partial \theta}\frac{\sin\theta}{(h_\theta)^2} \right\rangle - \langle N\cos\theta\rangle \right) - \langle N\rangle - 3\left\langle \left(\frac{1}{R}\frac{\partial R}{\partial\theta}\right)^2 \frac{1}{(h_\theta)^2} \right\rangle \\
& + \varepsilon \left[\alpha_i^{1C} - \left(1 + \frac{\partial R_0(r)}{\partial r}\right) \frac{\left\langle \frac{1}{(1+\varepsilon\cos\xi)}\frac{1}{h_r} \right\rangle}{\left\langle \frac{1}{h_r} \right\rangle} \alpha_i^{2C} - \frac{\hat{P}_i}{\hat{V}_{\phi i}} \left(\alpha_i^{2C} - \alpha_i^{4C} \right) \right] \times \\
& \left(-2\left\langle \frac{1}{R}\frac{\partial R}{\partial\theta}\frac{\sin\theta}{(h_\theta)^2} \right\rangle - \langle N\cos\theta\rangle + \left\langle \frac{\partial h_\theta}{\partial\theta}\frac{\sin\theta}{(h_\theta)^3} \right\rangle - \left\langle \frac{\cos\theta}{(h_\theta)^2} \right\rangle \right) \Bigg] \\
& + \frac{1}{2} q r \tilde{n}_i^s \left\langle \frac{\cos\theta}{h_\theta} \right\rangle - \langle M_{\theta i}\rangle \frac{qR_0}{n_i m_i V_{thi}^2} + \hat{V}_{ri} \left\langle \frac{1}{(1+\varepsilon\cos\xi)} \right\rangle \\
& + \frac{1}{2} q R_0 \overline{\overline{\Phi}}_i \varepsilon \left(\tilde{\Phi}^s \left[\left\langle \frac{\cos\theta}{h_\theta} \right\rangle + \varepsilon \tilde{n}_i^c \left\langle \frac{\cos^2\theta}{h_\theta} \right\rangle \right] - \varepsilon \tilde{n}_i^s \tilde{\Phi}^c \left\langle \frac{\sin^2\theta}{h_\theta} \right\rangle \right)
\end{aligned}
\tag{D5}
$$

$$
c_{21} = f_p \left(\overline{\nu}_{Ii}^* + \overline{\nu}_{Ie}^* \right) \sqrt{\frac{m_I}{m_i}}
$$

$$
c_{22} = \hat{V}_{\theta I}^{n-1} q r f_p^2 \tilde{n}_I^s \left(\left\langle \frac{\cos\theta}{h_\theta} \right\rangle + \frac{\left\langle \frac{1}{R}\frac{\partial R}{\partial\theta}\frac{\sin\theta}{h_\theta} \right\rangle}{\left\langle \frac{\sin^2\theta}{h_\theta} \right\rangle} \left\langle \frac{\cos^2\theta}{h_\theta} \right\rangle \right) + q r f_p \hat{V}_{\phi I} \tilde{V}_{\phi I}^s \left\langle \frac{1}{R}\frac{\partial R}{\partial\theta}\frac{\sin\theta}{h_\theta} \right\rangle - f_p \left(\overline{\nu}_{Ii}^* + \overline{\nu}_{Ie}^* \right) - f_p \nu_{atomI}^*
$$

$$
\begin{aligned}
-q^2 R_0{}^2 f_I f_p \Bigg[& \left[\frac{1}{3}\tilde{n}_I^c + \alpha_I^{3C} \right] \varepsilon \left\langle \frac{\partial h_\theta}{\partial\theta}\frac{\sin\theta}{(h_\theta)^3} \right\rangle - \left[\tilde{n}_I^c + 2\alpha_I^{3C} \right] \varepsilon \left\langle \frac{1}{R}\frac{\partial R}{\partial\theta}\frac{\sin\theta}{(h_\theta)^2} \right\rangle - \left[\tilde{n}_I^c + \alpha_I^{3C} \right] \frac{1}{3}\varepsilon \left\langle \frac{\cos\theta}{(h_\theta)^2} \right\rangle \\
& + 3\langle Q\rangle + \langle M\rangle - \alpha_I^{3C} \varepsilon \langle N\cos\theta\rangle \\
& + \frac{\left\langle \frac{1}{R}\frac{\partial R}{\partial\theta}\sin\theta\frac{1}{h_\theta} \right\rangle}{\left\langle \frac{\sin^2\theta}{h_\theta} \right\rangle} \left[-\frac{1}{3}\left\langle \frac{\partial h_\theta}{\partial\theta}\frac{\sin\theta}{(h_\theta)^3} \right\rangle + \left\langle \frac{1}{R}\frac{\partial R}{\partial\theta}\frac{\sin\theta}{(h_\theta)^2} \right\rangle + \frac{1}{3}\left\langle \frac{\cos\theta}{(h_\theta)^2} \right\rangle + \langle M\cos\theta\rangle - \langle P\sin\theta\rangle \right] \Bigg] \\
+ q^2 R_0{}^2 f_I f_p \varepsilon & \frac{\left\langle \frac{1}{1+\varepsilon\cos\xi} \right\rangle}{\left\langle \frac{1}{h_r} \right\rangle} \alpha_I^{2C} \left[2\left\langle \frac{1}{R}\frac{\partial R}{\partial\theta}\frac{\sin\theta}{(h_\theta)^2} \right\rangle + \langle N\cos\theta\rangle - \left\langle \frac{\partial h_\theta}{\partial\theta}\frac{\sin\theta}{(h_\theta)^3} \right\rangle + \left\langle \frac{\cos\theta}{(h_\theta)^2} \right\rangle \right]
\end{aligned}
\tag{D6}
$$

D3. Coefficients in the toroidal rotation subsystem:

$$
e_{11} = \sqrt{\frac{m_I}{m_i}}\beta_i, \qquad e_{12} = \beta_I, \qquad f_1 = \frac{y_i + y_I}{V_{thI}}
\tag{D7}
$$

$$e_{21} = 1, \qquad e_{22} = -\sqrt{\frac{m_i}{m_I}}$$

$$f_2 = \left[\hat{V}_{\theta i} - \sqrt{\frac{m_i}{m_I}} \hat{V}_{\theta I} \right] \frac{\left\langle \dfrac{1}{1+\varepsilon\cos\xi} \right\rangle}{\left(1 + \dfrac{\partial R_0(r)}{\partial r} \right) \left\langle \dfrac{1}{(1+\varepsilon\cos\xi)} \dfrac{1}{h_r} \right\rangle} \tag{D8}$$

$$+ \left[-\hat{P}_i + \sqrt{\frac{m_i}{m_I}} \hat{P}_I \right] \frac{\left\langle \dfrac{1}{h_r} \right\rangle}{\left(1 + \dfrac{\partial R_0(r)}{\partial r} \right) \left\langle \dfrac{1}{(1+\varepsilon\cos\xi)} \dfrac{1}{h_r} \right\rangle}$$

APPENDIX E

GTROTA (Georgia Tech ROTAtion) USER'S MANUAL

GTROTA(Georgia Tech ROTAtion) version 1.0 User's Manual

Cheonho Bae[1]

Fusion Research Center & NRE Program, Georgia Institute of Technology

Atlanta, GA 30332-0425 USA

July 2012

---

[1] Electronic mail: gth892k@mail.gatech.edu

1. INTRODUCTION

GTROTA is a code that computes the plasma rotation velocities and the related momentum transport based on the neoclassical plasma rotation theory with the Stacy-Sigmar poloidal rotation model using the Miller equilibrium flux surface geometry [1]. Current rotation theory is based on Braginskii's ordering, thus the code is better suited for strong rotation analysis although it would still run for slow rotation analysis with decreased accuracy. This manual introduces the basic physics and numerical calculation model, how to create an input subroutine, how to run the code, and how to process the outputs. Details on the plasma rotation theory can be found in Ref. [1] and the numerical analysis methodology is discussed in Ref. [2]. Users of this code are highly recommended to read these before using the code. GTROTAv1.0 is currently provided in Matlab and will be converted into Fortran in the near future.

2. PHYSICS MODEL

2.1. Extended plasma rotation theory

The extended neoclassical plasma rotation theory and its calculation model [1] is derived from the continuity,

$$\frac{\partial n_j}{\partial t} + \nabla \cdot (n_j \vec{V}_j) = S_j^{\,o} \tag{1}$$

and the momentum balance equations,

$$m_j \frac{\partial}{\partial t}(n_j \vec{V}_j) + n_j m_j \nabla \cdot \left(\vec{V}_j \vec{V}_j\right) + \nabla P_j + \nabla \cdot \vec{\vec{\Pi}}_j = n_j e_j (\vec{E} + \vec{V}_j \times \vec{B}) + \vec{F}_j^{\,1} + \vec{S}_j^{\,1} \tag{2}$$

where S is the source, P is the pressure, $\vec{\vec{\Pi}}$ is the viscosity tensor, and F is the collisional friction. The primary goal of the tokamak plasma rotation theory is to predict toroidal velocity of the main ion (deuterium), whose measurement is not available, and

calculate the associated momentum transport. The non-negligent poloidal and toroidal components of the inertial term in Eq. (2) are

$$\left[\left(\vec{V}\bullet\nabla\right)\vec{V}\right]_\theta = \frac{V_{\theta j}}{h_\theta}\frac{\partial V_{\theta j}}{\partial\theta} - \frac{V_{\theta j}V_{\phi j}}{h_\theta h_\phi}\frac{\partial h_\phi}{\partial\theta}, \tag{3}$$

$$\left[\left(\vec{V}\bullet\nabla\right)\vec{V}\right]_\phi = \left(\frac{V_{rj}}{h_r}\frac{\partial V_{\phi j}}{\partial r} + \frac{V_{\phi j}V_{rj}}{h_\phi h_r}\frac{\partial h_\phi}{\partial r}\right) + \left(\frac{V_{\theta j}}{h_\theta}\frac{\partial V_{\phi j}}{\partial\theta} + \frac{V_{\phi j}V_{\theta j}}{h_\phi h_\theta}\frac{\partial h_\phi}{\partial\theta}\right), \tag{4}$$

and those of the viscosity terms with respect to Braginskii's viscosity representations[3-6] are

$$\left(\nabla\bullet\Pi\right)_\theta = \frac{1}{H}\frac{\partial}{\partial r}\left(Rh_\theta\Pi_{r\theta}\right) + \frac{1}{H}\frac{\partial}{\partial\theta}\left(h_r h_\phi\Pi_{\theta\theta}\right) - \frac{1}{h_\theta h_r}\frac{\partial h_r}{\partial\theta}\Pi_{rr} + \frac{1}{h_\theta h_r}\frac{\partial h_\theta}{\partial r}\Pi_{\theta r} - \frac{1}{Rh_\theta}\frac{\partial R}{\partial\theta}\Pi_{\phi\phi}, \tag{5}$$

$$\left(\nabla\bullet\Pi\right)_\phi = \left[\frac{1}{Rh_\theta h_r}\frac{\partial}{\partial r}\left(Rh_\theta\Pi_{r\phi}\right) + \frac{1}{Rh_r}\frac{\partial R}{\partial r}\Pi_{r\phi}\right] + \left[\frac{B_\theta}{h_\theta}\frac{\partial}{\partial\theta}\left(\frac{\Pi_{\theta\phi}}{B_\theta}\right) + \frac{1}{Rh_\theta}\frac{\partial R}{\partial\theta}\Pi_{\theta\phi}\right]. \tag{6}$$

Braginskii's viscosity [6] is decomposed into the parallel (η_{0j}), perpendicular (η_{1j}, η_{2j}), and gyroviscous (η_{3j}, η_{4j}) contributions and their relative orderings are shown in Eq. (7) with η_{0j} represented with the Shaing banana-plateau-PS viscosity interpolation formula,[5]

$$\eta_{0j} = \frac{n_j m_j V_{thj} q R_0 \varepsilon^{-3/2}\nu_{jj}^*}{\left(1+\varepsilon^{-3/2}\nu_{jj}^*\right)\left(1+\nu_{jj}^*\right)} \equiv n_j m_j V_{thj} q R f_j,\ \eta_{1j} = \frac{3}{10}\frac{n_j T_j}{\Omega^2\tau},\ \eta_{2j} = 4\eta_{1j},\ \eta_{3j} = \frac{1}{2}\frac{n_j T_j}{\Omega},\ \eta_{4j} = 2\eta_{3j} \tag{7}$$

where V_{thj} is the thermal velocity of species j, q is the safety factor, $\nu = 1/\tau$ is the collision frequency with its normalized term $\nu^* \equiv \nu q R_0 / V_{th}$, Ω is the gyrofrequency, and $f_j \equiv \dfrac{\varepsilon^{-3/2}\nu_{jj}^*}{\left(1+\varepsilon^{-3/2}\nu_{jj}^*\right)\left(1+\nu_{jj}^*\right)}$.

Unlike earlier simple theories [7-9], this extended calculation model [1, 10] expands density and velocity with the lowest order Fourier Series,

$$n_j\left(r,\theta\right) \approx \bar{n}_j\left(r\right)\left[1 + n_j^c\cos\theta + n_j^s\sin\theta\right], \tag{8}$$

$$V_j(r,\theta) \approx \overline{V}_j(r)\left[1+V_j^c \cos\theta + V_j^s \sin\theta\right], \tag{9}$$

thus introduces poloidal asymmetries ($n_j^{c,s}$ and $V_j^{c,s}$) in the formalism. Earlier, Stacey et al.[10] have calculated these asymmetries assuming circular flux surface geometry, limiting the accuracy in the calculations. The calculation model presented in this manual [1] is based on a D-shaped elongated geometry given in the next section [11], thus calculates the asymmetries more accurately.

2.2. Magnetic flux surface geometry

The geometry of the D-shaped elongated magnetic flux surface used in the code is given by Miller et al. [11] with elongation κ and triangularity δ as shown in Fig. 1. The R and Z coordinates of the Miller model are given by

$$R(r) = R_0(r) + r\cos(\theta + x\sin\theta) \equiv R_0(r) + r\cos\xi, \tag{10}$$

$$Z(r) = \kappa r \sin\theta, \tag{11}$$

where $R_0(r)$ is a function of r (the half-diameter from the center of plasma along the plasma mid-plane), $x \equiv \sin^{-1}\delta$, and $\xi \equiv \theta + x\sin\theta$.

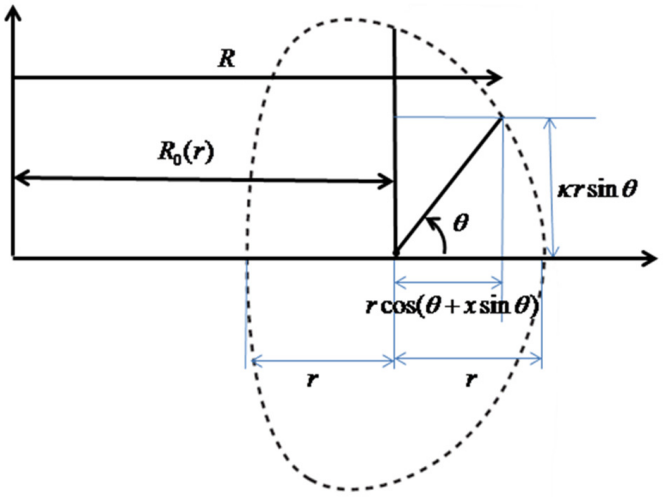

Fig. 1. Miller equilibrium flux surface geometry

Analysis of the curvilinear differential geometry in all coordinates (r,θ,ϕ) on the flux surfaces yields the following metric coefficients for the Miller geometry [11-13].

$$h_r = \frac{\kappa\left[\cos\left(x\sin\theta\right)+\frac{\partial R_0(r)}{\partial r}\cos\theta+\left[s_\kappa - s_\delta\cos\theta+\left(1+s_\kappa\right)x\cos\theta\right]\sin\theta\sin\xi\right]}{\sqrt{\sin^2\xi\left(1+x\cos\theta\right)^2+\kappa^2\cos^2\theta}}, \quad (12)$$

$$h_\theta = \frac{r\kappa\left[\cos\left(x\sin\theta\right)+\frac{\partial R_0(r)}{\partial r}\cos\theta+\left[s_\kappa - s_\delta\cos\theta+\left(1+s_\kappa\right)x\cos\theta\right]\sin\theta\sin\xi\right]}{\sqrt{\left(\frac{\partial R_0}{\partial r}+\cos\xi - s_\delta\sin\xi\sin\theta\right)^2+\kappa^2\sin^2\theta\left(s_\kappa+1\right)^2}}, \quad (13)$$

$$h_\phi = R(r) = R_0\left(1+\varepsilon\cos\xi\right) \quad (14)$$

where $s_\kappa\left(r\right)=\frac{r}{\kappa}\frac{\partial\kappa}{\partial r}$ and $s_\delta\left(r\right)=r\frac{\partial\delta}{\partial r}/\sqrt{\left(1-\delta^2\right)}$ account for the radial changes in elongation and triangularity. Ampere's law provides the following magnetic field representations for the Miller model,

$$B_\theta\left(r,\theta\right)=\left(1+\frac{\partial R_0(r)}{\partial r}\right)\frac{\overline{B}_\theta}{h_r\left(1+\varepsilon\cos\xi\right)}, \quad (15)$$

$$B_\phi = \frac{\overline{B}_\phi}{1+\varepsilon\cos\xi}, \quad (16)$$

where the overbars indicate the average values at given r, and the flux surface average (FSA) formula for this Miller geometry is given by

$$\left\langle A(r,\theta)\right\rangle \equiv \frac{\oint\frac{A(r,\theta)d\ell_\theta}{B_\theta}}{\oint\frac{d\ell_\theta}{B_\theta}} = \frac{\oint A(r,\theta)Y\left(r,\theta\right)d\theta}{\oint Y\left(r,\theta\right)d\theta} \quad (17)$$

where

$$Y\left(r,\theta\right)=\frac{\left(1+\varepsilon\cos\xi\right)\left[\cos\left(x\sin\theta\right)+\frac{\partial R_0(r)}{\partial r}\cos\theta+\left[s_\kappa - s_\delta\cos\theta+\left(1+s_\kappa\right)x\cos\theta\right]\sin\theta\sin\xi\right]^2}{\sqrt{\left[\left(\frac{\partial R_0}{\partial r}+\cos\xi - s_\delta\sin\xi\sin\theta\right)^2+\kappa^2\sin^2\theta\left(s_\kappa+1\right)^2\right]\left[\sin^2\xi\left(1+x\cos\theta\right)^2+\kappa^2\cos^2\theta\right]}}. \quad (18)$$

These FSAs cannot be reduced to simple analytic expressions, thus computed in a separate routine and imported into the main code.

3. NUMERICAL CALCULATION MODEL

3.1. Coupled set of nonlinear equations

The extended rotation calculation model [1] is consisted of 8 unknowns (4 velocities and 4 density asymmetries) when assuming two-species plasma with Eq. (19) summarizing all interchangeably used notations in the code, figures, and equations to follow. In the code, velocities and asymmetries are normalized to the same order of magnitude to minimize numerical round-off errors by $\hat{V}_{\theta j} \equiv \overline{V}_{\theta j} \big/ f_p V_{thj}$, $\hat{V}_{\phi j} \equiv \overline{V}_{\theta j} \big/ V_{thj}$, and $\tilde{n}_j^{c,s} \equiv n_j^{c,s} \big/ \varepsilon$ where $\varepsilon \equiv r \big/ R_0$.

$$\begin{aligned}
&\hat{V}_{\phi i} = \hat{V}_{\phi D} = \hat{V}_{tD} : \text{Toroidal Velocity (Deuterium)}, \quad \hat{V}_{\phi I} = \hat{V}_{\phi C} = \hat{V}_{tC} : \text{Toroidal Velocity (Carbon)} \\
&\hat{V}_{\theta i} = \hat{V}_{\theta D} = \hat{V}_{pD} : \text{Poloidal Velocity (Deuterium)}, \quad \hat{V}_{\theta I} = \hat{V}_{\theta C} = \hat{V}_{pC} : \text{Poloidal Velocity (Carbon)} \\
&\tilde{n}_D^c = \tilde{n}_i^c : \text{Cos Asymmetry (Deuterium)}, \quad \tilde{n}_C^c = \tilde{n}_I^c : \text{Cos Asymmetry (Carbon)} \\
&\tilde{n}_D^s = \tilde{n}_i^s : \text{Sin Asymmetry (Deuterium)}, \quad \tilde{n}_C^s = \tilde{n}_I^s : \text{Sin Asymmetry (Carbon)}
\end{aligned} \tag{19}$$

Equations (20) to (24) constitute the eight equations, expressed in generic forms, to solve for the eight unknowns, with Eqs. (20) to (22) constituting six equations with j being either i (deuterium) or I (carbon) and k being the other.

$$A_{11}\hat{V}_{\theta j}^{\,2} + A_{12}\hat{V}_{\theta j} + A_{13}\hat{V}_{\theta k} = B_1 \tag{20}$$

$$A_{C1}\tilde{n}_j^c + A_{C2}\tilde{n}_j^s + A_{C3}\tilde{n}_k^c = B_C \tag{21}$$

$$A_{S1}\tilde{n}_j^c + A_{S2}\tilde{n}_j^s + A_{S3}\tilde{n}_k^s = B_S \tag{22}$$

where A_{11}, A_{12}, A_{13}, $A_{C,S}$, B_1, and $B_{C,S}$ coefficients can be found in Ref. [2]. Equations (20) to (22) are the FSAs of Fourier moments of the poloidal momentum balance with all the terms retained, thus used to solve for the poloidal velocities and density asymmetries that are eventually coupled with toroidal rotation computation model, Eqs. (23) and (24).

$$\hat{V}_{\phi i}\sqrt{m_I/m_i}\,\beta_i + \hat{V}_{\phi I}\beta_I = \left(y_i + y_I\right)/V_{thI} \tag{23}$$

where

$$\beta_j \equiv \frac{\nu_{dj}+\nu_{nj}+S_{nbj}/\bar{n}_j}{\left(\bar{\nu}_{jk}+\bar{\nu}_{je}\right)} = qR_0\frac{\nu_{dj}+\nu_{nj}+S_{nbj}/\bar{n}_j}{\left(\bar{\nu}^*_{jk}+\bar{\nu}^*_{je}\right)V_{thj}} \text{ and } y_j = V_{thj}\left[\left(1+\beta_j\right)\hat{V}_{\phi j}-\sqrt{\frac{m_j}{m_k}}\hat{V}_{\phi k}\right]$$

with ν_{nj} and ν_{dj} being the "inertial" and "viscous" transport frequencies respectively, and S_{nb} being neutral beam source, and

$$\hat{V}_{\phi i}-\sqrt{\frac{m_i}{m_I}}\hat{V}_{\phi I}=\left(\hat{V}_{\theta i}-\sqrt{\frac{m_i}{m_I}}\hat{V}_{\theta I}\right)\frac{\left\langle\frac{1}{1+\varepsilon\cos\xi}\right\rangle}{\left(1+\frac{\partial R_0(r)}{\partial r}\right)\left\langle\frac{1}{(1+\varepsilon\cos\xi)}\frac{1}{h_r}\right\rangle}+\left(-\hat{P}_i+\sqrt{\frac{m_i}{m_I}}\hat{P}_I\right)\frac{\left\langle\frac{1}{h_r}\right\rangle}{\left(1+\frac{\partial R_0(r)}{\partial r}\right)\left\langle\frac{1}{(1+\varepsilon\cos\xi)}\frac{1}{h_r}\right\rangle} \quad (24)$$

constitute the toroidal rotation computation model derived from the toroidal and radial components of the momentum balance equation respectively. The quadratic equation in Eq. (20) is converted into Eq. (25) so that the quadratic term is treated as a linear term with n being the current iteration step and $n-1$ being the previous step. With the quadratic equation possibly having two solutions, this also ensures that the algorithm searches for the physical solution corresponding to the initial guesses of poloidal velocities.

$$A_{11}\hat{V}_{\theta j}{}^{n}\hat{V}_{\theta j}{}^{n-1}+A_{12}\hat{V}_{\theta j}{}^{n}+A_{13}\hat{V}_{\theta k}{}^{n}=B_1{}^{n} \quad (25)$$

More details on the derivation of these equations can be found in Ref. [1].

We notice that ν_{nj} and ν_{dj} given by,

$$\begin{aligned}\nu_{nj} &= \frac{\bar{V}_{rj}}{R_0}\left[\frac{\partial R_0}{\partial r}\left\langle\frac{1}{h_r}\right\rangle+\left\langle\frac{\cos\xi}{h_r}\right\rangle+\varepsilon\left(\tilde{\bar{n}}^c_j+\tilde{\bar{V}}^c_{\phi j}\right)\left\langle\cos\theta\frac{\cos\xi}{h_r}\right\rangle-R_0L^{-1}_{\bar{V}_\phi}\right]\\ &+\bar{V}_{\theta j}\varepsilon\tilde{\bar{V}}^s_{\phi j}\left(\left\langle\cos\theta\frac{1}{h_\theta}\right\rangle+\frac{\left\langle\frac{1}{R}\frac{\partial R}{\partial\theta}\sin\theta\frac{1}{h_\theta}\right\rangle}{\left\langle\sin^2\theta\frac{1}{h_\theta}\right\rangle}\left\langle\cos^2\theta\frac{1}{h_\theta}\right\rangle+\varepsilon\left\langle\cos\theta\frac{\cos\xi}{h_\theta}\right\rangle+\frac{1}{R_0}\left\langle\frac{\partial R}{\partial\theta}\sin\theta\frac{1}{h_\theta}\right\rangle\right)\end{aligned} \quad (26)$$

where $L^{-1}_X = -1/X\,\partial X/\partial r$ is the gradient length scales for a given quantity X and $\tilde{\bar{V}}^{c,s}_{\phi j} \equiv \bar{V}^{c,s}_{\phi j}/\varepsilon$, and

$$\nu_{dj} \approx \nu^1_{dj}+\nu^2_{dj} \quad (27)$$

where

$$\nu_{dj}^{1} = -\frac{T_j}{R_0 e_j \overline{B}_\phi}\varepsilon\left[\begin{array}{l}\widetilde{V}_{\phi j}^{s}\left(2\left\langle\cos\theta\frac{\cos\xi}{h_\theta h_r}\right\rangle+\frac{1}{R_0}\left\langle R\cos\theta\frac{\cos\xi}{h_\theta h_r}\right\rangle+\frac{1}{R_0}\left\langle R\sin\theta\frac{\sin\xi}{h_\theta h_r}\right\rangle+\frac{1}{R_0}x\left\langle R\sin\theta\cos\theta\frac{\sin\xi}{h_\theta h_r}\right\rangle\right)\\ +\tilde{n}_j^{s}\frac{1}{R_0}\left(\left\langle R\sin\theta\frac{\sin\xi}{h_\theta h_r}\right\rangle+x\left\langle R\sin\theta\cos\theta\frac{\sin\xi}{h_\theta h_r}\right\rangle\right)\end{array}\right], \quad (28)$$

$$\nu_{dj}^{2} \equiv \frac{1}{2}\frac{\tilde{\theta}_j G_j T_j}{R_0^{\,2} e_j B_\phi} \quad (29)$$

with

$$G_j \equiv r\left(L_{n_j}^{-1}+L_{T_j}^{-1}+L_{\widetilde{V}_{\phi j}}^{-1}\right), \quad (30)$$

$$\tilde{\theta}_j = 2\varepsilon\left[\begin{array}{l}\widetilde{V}_{\phi j}^{s}\left(\tilde{n}_j^{c}\left\langle R\frac{\cos^2\theta}{h_\theta h_r}\right\rangle+\frac{1}{\varepsilon}\left\langle R\frac{\cos\theta}{h_\theta h_r}\right\rangle+\left\langle R\cos\theta\frac{\cos\xi}{h_\theta h_r}\right\rangle+\left\langle R\sin\theta\frac{\sin\xi}{h_\theta h_r}\right\rangle+x\left\langle R\sin\theta\cos\theta\frac{\sin\xi}{h_\theta h_r}\right\rangle\right)\\ +\tilde{n}_j^{s}\left(-\widetilde{V}_{\phi j}^{c}\left\langle R\frac{\sin^2\theta}{h_\theta h_r}\right\rangle+\left\langle R\sin\theta\frac{\sin\xi}{h_\theta h_r}\right\rangle+x\left\langle R\sin\theta\cos\theta\frac{\sin\xi}{h_\theta h_r}\right\rangle\right)\end{array}\right], \quad (31)$$

must be computed to calculate the velocities and asymmetries. These are the transport rate calculations due to inertial and gyroviscosity. Gyroviscous component essentially dominates the neoclassical viscous transport in tokamak plasmas and also much larger than the inertial transport [1].

3.2. Decomposed numerical calculation models

GTROTAv1.0 solves the following decomposed system of nonlinear equations.

Poloidal rotation subsystem: $$\begin{bmatrix} c_{11} & c_{12} \\ c_{21} & c_{22} \end{bmatrix}\begin{bmatrix} \hat{V}_{\theta i} \\ \hat{V}_{\theta I} \end{bmatrix} = \begin{bmatrix} d_1 \\ d_2 \end{bmatrix} \quad (32)$$

Density asymmetry subsystem: $$\begin{bmatrix} a_{11} & a_{12} & a_{13} & 0 \\ a_{21} & a_{22} & 0 & a_{24} \\ a_{31} & 0 & a_{33} & a_{34} \\ 0 & a_{42} & a_{43} & a_{44} \end{bmatrix}\begin{bmatrix} \tilde{n}_i^{c} \\ \tilde{n}_i^{s} \\ \tilde{n}_I^{c} \\ \tilde{n}_I^{s} \end{bmatrix} = \begin{bmatrix} b_1 \\ b_2 \\ b_3 \\ b_4 \end{bmatrix} \quad (33)$$

Toroidal rotation subsystem: $$\begin{bmatrix} e_{11} & e_{12} \\ e_{21} & e_{22} \end{bmatrix}\begin{bmatrix} \hat{V}_{\phi i} \\ \hat{V}_{\phi I} \end{bmatrix} = \begin{bmatrix} f_1 \\ f_2 \end{bmatrix} \quad (34)$$

GTROTAv1.0 uses nonlinear Successive OverRelaxation (SOR) to iteratively solve for the eight unknowns using the algorithm illustrated in Fig. 2.

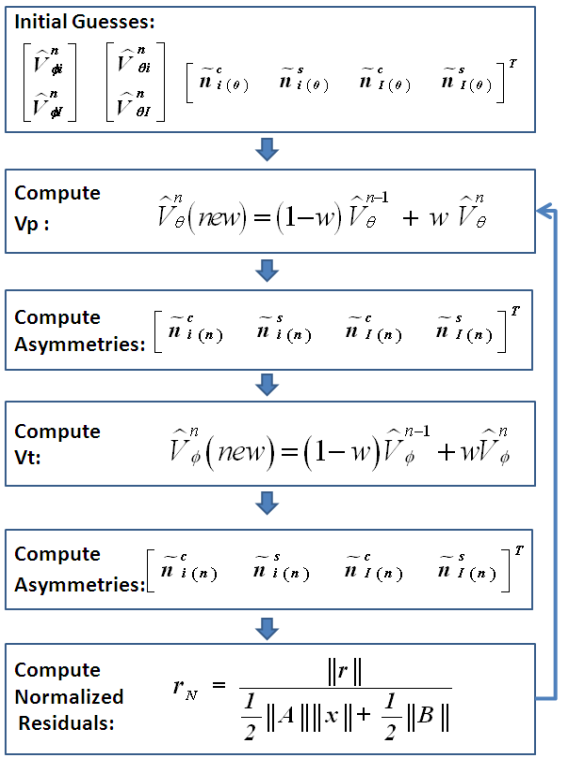

Fig. 2. SOR Flowsheet in the elongated model computation

GTROTAv1.0 uses the experimental measurement of carbon toroidal and poloidal velocities as the initial guesses for "VtI" and "VpI" respectively. It generates the initial guess for the deuterium toroidal velocity (Vti) from the perturbation theory using "VtI" as an input. The initial guess for the deuterium poloidal velocity (Vpi) is calculated from the momentum balance equation with three other initial guesses as the inputs. Zeros are used as the initial guesses for all the density asymmetries.

4. HOW TO RUN GTROTAv1.0

4.1. Step 1: How to create an input subroutine

To run the code, the first thing to do is create an input subroutine. The default input subroutine is "shot138639.m", shown in Table 1. If a user works on another shot, a new input file named "shot******.m" needs to be created.

Table 1. Input code (shot138639.m)

```
function
[Source_NB,Source_impurity,Source_wall,Elongation,dK_dr,x,a,Kmax,Kmin,del_top_max,del_bottom_max,dR0dr,VtI_one,VpI_one,shot,ne,R0,Bp,B
t,fp,E1,E2,E3,Etor,P_E1,P_E2,P_E3,f_E1_D1,f_E1_D2,f_E1_D3,f_E2_D1,f_E2_D2,f_E2_D3,f_E3_D1,f_E3_D2,f_E3_D3,q,nI,VtI,VpI,ni,Te,Ti,TI,T,
Torque_density,rho,r,ep,delta_r,Phi]=Shot138639(k,e,eV);

%############## SHOT 138639-2085 ms PARAMETERS from TRANSP###############
nc=textread('nc138639.txt');nI=nc(:,2).*1e19; rho=nc(:,1);%Carbon Density (m^-3);
Vt=textread('vt138639.txt');VtI=-Vt(:,2)*1000;%Toroidal Velocity(m/s)
Vp=textread('vp138639.txt');VpI=-Vp(:,2)*1000;%Poloidal Velocity(m/s)
Torque_read=textread('tq138639.txt');Torque_density=Torque_read(:,2);%Torque input(N.m)
ne=textread('ne138639.txt');ne=ne(:,2).*1e19;%Electron Density(m^-3)
te=textread('te138639.txt');Te=te(:,2)*1000; %Electron Temperature (eV)
Ti=textread('ti138639.txt');TI=Ti(:,2)*1000;Ti=TI;T=Ti;%Ion Temperature(eV);
vrpot=textread('vrpot138639.txt');Elec_poten=vrpot(:,2);%Electric potential(Volts);
Phi=vrpot(:,2);Phi(size((rho),1),1)=Phi(size((rho),1)-1,1);
Bt_profile=textread('bt138639.txt');Bt=-Bt_profile(1:2:101,2);%Toroidal magnetic strength(Tesla);
Bp_profile=textread('bp138639.txt');Bp=-Bp_profile(1:2:101,2);%Poloidal magnetic strength(Tesla);
sbtot=textread('sbtot138639.txt');Source_NB=sbtot(:,2);%Total Beam source(m^-3);
scimp=textread('scimp138639.txt');Source_impurity=scimp(:,2);%Impurity source(m^-3);
swtot=textread('swtot138639.txt');Source_wall=swtot(:,2);%Wall source(m^-3);
%############## SHOT 138639-2085 ms PARAMETERS from TRANSP###############

%############## BEAM INJECTION PARAMETERS(from EXPERIMENT) ###############
E1=81*1000; E2=75*1000; E3=81*1000;%Beam energies(eV)
P_E1=2.1;P_E2=2.2;P_E3=2.6;%Incident power(MW)
f_E1_D1=.55;f_E1_D2=.29;f_E1_D3=.16;%E1(81keV) power fraction(full, half, 1/3)
f_E2_D1=.54;f_E2_D2=.28;f_E2_D3=.18;%E1(75keV) power fraction(full, half, 1/3)
f_E3_D1=.55;f_E3_D2=.29;f_E3_D3=.16;%E1(81keV) power fraction(full, half, 1/3)
%############## BEAM INJECTION PARAMETERS(from EXPERIMENT) ###############

%############## PLASMA PARAMETERS from EFIT #################
Vloop=0.26296; % in Volts (must always be positive because Ip runs parallel with Vloop)
R0=1.734;
a=0.586;
q0=1.2;q95=4.9;qa=8;
Kmax=1.83;Kmin=1.45;
del_top_max=0.6;del_bottom_max=0.22;
beta_p=1.802; int_inductance=0.880;
```

```
%############## PLASMA PARAMETERS from EFIT ##################


%############## BASIC CALCULATIONS ##################
fp=Bp./Bt;
Etor=Vloop/(2*pi*R0);
ni=ne-6.*nI;% From Charge Neutrality
r=rho.*a;%
ep=r./R0;
delta_r=r(size((VtI),1))-r(size((VtI),1)-1);% Torque due to Neutral Beam (N*m/m^3);
dR0dr = -r./R0.*(beta_p + int_inductance/2);
R0_profile = R0+dR0dr.*delta_r;
radius=rho.*a;
del_top=(del_top_max-0)/a.*r;del_bottom=(del_bottom_max-0)/a.*r; % assume linear increase
x_top=asin(del_top);x_bottom=asin(del_bottom);
x=(x_top+x_bottom)./2;
Elongation=(Kmax-Kmin)/a*radius+1.45;
dK_dr=(Kmax-Kmin)/a; % assume linear increase of elongation
%############## PLASMA PARAMETERS from EFIT ##################


%############ PARAMETERS MANUALLY ADJUSTED to EFIT PROFILES ##############
q=40*r.^6+25*r.^4+q0; % manually fitted to profile in EFIT
%############ PARAMETERS MANUALLY ADJUSTED to EFIT PROFILES ##############
shot=138639; VtI_one = VtI; VpI_one=VpI;
return
```

Inputs in Table 1 are grouped together based on the input sources: TRANPS, EFIT, and experiment inputs. There are 13 inputs generated with TRANSP, with their units, summarized in Table 2. TRANSP generates profiles with 101 mesh points along the radial direction but GTROTAv1.0 uses 51 for saving the run-time, thus the input size needs to be adjusted so that the final outputs are in (51,1) column-vector format. Inputs from EFIT are directly from EFITools on DIII-D database. For accuracy, q profile is manually adjusted to fit the q profile in EFIT, instead of just assuming a linear increase. Beam injection parameters need to be acquired from users' collaborating experimentalist. For shot#138639, three beams with their beam energies 81keV (30LT), 75keV (150LT), and 81keV (330LT) are injected with duty cycles 2.1/2.6MW, 2.2/2.2MW, and

2.6/2.6MW respectively. For 30LT beam, the full, half, and 1/3 power fractions are 0.55, 0.29, and 0.16 respectively.

Table 2. Inputs from TRASNP

inputs	Parameter name	unit
nc138639	Carbon(or impurity) density	$10^{-19} \cdot particles \cdot m^{-3}$
ne138639	Electron density	$10^{-19} \cdot particles \cdot m^{-3}$
te138639	Electron temperature	keV
ti138639	Ion temperature	keV
tq138639	Torque input	$N \cdot m$
vp138639	Carbon poloidal velocity	$km \cdot s^{-1}$
vt138639	Carbon toroidal velocity	$km \cdot s^{-1}$
vrpot138639	Electric potential	$Volts$
sbtot138639	Total beam sources	$10^{-19} \cdot particles \cdot m^{-3}$
scimp138639	Impurity source	$10^{-19} \cdot particles \cdot m^{-3}$
swtot138639	Wall source	$10^{-19} \cdot particles \cdot m^{-3}$
bp138639	Poloidal magnetic field profile	$Tesla$
bt138639	Toroidal magnetic field profile	$Tesla$

4.1.1. Sign convention in the input subroutine

Due to the importance of the initial guesses in nonlinear programming, it is important that users put the signs of the inputs correctly. The sign convention for GTROTAv1.0 inputs is based on the theoretical coordinates determined by the right hand

rule with the thumb direction corresponding to the toroidal current (I_ϕ) direction. An example of theoretical sign convention for shot #138639 is illustrated in Fig. 3. In this example, I_ϕ is in clockwise (CW) direction, thus with $+\hat{n}_\phi$ being CW positive, $+\hat{n}_\theta$ will the positive upward at the outer mid-plane by the right hand rule. Thus, if the torque input is provided with positive values, its sign must be reversed since the beams are injected CCW ($-\hat{n}_\phi$ direction). Also, for shot #138639, TRANSP inputs for B_ϕ and B_θ are provided as negative values for CCW positive and downward positive at the outer mid-plane respectively, thus their signs must also be reversed to agree with schematics in Fig. 3. Since all DIII-D experiments do not follow this theoretical sign convention and experimental sign conventions can differ, users are advised to draw the directions of all the inputs in a similar schematic as in Fig. 3 to get the final input signs correctly. Otherwise, the code will still run to use a global minimization technique known as Simulated Annealing (SA) to identify a wrong solution as the true solution.

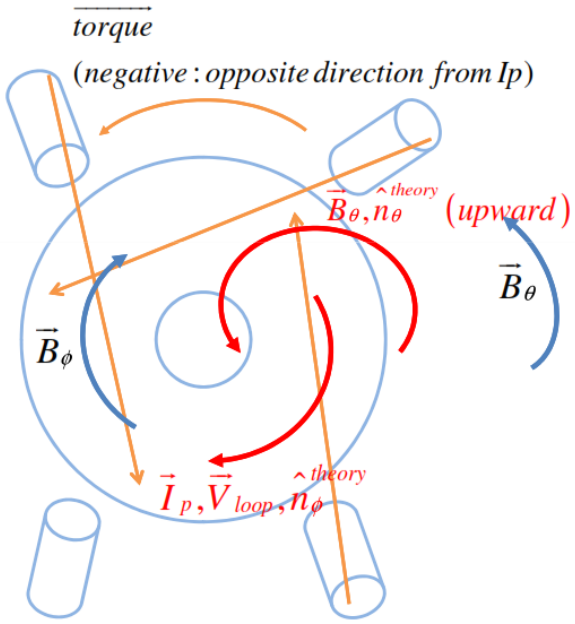

Figure 3. Theoretical sign convention for shot #138639

4.2. Step 2: Test run of the code

Once the input subroutine is created with correct signs, users need to update subroutine call command in the main program, GTROTA (see Table 3), as follows. Users can simply replace "138639" with user's own subroutine shot number (red color in Table 1). Leave "j_manual_138639.txt" as is for now because this needs to be updated after identifying the iteration step numbers that correspond to the true solution from this test run. Leave the default "relaxation(α)=0.5" as is because these will be explained later for users to adjust when necessary. "max_j=100" is the default number of maximum iterations, which is set enough for the code to generate at least three local minima in nonlinear topological maps, thus can later be adjusted especially with lower relaxation (α) values.

Table 3. Input subroutine call commands in the main code

[Elongation,dK_dr,x,a,Kmax,Kmin,del_top_max,del_bottom_max,dR0dr,VtI_one,VpI_one,shot,ne,R0,Bp,Bt,fp,E1,E2,E3,Etor,P_E1,P_E2,P_E3,f_E1_D1,f_E1_D2,f_E1_D3,f_E2_D1,f_E2_D2,f_E2_D3,f_E3_D1,f_E3_D2,f_E3_D3,q,nI,VtI,VpI,ni,Te,Ti,TI,T,Torque_density,rho,r,ep,delta_r,Phi]=Shot**138639**(k,e,eV);
sol_i=textread(**'j_manual_138639.txt'**);sol_iteration=sol_i(:,2);relaxation=**0.5**;max_j=**100**;

Now, GTROTAv1.0 is ready to test run the code for the shot of users' interest. In the Matlab command prompt, type "GTROTA" and hit enter. When the run is completed, GTROTAv1.0 will generate a number of figures including 51 nonlinear topological maps from the center mesh ($\rho = 0$) to the edge ($\rho = 1$). It uses nonlinear SOR to control the iterative dynamics of the velocity subsystems with each new velocities calculated by

$$\hat{V}^{n}(new) = (1-w)\,\hat{V}^{n-1} + w\,\hat{V}^{n} \tag{35}$$

where relaxation weight is computed by

$$w = \frac{\alpha}{cond(A)^{n=1}} \ . \tag{36}$$

The default α for the code ("relaxation" in Table 3) is $\alpha = 0.5$ and $cond\left(A\right)^{n=1}$ are the condition numbers of the poloidal and toroidal subsystem for 51 mesh points, thus automatically calculated by the code. Users can start with this default w to generate 51 topological maps and use SA to identify the true solution from these maps, or change α value once the nonlinear dynamics of the system for the new shot is well-understood. Nonlinear dynamics of each mesh is independent from other mesh dynamics but similarities exist for nearby meshes. Thus, SA can be used to identify the true solutions for all 51 maps that correspond to the global minima within the physically feasible range.

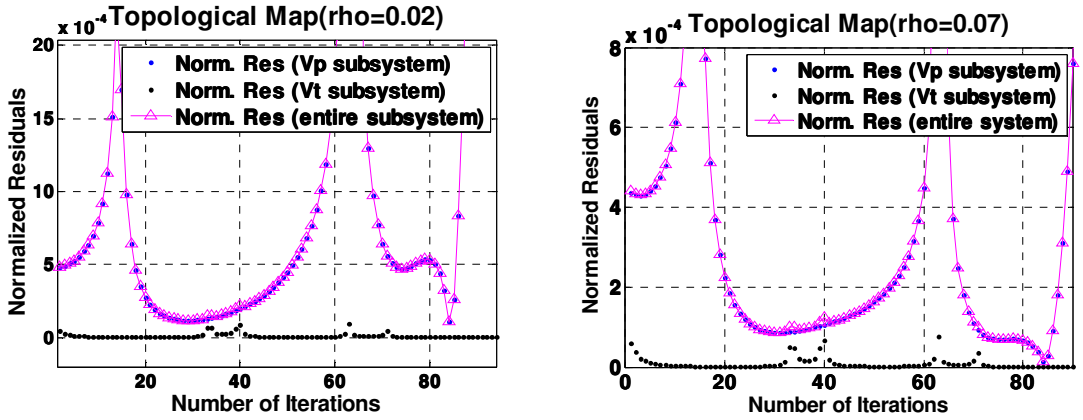

Figure 4. Topological maps for the meshes for $\rho < 0.25\,(\alpha = 0.5)$

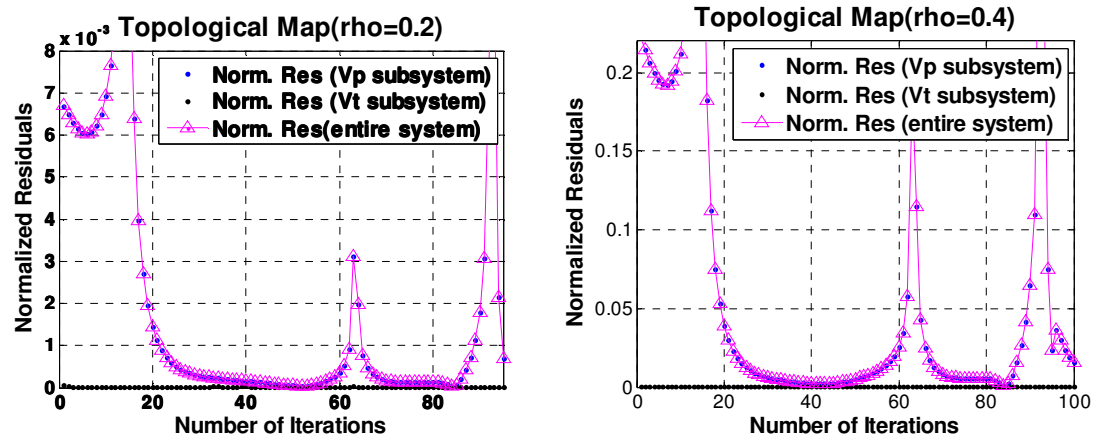

Figure 5. Topological maps for the meshes for $\rho > 0.25\,(\alpha = 0.5)$

For GTROTAv1.0, the physically feasible range is usually from zero velocities to approximately the triple of the initial guess, meaning that the algorithm assumes that the initial guesses at least have the same signs as the true solutions and this reemphasizes the importance of the accuracy of your initial guesses. Figures 4 and 5 present topological maps for four selected meshes along the radial profile for shot #138639 with $\alpha = 0.5$, which clearly shows 3~4 local minima before 100 iterations.

4.2.1. Application of Simulated Annealing

A test run of the code also generates three feasible solution sets, as shown in Fig. 6, that corresponds to the first three local minima near the initial guesses and users need to manually identify the true solution with SA. Shot #138639 is a good example to discuss the correct use of SA because it has a good mix of two different types of dynamics that users can expect from the code within $0.2 < \alpha < 2$. In Figure 6(a), Vpi for $\rho < 0.25$ quickly drives to the trivial solutions (i.e., zero velocities), yielding non-physical numerical blow-up on other velocities. Thus for $\rho < 0.25$ range, the first solution set (red squares) corresponds to the true solution. On the other hand, for $\rho > 0.25$ range, all three solutions are non-trivial solutions and SA identifies the 2nd solution set with the lowest normalized residulas as the true solution. Although the first set in $\rho > 0.25$ range is closer to the initial guesses, SA eliminates this set for its higher residuals by more than an order of magnitude compared to the 2nd (and 3rd) solution set. This means that the first set here only appeared as a transient solution that are not consistently generated with different α values. For an accurate identification of the true solution, users must understand two important facts: 1) solution for each mesh is independent; 2) trivial solutions must be identified and eliminated from the feasible solutions. Independence of each mesh implies that all 51 topological maps must be examined individually to determine the true solution by SA. Considering that the nearby

meshes yield similar dynamics, this is not a difficult task. Trivial solution sets are characterized by one(or multiple) velocity being almost zero while the others are numerically blown-up, yielding non-physical solutions. For shot #138639, α values other than 0.5 actually yield profiles that does not require separate selection about any discontinuous points but $\alpha = 0.5$ is set as default because overall it yields the most stable radial profiles. This type of differences in dynamics about a singular mesh is not rare, thus a careful tuning of the dynamics can be acheived by varying α to a wider range to identify the most optimal value, which is actually recommended for this code.

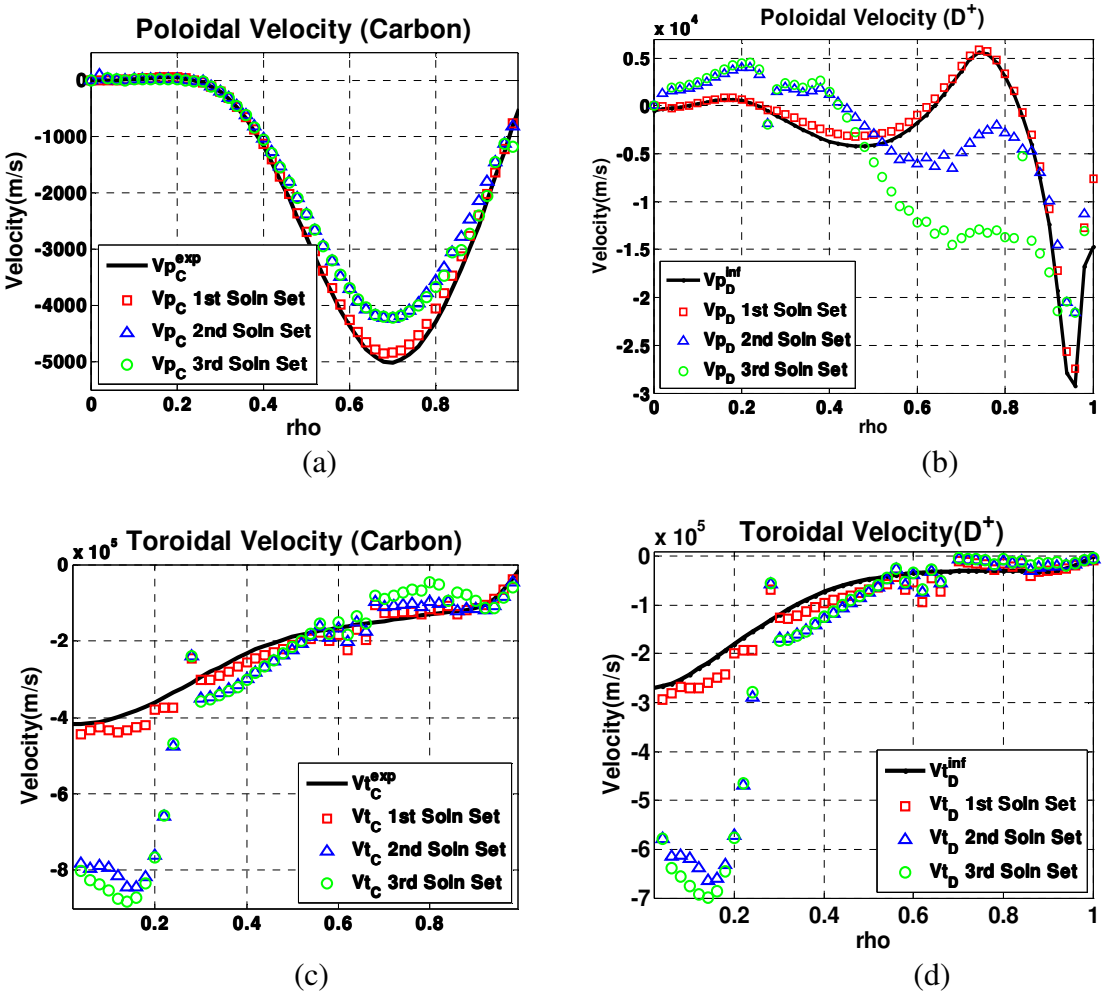

Figure 6. Feasible solution sets for the local minima in Figs. 4 and 5 (toroidal velocities: CW positive / poloidal velocities: positive upward at outer mid-plane)

4.3. Step 3: How to create the iteration step input for true solutions.

Once the code is test-run and users identify the iteration step for each individual mesh that corresponds to the true solution, next step is to create a text format input file that replace "j_manual_138639.txt" in the main program (Table 3). Typing either "har1_i", har2_i", or "har3_i" in the Matlab command prompt gives the corresponding iteration step numbers, j. Easiest way to create "j_manual_******.txt" is to copy and paste the iteration numbers into the Excel spreadsheet (j_manual_138639.xlsx) and save it as ".txt" format with a new shot number. In "j_manual_138639.txt", users can notice that the iteration step numbers for the meshes with high singularities are set as "NaN" so that the code will eliminate the discontinuities in the final profile. These points can be easily identified just by observing the profiles in Fig. 6 or refering to the condition number plot shown in Fig. 7. Users are also advised to neglect a few meshes at both ends of the profiles. Meshes for $\rho \le 0.3$ usually have very low accuracy because $\varepsilon \equiv r/R_0$ is too small, causing numerical blow-ups. Also, the results in $\rho > 0.95$ are less trustworthy not only because the numerical systems are extremely ill-conditioned but also because the current plasma rotation theory [1] based on Braginskii's ordering with no atomic physics treatment in the plasma edge lacks accuracy in the plasma edge and for slow rotation

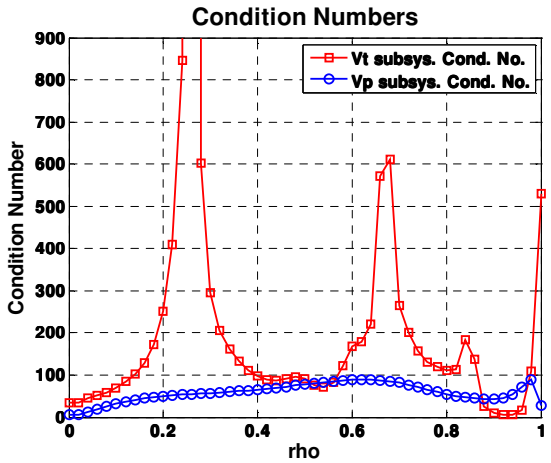

Figure 7. Condition numbers at initial iteration step(shot #138639)

shots. This manual process is expected to be automated in the future versions after analyzing more shots.

4.4. Step 4: Second run and the final processing

With "j_manual_******.txt" created, users need to run the code for the 2nd time. This second run will generate figures similar to those of shot #138639 in Fig. 8, showing the raw solutions (red squares) and the spline-fit (black dots) of the profiles together. Here $Vp_C^{\exp}$ and $Vt_C^{\exp}$ are the experimental measurement for carbon, $Vt_D^{\inf}$ is the inferred velocities from the perturbation theory, $Vp_D^{initial}$ is the initial guess calculated with the other velocities from the momentum balance equation.

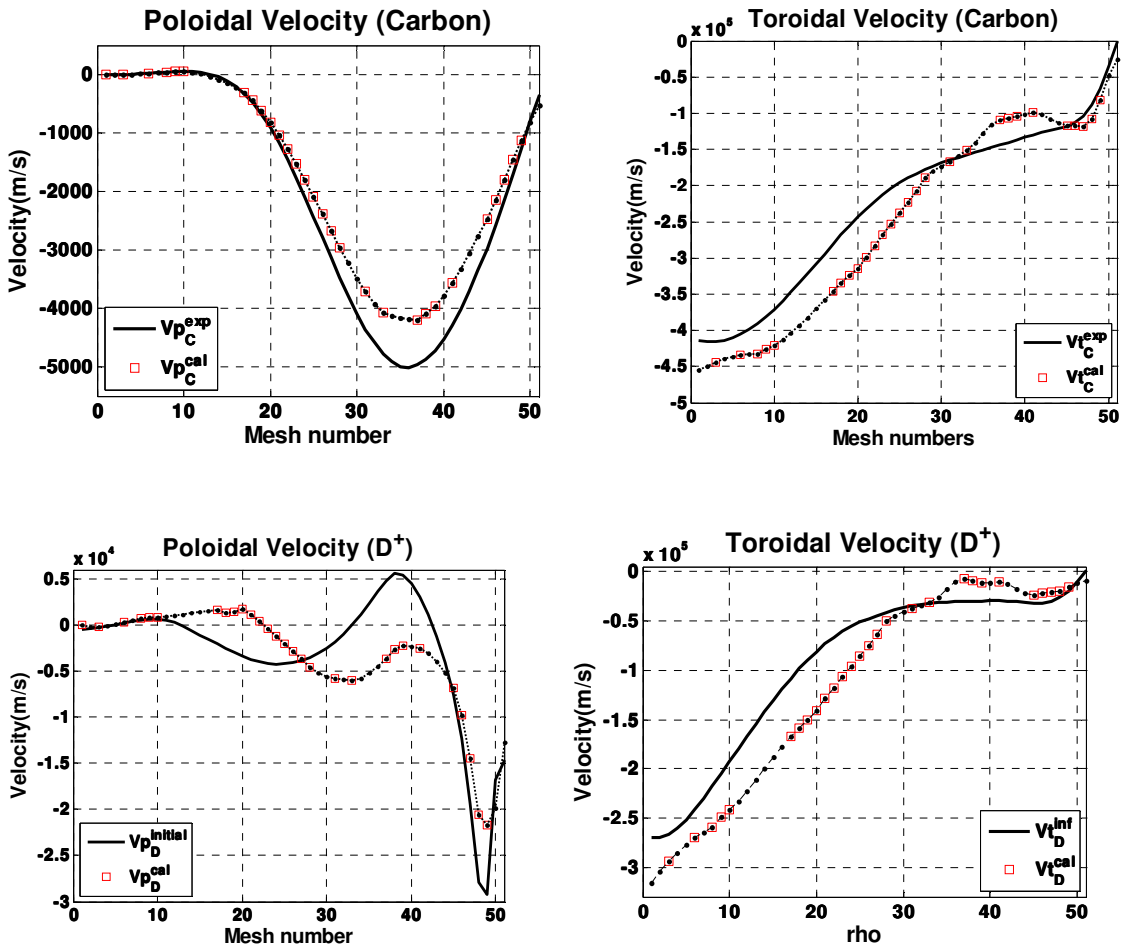

Figure 8. Raw velocities and spline-fitted profiles

Figures 9 show the finally processed profiles of the true solution (*Vp* and *Vt* of both species on the same plot) for shot #138639. Note that the signs of toroidal velocities are reversed from Fig. 8 due to the familiarity of the plasma physicists to CCW being positive.

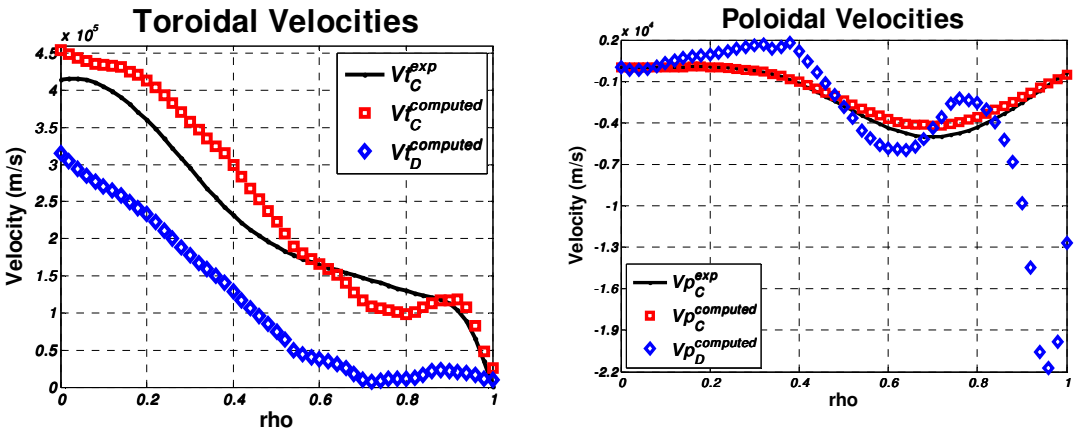

Figure 9. Final true solution velocity profiles (toroidal velocities: CCW positive / poloidal velocities: positive upward at outer mid-plane)

Figure 10 shows the finally spline-fitted density asymmetries for shot #138639. Here meshes for $\rho > 0.96$ not presented due to the lack of accuracy in this region.

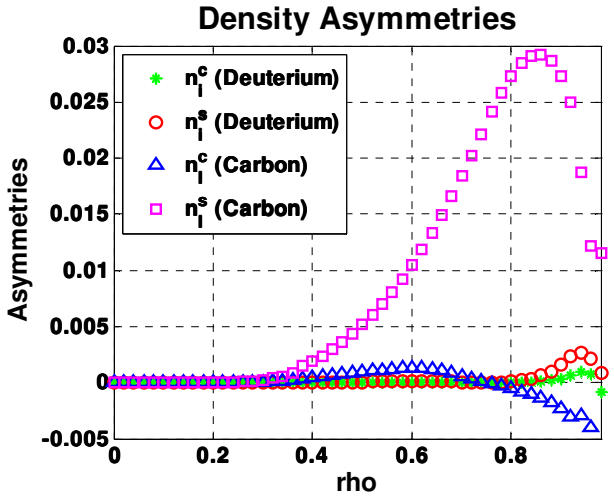

Figure 10. Computed density asymmetries

The code also calculates the neoclassical angular transport rates, inertial and gyroviscous transports, as shown in Fig. 11 for shot #138639. Note that GTROTAv1.0 based on the Stacey-Sigmar poloidal rotation model [1] calculates the gyroviscous transport contribution (not the much smaller perpendicular contribution) which accounts for the most of the neoclassical viscous damping. Neoclassical transport frequencies in the range $\rho > 0.9$ tend to fluctuate more as the code tries to spline fit them. With the current theory [1] not developed for slow rotation and not accounting for the atomic physics in the edge, when combined with the ill-conditioning of the numerical model in the edge, spline-fitted results in the plasma edge is not only less trustworthy but also can be misleading in terms of what's really happening in the edge. Future extended theory and the code will be updated to increase the accuracy in this range.

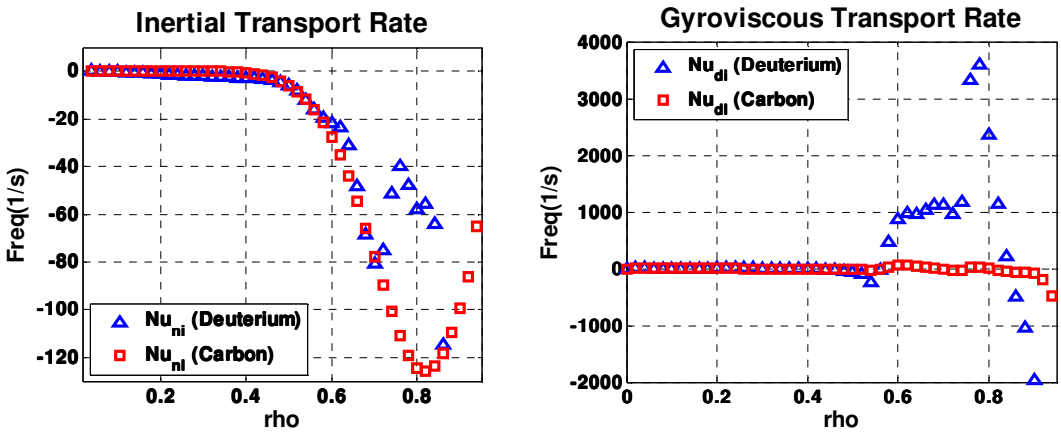

(a) Inertial transport frequency (b) Gyroviscous transport frequency

Figure 11. Transport frequencies

5. VERIFICATION OF RESULTS

GTROTAv1.0 allows users to examine the nonlinear dynamics of the given problem by changing the relaxation weights (i.e., changing α) in Eq. (36). Users are recommended to examine them for $0.2 \le \alpha \le 2$, or beyond if necessary, with the goal of identifying the most commonly appearing solution which corresponds to the true solution

that the algorithm always tries to converge to. Any solution profiles appearing for a particular α value only are likely to be transient solutions that happen to appear with higher normalized residuals (much higher than 10^{-3} empirically), thus not the true solution. Once the true solution is identified, users can change the default α to another optimal value that yields most stable true solution profile and process the solution manually for the final spline-fitted true solution profiles.

6. CONCLUSIONS

This manual for GTROTAv1.0 summarizes the neoclassical rotation theory and the numerical model of GTROTA, and the steps to follow for the users of the code. Use of Matlab during the development of the code allowed easy and fast testing of many standard and non-standard nonlinear algorithms discussed in Ref. [2]. It is expected to be translated into Fortran in the near future. Due to the inherent nonlinear characteristics of the extended plasma rotation theory, some manual steps in the use of the code was inevitable but will be automated as much as possible after identifying more generalized dynamics in the future versions. Users are encouraged to contact Cheonho Bae for any questions and suggestions regarding the algorithm of GTROTAv1.0.

References

1. C. Bae, Stacey, Weston M., Solomon, Wayne M., Physics of Plasma Physics (Unpublished results).
2. C. Bae, Stacey, Weston M., Morley, Tom D., J Comput Phys (Unpublished results).
3. W. M. Stacey, and D. J. Sigmar, Physics of Fluids **28** (1985).
4. W. M. Stacey, and C. Bae, Physics of Plasmas **16** (2009).
5. W. M. Stacey, *Fusion plasma physics* (Wiley-VCH ; John Wiley, Weinheim Chichester, 2005).
6. S. I. Braginskii, Review of Plasma Physics **1** (1965).
7. S. P. Hirshman, and D. J. Sigmar, Nuclear Fusion **21** (1981).
8. W. A. Houlberg *et al.*, Physics of Plasmas **4** (1997).
9. Y. B. Kim, P. H. Diamond, and R. J. Groebner, Phys Fluids B-Plasma **3** (1991).
10. W. M. Stacey, R. W. Johnson, and J. Mandrekas, Physics of Plasmas **13** (2006).
11. R. L. Miller *et al.*, Physics of Plasmas **5** (1998).
12. J. Candy, Plasma Physics and Controlled Fusion **51** (2009).
13. W. M. Stacey, Physics of Plasmas **15** (2008).

REFERENCES

[1] W.M. Stacey, A.W. Bailey, D.J. Sigmar, K.C. Shaing, Rotation and Impurity Transport in a Tokamak Plasma with Directed Neutral-Beam Injection, Nuclear Fusion, 25 (1985) 463-477.

[2] K.H. Burrell, T. Ohkawa, S.K. Wong, Explanation of the Expulsion of Impurities from Tokamak Plasmas by Neutral-Beam Injection, Physical Review Letters, 47 (1981) 511-515.

[3] A. Bondeson, D.J. Ward, Stabilization of External-Modes in Tokamaks by Resistive Walls and Plasma Rotation, Physical Review Letters, 72 (1994) 2709-2712.

[4] A.M. Garofalo, M.S. Chu, E.D. Fredrickson, M. Gryaznevich, T.H. Jensen, L.C. Johnson, R.J. La Haye, G.A. Navratil, M. Okabayashi, J.T. Scoville, E.J. Strait, A.D. Turnbull, D.-D. Team, Resistive wall mode dynamics and active feedback control in DIII-D, Nuclear Fusion, 41 (2001) 1171-1176.

[5] K.H. Burrell, Effects of ExB velocity shear and magnetic shear on turbulence and transport in magnetic confinement devices, Physics of Plasmas, 4 (1997) 1499-1518.

[6] J.S. deGrassie, D.R. Baker, K.H. Burrell, P. Gohil, C.M. Greenfield, R.J. Groebner, D.M. Thomas, Toroidal rotation in neutral beam heated discharges in DIII-D, Nuclear Fusion, 43 (2003) 142-156.

[7] K.D. Zastrow, W.G.F. Core, L.G. Eriksson, M.G. Von Hellermann, A.C. Howman, R.W.T. Konig, Transfer rates of toroidal angular momentum during neutral beam injection, Nuclear Fusion, 38 (1998) 257-263.

[8] S.D. Scott, V. Arunasalam, C.W. Barnes, M.G. Bell, M. Bitter, R. Boivin, N.L. Bretz, R. Budny, C.E. Bush, A. Cavallo, T.K. Chu, S.A. Cohen, P. Colestock, S.L. Davis, D.L. Dimock, H.F. Dylla, P.C. Efthimion, A.B. Erhrardt, R.J. Fonck, E. Fredrickson, H.P. Furth, R.J. Goldston, G. Greene, B. Grek, L.R. Grisham, G. Hammett, R.J. Hawryluk, H.W. Hendel, K.W. Hill, E. Hinnov, D.J. Hoffman, J. Hosea, R.B. Howell, H. Hsuan, R.A. Hulse, K.P. Jaehnig, A.C. Janos, D. Jassby, F. Jobes, D.W. Johnson, L.C. Johnson, R. Kaita, C. Kierasphillips, S.J. Kilpatrick, P.H. Lamarche, B. Leblanc, R. Little, D.M. Manos, D.K. Mansfield, E. Mazzucato, M.P. Mccarthy, D.C. Mccune, K. Mcguire, D.H. Mcneill, D.M. Meade, S.S. Medley, D.R. Mikkelsen, R. Motley, D. Mueller, J.A. Murphy, Y. Nagayama, R. Nazakian, D.K. Owens, H. Park, A.T. Ramsey, M.H. Redi, A.L. Roquemore, P.H. Rutherford, G. Schilling, J. Schivell, G.L. Schmidt, J. Stevens, B.C. Stratton, W. Stodiek, E.J. Synakowski, W.M. Tang, G. Taylor, J.R. Timberlake, H.H. Towner, M. Ulrickson, S. Vongoeler, R. Wieland, M. Williams, J.R. Wilson, K.L. Wong, S. Yoshikawa, K.M. Young, M.C. Zarnstorff, S.J. Zweben, Correlations of Heat and Momentum Transport in the Tftr Tokamak, Physics of Fluids B-Plasma Physics, 2 (1990) 1300-1305.

[9] S. Suckewer, H.P. Eubank, R.J. Goldston, E. Hinnov, N.R. Sauthoff, Toroidal Plasma Rotation in the Princeton Large Torus Induced by Neutral-Beam Injection, Physical Review Letters, 43 (1979) 207-210.

[10] R.C. Isler, L.E. Murray, E.C. Crume, C.E. Bush, J.L. Dunlap, P.H. Edmonds, S. Kasai, E.A. Lazarus, M. Murakami, G.H. Neilson, V.K. Pare, S.D. Scott, C.E. Thomas, A.J. Wootton, Impurity Transport and Plasma Rotation in the Isx-B Tokamak, Nuclear Fusion, 23 (1983) 1017-1037.

[11] R.J. Groebner, W. Pfeiffer, F.P. Blau, K.H. Burrell, E.S. Fairbanks, R.P. Seraydarian, H. Stjohn, R.E. Stockdale, Experimentally Inferred Ion Thermal-Diffusivity Profiles in the Doublet-Iii Tokamak - Comparison with Neoclassical Theory, Nuclear Fusion, 26 (1986) 543-554.
[12] A.N. Kaufman, Plasma Viscosity in a Magnetic Field, Physics of Fluids, 3 (1960) 610-616.
[13] S.I. Braginskii, Review of Plasma Physics, 1 (1965) 205.
[14] R.D. Hazeltine, Rotation of a toroidally confined, collisional plasma, Physics of Fluids, 17 (1974) 961-968.
[15] K.T. Tsang, E.A. Frieman, Toroidal Plasma Rotation in Axisymmetric and Slightly Nonaxisymmetric Systems, Physics of Fluids, 19 (1976) 747-756.
[16] A.B. Mikhailovskii, V.S. Tsypin, Transport-Equations of Plasma in a Curvilinear Magnetic-Field, Soviet Journal of Plasma Physics, 10 (1984) 51.
[17] W.M. Stacey, D.J. Sigmar, Viscous effects in a collisional tokamak plasma with strong rotation, Physics of Fluids, 28 (1985) 2800-2807.
[18] F.L. Hinton, S.K. Wong, Neoclassical Ion-Transport in Rotating Axisymmetric Plasmas, Physics of Fluids, 28 (1985) 3082-3098.
[19] J.W. Connor, S.C. Cowley, R.J. Hastie, L.R. Pan, Toroidal Rotation and Momentum Transport, Plasma Physics and Controlled Fusion, 29 (1987) 919-931.
[20] W.M. Stacey, Poloidal Rotation and Density Asymmetries in a Tokamak Plasma with Strong Toroidal Rotation, Phys Fluids B-Plasma, 4 (1992) 3302-3309.
[21] R.D. Hazeltine, J.D. Meiss, Plasma confinement, Addison-Wesley Pub. Co., Redwood City, Calif. :, 1992.
[22] A. Rogister, Revisited Neoclassical Transport-Theory for Steep, Collisional Plasma Edge Profiles, Physics of Plasmas, 1 (1994) 619-635.
[23] H.A. Claassen, H. Gerhauser, A. Rogister, C. Yarim, Neoclassical theory of rotation and electric field in high collisionality plasmas with steep gradients, Physics of Plasmas, 7 (2000) 3699-3706.
[24] W.M. Stacey, A neoclassical model for toroidal rotation and the radial electric field in the edge pedestal, Physics of Plasmas, 11 (2004) 3096-3099.
[25] S.K. Wong, V.S. Chan, A drift-kinetic approach to neoclassical transport theory for plasmas with large toroidal rotation, Physics of Plasmas, 11 (2004) 3432-3442.
[26] P.J. Catto, A.N. Simakov, A drift ordered short mean free path description for magnetized plasma allowing strong spatial anisotropy, Physics of Plasmas, 11 (2004) 90-102.
[27] P.J. Catto, A.N. Simakov, Evaluation of the neoclassical radial electric field in a collisional tokamak, Physics of Plasmas, 12 (2005) 012501.
[28] J.J. Ramos, Fluid formalism for collisionless magnetized plasmas, Physics of Plasmas, 12 (2005) 112301.
[29] W.M. Stacey, Extension and comparison of neoclassical models for poloidal rotation in tokamaks, Physics of Plasmas, 15 (2008) 012501.
[30] W.M. Stacey, R.W. Johnson, J. Mandrekas, A neoclassical calculation of toroidal rotation profiles and comparison with DIII-D measurements, Physics of Plasmas, 13 (2006) 062508.

[31] W.M. Stacey, D.R. Jackson, Poloidal Rotation, Density Asymmetries, and Momentum Confinement in Tokamak Experiments, Phys Fluids B-Plasma, 5 (1993) 1828-1835.
[32] W.M. Stacey, M. Murakami, Momentum confinement in DIII-D shots with impurities, Physics of Plasmas, 8 (2001) 4450-4454.
[33] W.M. Stacey, J. Mandrekas, Comparision of neoclassical rotation theory with experiment under a variety of conditions in DIII-D, Physics of Plasmas, 9 (2002) 1622-1628.
[34] R.L. Miller, M.S. Chu, J.M. Greene, Y.R. Lin-Liu, R.E. Waltz, Noncircular, finite aspect ratio, local equilibrium model, Physics of Plasmas, 5 (1998) 973-978.
[35] W.M. Stacey, Applications of the Miller equilibrium to extend tokamak computational models, Physics of Plasmas, 15 (2008) 122505.
[36] W.M. Stacey, C. Bae, Representation of the plasma fluid equations in "Miller equilibrium" analytical flux surface geometry, Physics of Plasmas, 16 (2009) 082501.
[37] J.L. Luxon, A design retrospective of the DIII-D tokamak, Nuclear Fusion, 42 (2002) 614.
[38] S.P. Hirshman, D.J. Sigmar, Neoclassical Transport of Impurities in Tokamak Plasmas, Nuclear Fusion, 21 (1981) 1079-1201.
[39] W.A. Houlberg, K.C. Shaing, S.P. Hirshman, M.C. Zarnstorff, Bootstrap current and neoclassical transport in tokamaks of arbitrary collisionality and aspect ratio, Physics of Plasmas, 4 (1997) 3230-3242.
[40] Y.B. Kim, P.H. Diamond, R.J. Groebner, Neoclassical Poloidal and Toroidal Rotation in Tokamaks, Phys Fluids B-Plasma, 3 (1991) 2050-2060.
[41] W.M. Stacey, Neoclassical calculation of poloidal rotation and poloidal density asymmetries in tokamaks, Physics of Plasmas, 9 (2002) 3874-3883.
[42] W.M. Stacey, Fusion plasma physics, Wiley-VCH ; John Wiley, Weinheim Chichester, 2005.
[43] J. Candy, A unified method for operator evaluation in local Grad-Shafranov plasma equilibria, Plasma Physics and Controlled Fusion, 51 (2009) 105009.
[44] W.M. Stacey, Ion particle transport in the tokamak edge plasma, Contributions to Plasma Physics, 48 (2008) 94-98.
[45] K.H. Burrell, P. Gohil, R.J. Groebner, D.H. Kaplan, J.I. Robinson, W.M. Solomon, Improved charge-coupled device detectors for high-speed, charge exchange spectroscopy studies on the DIII-D tokamak, Review of Scientific Instruments, 75 (2004) 3455-3457.
[46] K.H. Burrell, D.H. Kaplan, P. Gohil, D.G. Nilson, R.J. Groebner, D.M. Thomas, Improved charge coupled device detectors for the edge charge exchange spectroscopy system on the DIII-D tokamak, Review of Scientific Instruments, 72 (2001) 1028-1033.
[47] W.M. Solomon, K.H. Burrell, P. Gohil, R.J. Groebner, L.R. Baylor, Extraction of poloidal velocity from charge exchange recombination spectroscopy measurements, Review of Scientific Instruments, 75 (2004) 3481-3486.
[48] R.C. Isler, Observation of the Reaction H^{0} + O^{8+} → H^{+}(O^{7+}) during Neutral-Beam Injection into ORMAK, Physical Review Letters, 38 (1977) 1359-1362.
[49] W.M. Solomon, K.H. Burrell, R. Andre, L.R. Baylor, R. Budny, P. Gohil, R.J. Groebner, C.T. Holcomb, W.A. Houlberg, M.R. Wade, Experimental test of the neoclassical theory of impurity poloidal rotation in tokamaks, Physics of Plasmas, 13 (2006) 056116.

[50] W.M. Solomon, K.H. Burrell, R. Feder, A. Nagy, P. Gohil, R.J. Groebner, Characterization of cross-section correction to charge exchange recombination spectroscopy rotation measurements using co- and counter-neutral-beam views, Review of Scientific Instruments, 79 (2008) 10F531.
[51] B.A. Grierson, K.H. Burrell, W.M. Solomon, N.A. Pablant, Deuterium velocity and temperature measurements on the DIII-D tokamak, Review of Scientific Instruments, 81 (2010).
[52] https://fusion.gat.com/global/Home, General Atomics Fusion Energy Research, (13 March 2012).
[53] S.H. Strogatz, Nonlinear dynamics and Chaos : with applications to physics, biology, chemistry, and engineering, Addison-Wesley Pub., Reading, Mass., 1994.
[54] C.T. Kelley, Society for Industrial and Applied Mathematics., Iterative methods for linear and nonlinear equations, in: Frontiers in applied mathematics 16, Society for Industrial and Applied Mathematics (SIAM, 3600 Market Street, Floor 6, Philadelphia, PA 19104), Philadelphia, Pa., 1995.
[55] J.M. Ortega, W.C. Rheinboldt, Society for Industrial and Applied Mathematics., Iterative solution of nonlinear equations in several variables, in: Classics in applied mathematics 30, Society for Industrial and Applied Mathematics (SIAM, 3600 Market Street, Floor 6, Philadelphia, PA 19104), Philadelphia, Pa., 2000.
[56] J.F. Traub, Iterative methods for the solution of equations, Prentice-Hall, Englewood Cliffs, N.J.,, 1964.
[57] S. Kirkpatrick, C.D. Gelatt, M.P. Vecchi, Optimization by Simulated Annealing, Science, 220 (1983) 671-680.
[58] D. Bertsimas, J.N. Tsitsiklis, Introduction to linear optimization, Athena Scientific, Belmont, Mass., 1997.
[59] W.M. Stacey, R.J. Groebner, Interpretation of edge pedestal rotation measurements in DIII-D, Physics of Plasmas, 15 (2008) 012503.
[60] G.H. Golub, C.F. Van Loan, Matrix computations, 3rd ed., Johns Hopkins University Press, Baltimore, 1996.
[61] D.G. Luenberger, Linear and nonlinear programming, 2nd ed., Springer, New York, NY, 2005.
[62] W.C. Rheinboldt, Methods for solving systems of nonlinear equations, 2nd ed., Society for Industrial and Applied Mathematics, Philadelphia, 1998.
[63] J.R. Shewchuk, An Introduction to the Conjugate Gradient Method Without the Agonizing Pain, (1994).
[64] C. Bae, Stacey, Weston M., Solomon, Wayne M., Extension of neoclassical rotation theory for tokamaks to realistically account for the geometry of magnetic flux surfaces, Physics of Plasma Physics, (In preparation).
[65] J.I. Choi, Applications of nonlinear dynamics in atomic and molecular systems, in, 2007.
[66] A.N. Simakov, P.J. Catto, What are the limitations of Braginskii's fluid equations and Hazeltine's drift kinetic equation?, Aip Conf Proc, 871 (2006) 238-249.

VITA

CHEONHO BAE

BAE was born in Busan, South Korea. He attended the United States Air Force Academy as an exchange cadet from the Republic of Korea Air Force (ROKAF) and was commissioned in the ROKAF as a second lieutenant, flew various jets, and served in military until 2005 when he decided to pursue a career in academics. Coming to Georgia Tech as an Aerospace engineering major, he later transferred to the Nuclear Engineering with nuclear fusion study. In his free time, he enjoys Korean traditional painting, playing soccer, and being harassed by his son, Youngsoo.